TR 3334

Two-Dimensional ACAR and Low-Background DBAR Studies on Materials with Defects

The research described in this thesis was performed at the Department of Reactor Physics of the Interfaculty Reactor Institute, Delft University of Technology, Mekelweg 15, 2629 JB Delft, The Netherlands.

Two-Dimensional ACAR and Low-Background DBAR Studies on Materials with Defects

BIBLIOTHEEK TECHNISCHE UNIVERSITEIT
Prometheusplein 1
DELFT

PROEFSCHRIFT

ter verkrijging van de graad van doctor
aan de Technische Universteit Delft,
op gezag van de Rector Magnificus prof.ir. K.F. Wakker,
in het openbaar te verdedigen ten overstaan van een commissie,
door het College voor Promoties aangewezen,
op dinsdag 18 mei 1999, te 10.30 uur

door

Abraham Cornelis KRUSEMAN

natuurkundig ingenieur
geboren te Amsterdam

Dit proefschrift is goedgekeurd door de promotoren:
Prof. dr. A. van Veen
Prof. dr. ir. H. van Dam

Samenstelling promotiecommissie:

Rector Magnificus, voorzitter	
Prof. dr. A. van Veen,	Rijksuniversiteit Groningen, promotror
Prof. dr. ir. H. van Dam,	Technische Universiteit Delft, promotor
Prof. dr. ir. C.W.E. van Eijk,	Technische Universiteit Delft
Prof. dr. L. Niesen,	Rijksuniversiteit Groningen
Prof. P. Hautojärvi,	Helsinki University of Technology
Prof. dr. W. Th. Wenckebach,	Technische Universiteit Delft
Dr. ir. P.E. Mijnarends,	Technische Universiteit Delft

Dr. ir. P.E. Mijnarends heeft als begeleider in belangrijke mate aan de totstandkoming van het proefschrift bijgedragen.

Published and distributed by:

Delft University Press
Postbus 98
2600 MG Delft
The Netherlands
Telephone: +31 15 2783254
Fax: +31 15 2781661
E-mail: dup@dup.tudelft.nl

ISBN 90-407-1880-6
NUGI: 841

Copyright © 1999 by A.C. Kruseman

All rights reserved. No part of the material protected by this copyright notice may be reproduced or utilized in any form or by any means, electronic or mechanical, including photocopying, recording or by any information storage and retrieval system, without permission from the publisher: Delft University Press.

Printed in the Netherlands

Contents

1 Introduction **1**

1.1 General 1

1.2 Positrons 3

1.3 Positron annihilation techniques 7

2 Theory **17**

2.1 Introduction 17

2.2 Momentum distribution 17

2.3 Atomic superposition calculations 20

2.4 Conclusions 23

3 Experimental setup **27**

3.1 Introduction 27

3.2 2D-ACAR 27

3.3 Two detector Doppler broadening 49

4 Data Analysis of 2D-ACAR Spectra **57**

4.1 Introduction 57

4.2 Momentum sampling function 57

4.3 Determination of the centre 62

4.4 Symmetry 63

4.5 Background 63

4.6 Anisotropy 63

4.7 Resolution function correction 68

5 Metals **75**

5.1 Introduction 75

5.2 Aluminium 76

5.3 Copper 90

5.4 Other metals 95

5.5 Conclusions 96

6 Semiconductors **101**
6.1 Electron irradiated silicon 101
6.2 Oxygen implanted silicon 126
6.3 Gallium Nitride 142

7 Calcium sulphate **153**
7.1 Introduction 153
7.2 Experimental 155
7.3 Discussion 161
7.4 Conclusions 164

8 Concluding remarks **167**

Summary **169**

Nomenclature **173**

List of Publications **177**

Samenvatting **179**

Dankwoord **183**

Cirriculum Vitea **185**

Chapter 1

Introduction

1.1 General

Materials science studies solids with the aim to obtain insight into the physical structures, processes and mechanisms which are the basis for the macroscopic properties of materials. Materials science covers a wide range of fields, often at the cutting edge of technological advancement. One of the fields of interest is the study of defects in materials. A better knowledge of defects is necessary for industry to improve the manufacture of electronic and construction materials. Even defects on an atomic scale can already hamper the use of a material. Moreover, properly designed defects give the material certain desired properties, e.g. doping atoms in semiconducting materials. A better knowledge of these defects and their behaviour makes it possible to adapt the production processes to control the introduction of defects and thus improve the quality of a material or the performance of a device.

In the sixties it was realised that positrons form a good probe for the investigation of open volume defects due to the propensity of positrons to trap at these defects [1]. The positron annihilates with an electron under emission of two annihilation gamma rays. The characteristics of the emitted gamma rays are different for positrons annihilating near a defect compared to positrons which annihilate in a defect-free material. This effect is utilised in the various positron annihilation techniques in use nowadays. Positron annihilation techniques are especially well suited to detect very small defects in very low concentrations (see figure 1.1). This makes it an interesting technique for the study of fine lines used as electronic interconnects. It is already possible to detect 1 appm of neutral charged open volume defects [2, 3] and the technique is used to profile defect concentrations in metals, polymers and semiconductors. The utilisation of the positron annihilation techniques can be improved if, besides the defect concentration, also the defect type can be determined. Conventional positron annihilation techniques such as the positron lifetime and the Doppler broadening of annihilation radiation only provide limited information about the defect type. Two less common techniques have the potential to pro-

vide additional information: the two-dimensional angular correlation of annihilation radiation technique which yields a two-dimensional spectrum while conventional techniques only yield a one-dimensional spectrum, and the two detector Doppler broadening of annihilation radiation technique which yields one-dimensional spectra with a superior peak to background ratio compared to the single detector technique. This second technique opens the possibility to measure the contribution of core electrons to the momentum distribution and obtain information about the atoms surrounding the annihilation site [5, 6]. The Defects in Matter group of the Reactor Physics department of the Interfaculty Reactor Institute decided to expand their positron annihilation setups with these two techniques. This thesis describes the construction of these new setups and their application in the field of materials science.

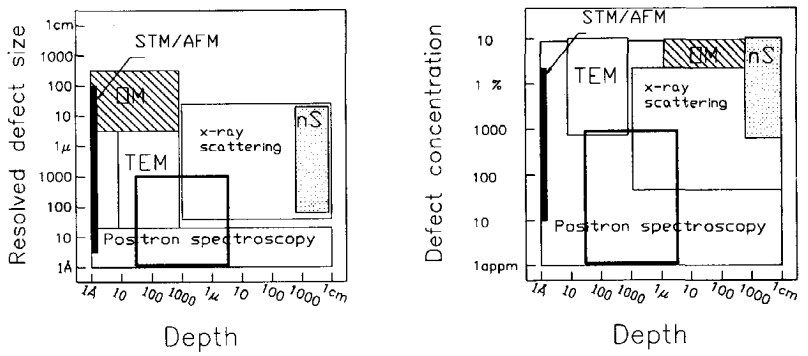

Figure 1.1: *The power of positron annihilation techniques for open volume defect analysis compared to other relevant techniques. OM: Optical Microscopy, nS: neutron Scattering, TEM: Transmission Electron Microscopy, STM: Scanning Tunneling Microscopy, AFM: Atomic Force Microscopy. The solid black lines outline the range of interest for studies of fine lines used as electronic interconnects (from Howell et al. [4]).*

The structure of the thesis is as follows. The present chapter gives a general introduction about positrons and positron annihilation techniques. To investigate the high-momentum part of the momentum distribution support from theoretical calculations is necessary. One of the methods which can provide this information is the atomic superposition method of Puska *et al.* [7]. The theory behind this method is explained in chapter 2. Chapter 3 describes the experimental setup of the two newly built systems. The two-dimensional angular correlation of annihilation radiation setup yields two-dimensional spectra. The data handling of these spectra is explained in chapter 4. The two setups were used to measure a wide variety of materials. Chapters 5, 6 and 7 show some experimental results for the new setups. Three different types of materials were investigated: the results for a selection of metals are collected in chapter 5, chapter 6

contains the results for semiconducting materials and chapter 7 which describes hydration and dehydration effects in gypsum. The thesis is concluded in chapter 8 with some final remarks.

1.2 Positrons

1.2.1 Positron physics

Positrons are the anti-particles of electrons; they have the same mass but an opposite charge. Dirac [8,9] predicted the existence of the positron in 1930. Two years later Anderson [10] experimentally detected the positron in his cloud chamber experiments. Positrons are not stable in the vicinity of their anti-particles, electrons, and annihilate. In solids this will be predominantly annihilation into two photons. Annihilations resulting in the emission of one photon are very rare because of energy and momentum conservation. The one photon annihilation mode is only possible in vicinity of a heavy nucleus which takes up the recoil momentum. The emission of three of more photons is possible but the probability strongly decreases as the number of photons increases. Ore and Powell [11] calculated the ratio between 3γ and 2γ to be $1/371$. All other annihilation modes have an even smaller probability compared to the 2γ annihilation mode. Since the electron and the positron have spin 1/2 annihilation processes with a odd number of photons are only possible for a combined spin of 1 and the processes with an even number of photons for a spin of 0.

When a positron is injected into a material it will thermalise within 10^{-12} s^{-1} [12–14] which is short compared to the mean lifetime of the positron of 10^{-10} s^{-1}. The lifetime is determined by the overlap between the electron and positron wavefunctions and strongly depends on the local electron density. When a positron is trapped in a vacancy, the overlap will be smaller and the mean lifetime will increase. This lifetime can be measured with a positron lifetime setup. In an open-volume defect the electron density is smaller than in the defect-free material and the lifetime becomes longer, thus, the positron lifetime provides information about defects.

After thermalisation, and in the absence of trapping, the positron remains delocalised. The de Broglie wavelength, λ_{th}, is given by

$$\lambda_{th} = \frac{2\pi\hbar}{(3m_0k_bT)^{1/2}} \sim 6.2\sqrt{\frac{300K}{T}}(\text{nm}), \tag{1.1}$$

with m_0 being the rest mass of the positron, k_b the Boltzman constant and T the temperature. At room temperature this is an order of magnitude larger than the typical lattice parameter, and hence the positron essentially behaves like a delocalised Bloch wave in the solid. Figure 1.2a shows the positron density in fcc Al. The positron wavefunction has the same periodicity as the fcc crystal structure. An open-volume defect results in a local lowering of the positron potential

energy which can trap the positron. Figure 1.2b shows the positron density in fcc Al with one missing atom. The positron becomes strongly localised at the position of the missing atom.

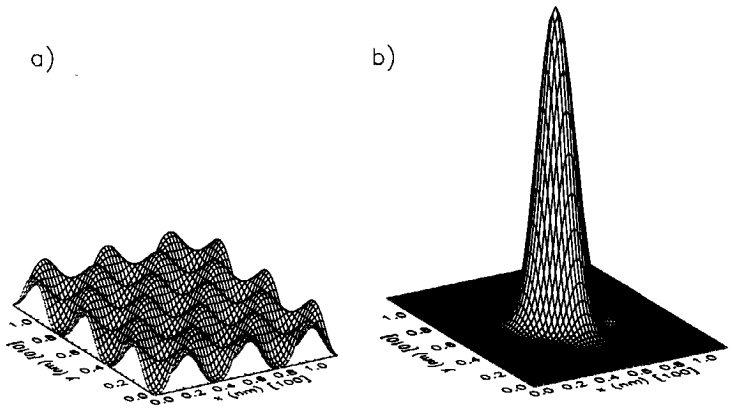

Figure 1.2: *a) Positron density in fcc Al. b) Positron density in fcc Al with a vacancy.*

With the presently available source strengths on average only one positron will be in the solid at any time and therefore the positron is in its ground state after thermalisation. The kinetic energy of the positron (25 meV at 300 K) is small compared to that of the electron in the solid (typically a few eV) and the momentum of the annihilation gamma rays therefore mainly reflects the momentum of the electron of the electron-positron pair.

In the center-of-mass system the two gamma rays are emitted in exactly opposite directions and each has an energy of $E = m_0c^2 - E_B/2$, where c is the velocity of light and E_B the binding energy of the positron and the electron in the solid. A large fraction ($\sim$90 %) of the annihilations occurs with the outermost electrons with a typical binding energy of a few eV. This binding energy is small compared to m_0c^2 (511 keV).

In the laboratory frame the momentum $\mathbf{p}$ of the positron-electron pair causes an energy shift,ΔE, and a small deviation, Θ, from collinearity as can be seen in figure 1.3. The angle Θ can be

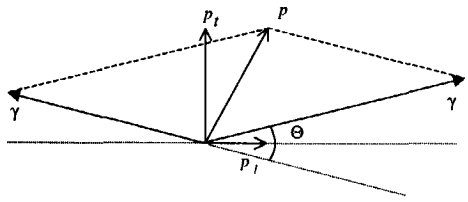

Figure 1.3: *The two annihilation photons. The transverse component of the momentum of the positron-electron pair, p_t, will cause a small deviation from collinearity. For the sake of clarity the angles in this figure are exaggerated.*

calculated from the transverse part of the momentum, p_t,

$$\Theta \sim sin(\Theta) = p_t/m_0c \tag{1.2}$$

The approximation of $\Theta \sim sin(\Theta)$ can be applied since the typical angle between the gamma rays is of the order of a few milliradians. These small angles can be measured with Angular Correlation of Annihilation Radiation (1D- or 2D-ACAR) systems which have resolutions down to 0.3 mrad [15]. The energy shift is equal to

$$\Delta E = cp_l/2 \tag{1.3}$$

with p_l the longitudinal component of the momentum of the electron-positron pair. One photon is shifted upwards and the other one is shifted downwards in energy. The energy-shift or Doppler-shift is measured in the Doppler Broadening of Annihilation Radiation (DBAR) technique. The energy shifts are of the order of 1.5 keV while modern high purity Ge detectors have an energy resolution of the order of 1.1 keV (4 mrad) * at the 511 keV photo peak. The resolution of a DBAR system is approximately a factor 10 worse than that of an ACAR system but the counting rates can be much higher. The acquisition time for a DBAR experiment is in the order of hours while that for an ACAR experiment is in the order of days.

1.2.2 Positron sources

Positrons can be produced by the nuclear decay of isotopes with an excess of protons or by pair production by high energy photons ($E_\gamma > 1.022$ MeV). In positron bulk studies, positrons are generally derived from β^+ decay of radioactive isotopes such as ^{22}Na, ^{58}Co or ^{64}Cu. During the decay of these isotopes a positron and a neutrino are emitted. The positron will have a

*1 keV is equivalent to 3.91 mrad (see equation 1.2 and 1.3).

continuous energy distribution which for ^{22}Na ranges from 0 to 0.54 MeV. The positrons have a broad implantation profile due to the wide energy range (e.g. 90 % of the positrons of a ^{22}Na source is stopped in 0.26 mm Si [16]). This makes these sources only suited for studies of bulk materials. For the study of surfaces and interfaces a mono-energetic beam of slow positrons is necessary. The positrons emitted from a source are stopped in a moderator (metallic moderators with a negative positron workfunction such as tungsten are commonly used). A small fraction will be emitted after thermalisation. These re-emitted positrons have an energy spread of a few eV. An electric field is used to accelerate the positrons and implant them in the sample with a selected energy. The energy range is typically between 0 and 30 keV. Usually, only Doppler broadening measurements are done with slow positron beams. Due to the low moderation efficiency, 10^{-3} to 10^{-4}, the beam intensity is too low to perform conventional ACAR measurements. To perform ACAR measurements with slow positrons a high-intensity beam, $\sim 1 \times 10^8$ e^+/s, is necessary. Several options are available to construct and high-intensity beam:

- Activation of ^{63}Cu to ^{64}Cu which decays under the emission of a positron.
- Acceleration of electrons in a LINAC. The electrons are stopped in a material with a high Z and the bremsstrahlung creates positron-electron pairs.
- Pair production from high-energetic gamma-rays which are present near the reactor core.

A LINAC gives a pulsed positron beam while a reactor-based beam is continuous, the latter option has the advantage of avoiding saturation problems of the detectors.

High-intensity slow positron beams are operational or under construction at only a few institutes in the world [17–20]. The at the Interfaculty Reactor Institute (IRI) developed high-intensity beam called POSH ("POSitrons at the Hoger onderwijs reactor") reached an intensity of 0.8×10^8 e^+/s at full reactor power (2 MW) during a test in 1997. Recent results at a power of 10 kW showed that an improvement in the intensity of beam in the final configuration with a factor of four can be realised. The POSH beam will be used for ACAR measurements of surfaces and interfaces and for an instrument for micro-analysis [21].

1.2.3 Positronium

Under the right conditions the positron can form a bound state with an electron with a binding energy of $\sim$ 6.8 eV. This was first predicted classically by Mohorovicic [22] in 1934 and later quantum mechanically by Ruark [23] in 1945. Ruark suggested the name positronium for the hydrogen-like structure and the abbreviation Ps. Experimentally positronium was observed by Deutsch in 1951 [24]. The ground states of positronium consist of the singlet $^1S_0$ state, para-positronium (p-Ps), and the triplet $^3S_1$ state, ortho-positronium (o-Ps). When no external fields

are present the formation of o-Ps is three times as likely as the formation of p-Ps. In vacuum p-Ps has a lifetime of 125 ps and decays via the emission of two 511 keV gamma-rays. The lifetime in vacuum for o-Ps is 142 ns (three orders of magnitude longer than p-Ps). The non-zero spin of o-Ps requires an annihilation process with an odd number of photons and o-Ps will mainly decay into three photons [25]. This process has a considerable smaller probability than two photon annihilation [26].

The formation of positronium is not possible in regions with a high electron density such as metals and semiconductors. In insulators and materials with large open volumes the formation of positronium is possible. In these materials p-Ps still has a lifetime of 125 ps but the lifetime of o-Ps is reduced to a few nanoseconds owing to 'pick off' reactions. In this reaction the parallel spin electron is exchanged for an electron with anti-parallel spin, thus enabling 2γ annihilation. The momentum of positronium is very small and the annihilation of p-Ps will therefore result in a narrow contribution to the 2D-ACAR distribution. The annihilation of o-Ps on the other hand results in a broad contribution to the ACAR distribution due to the annihilation with 'pick-off' electrons.

1.3 Positron annihilation techniques

1.3.1 Angular Correlation of Annihilation Radiation

The Angular Correlation of Annihilation Radiation(ACAR) method measures the deviation of the collinearity between the two annihilation photons. In the older one-dimensional ACAR (long-slit ACAR) only one component was measured. Since the availability of two-dimensional position-sensitive detectors the interest has shifted to the two-dimensional ACAR technique. Figure 1.4 shows the geometry of a 2D-ACAR experiment. In 2D-ACAR both Θ and Φ are measured which provides the two transverse components of the momentum:

$$\Theta \sim sin(\Theta) = p_x/m_0c \tag{1.4}$$

$$\Phi \sim sin(\Phi) = p_y/m_0c \tag{1.5}$$

The small angle approximation is appropriate since the typical angle between the gamma rays is of the order of a few milliradians.

One obtains the two-dimensional projection of the three dimensional-momentum density:

$$N(\Theta,\Phi) = N(p_x,p_y) \propto \int \rho^{2\gamma}(\mathbf{p})dp_z \tag{1.6}$$

with $\rho^{2\gamma}$ the momentum density of the electrons as seen by positrons. Figure 1.5 shows an example of a 2D-ACAR distribution for Si. The samples are usually aligned with the integration

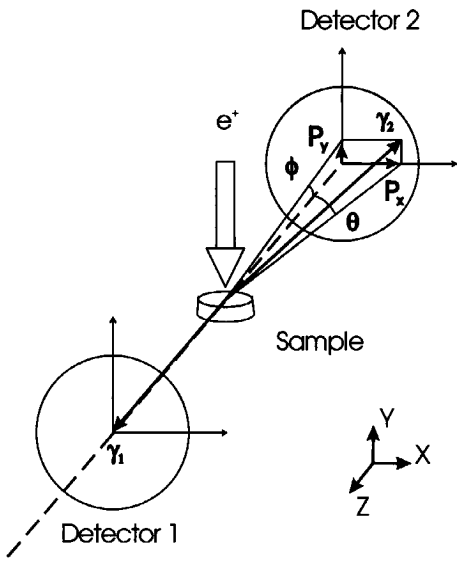

Figure 1.4: *Geometry of a 2D-ACAR experiment.*

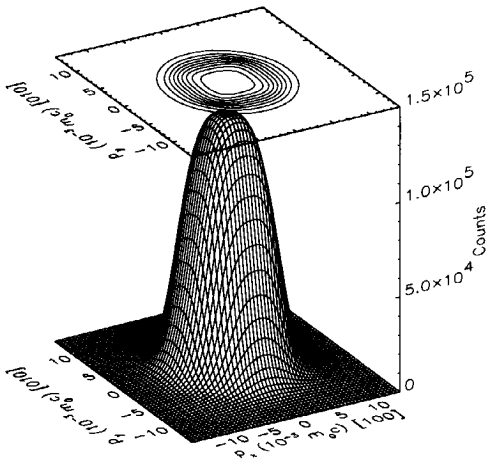

Figure 1.5: *ACAR distribution for Si.*

direction along one of the main crystallographic directions. In principle, by measuring also the Doppler shift beside the angles Θ and Φ, one could obtain the three-dimensional momentum density. In practice, such an experiment is not feasible because of the low signal intensity when a detector with a good energy and spatial resolution is used [27]. Another possibility consists of measuring the two-dimensional projection for a sufficient number of different sample orientations and using these measurements to reconstruct the three-dimensional momentum density [28].

The 2D-ACAR technique is one of the techniques capable of deriving information regarding the electronic structure. It has been used in the study of Fermi surface topology. For this type of study a good resolution is important. The resolution is less important when the 2D-ACAR technique is used for defect analysis.

1.3.2 Doppler Broadening of Annihilation Radiation

The DBAR-technique measures the Doppler shift of **one** of the two annihilation photons. A one-dimensional projection is obtained of the three-dimensional momentum density.

$$N(E) = N(p_z) \propto \int\int \rho^{2\gamma}(\mathbf{p}) dp_x dp_y \tag{1.7}$$

The Doppler shift is measured with Ge-detectors. The best detectors have a resolution of 1.1 keV at the 511 keV annihilation peak while a typical Doppler shift will be 1.5 keV. Due to the double integration and the resolution of the detectors the measured distribution is almost featureless. For characterising this distribution, MacKenzie *et al.* [29] introduced the line shape parameter S. It is calculated as the ratio between the central region of the annihilation peak and the total area (see figure 1.6). The integration intervals are set to maximise the sensitivity to changes in the shape of the momentum distribution. In the setup at Delft University of Technology the interval for the calculation of the S parameter is 1.65 keV wide and centred at 511 keV.. The main contribution in the central region is stemming from annihilations of positrons with valence electrons. Annihilations with core electrons result in larger Doppler shifts. In an open volume defect a smaller fraction of the positrons annihilates with those core electrons; as a result the peak becomes narrower and the S value will increase.

In addition to the S parameter, other parameters have been proposed to extract more information from the annihilation peak. One of the more promising ones is the wing- or W parameter. The W parameter is defined by the area of two energy windows in the tails of the annihilation photo peak divided by the total area. In our setup the wing intervals are [504.7, 508.7] keV and [513.3, 517.3] keV for the left and right side wings, respectively. While the S parameter provides information about valence electrons that dominate the central part of the annihilation peak, the W parameter provides information about core-electrons. The absolute values of S

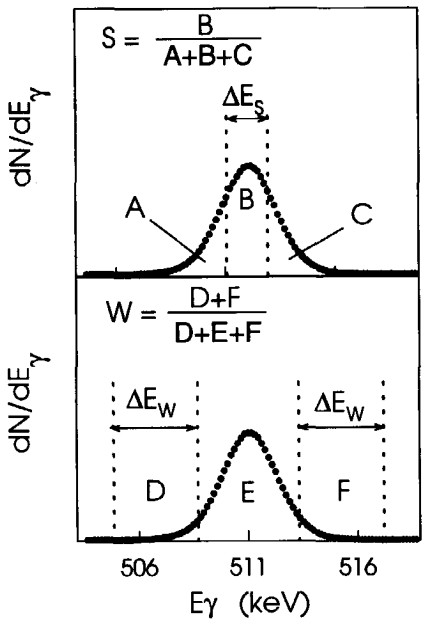

Figure 1.6: *The 511 keV annihilation photo-peak. The S parameter is defined as the area B (defined by energy window ΔE_s) divided by the total area A+B+C. The W parameter is defined as the area of the wings D and F divided by the total area.*

and W are influenced by the resolution of the setup and the limits of the window intervals. To compare S and W values obtained with different setups the S and W values are divided by those of a reference material. Defect-free Si is usually chosen as a reference.

The development of the slow positron beams, such as the Variable Energy Positron (VEP) beam at the Delft University of Technology [30,31], has opened up a whole range of new applications for DBAR measurements. The implantation energy of the positrons can be varied between 0 and 30 keV By adjusting the energy one can probe the different layers of a sample samples and perform a series of measurements as a function of energy(depth). The implantation profile of such a mono-energetic positron beam can be parameterised with a Makhovian profile [32]:

$$P(z,E) = \frac{mz^{m-1}}{z_0^m} exp[-(z/z_0)^m] \tag{1.8}$$

with E the incident energy of the positrons, m a shape parameter and z_0 related to the mean

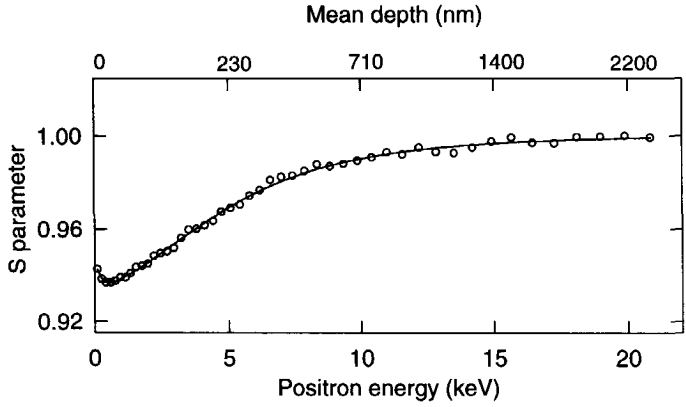

Figure 1.7: *S-E curve for defect-free Si as measured with the VEP (symbols) and the fit obtained with VEPFIT (line).*

implantation depth $\bar{z}$. The latter is given by

$$\bar{z} = \frac{\sqrt{\pi}}{2} z_0 = \frac{\alpha}{\rho} E^n \tag{1.9}$$

in which ρ is the density of the material and α and n are material independent constants. Vehanen *et al.* [33] performed Monte Carlo simulations and obtained: $m = 2.0$, $n = 1.62$ and $\alpha = 4.0$ μg cm^{-2} keV$^{-1.62}$. New Monte Carlo simulations by Ghosh *et al.* [34] showed a dependence of α and n on the sample material.

Figure 1.7 shows an example of an S-E curve for defect-free Si. Although the sample is defect-free, one observes a change in the S-value as a function of implantation energy. This is caused by the contribution of a surface layer which has a different S value compared to the bulk S value. Although the surface layer is small it has a profound influence even for higher energies due to the implantation profile and the diffusion of the positron in a solid after thermalisation. To analyse the data a program is necessary that simulates the implantation, the diffusion, the trapping and the annihilation of the positrons. A program capable of simulating a positron in a solid is VEPFIT [35]. The studied system is described as a stack of different positron trapping layers, each layer being characterised by a thickness, a characteristic lineshape parameter and a positron diffusion layer (which is related to the defect concentration). The lineshape parameter for a given implantation energy is then given by

$$S(E) = \sum_{i=1}^{n} f_i(E) S_i + f_{surface}(E) S_{surface} + f_{bulk}(E) S_{bulk}, \tag{1.10}$$

where $f_i(E)$ is the fraction of the positrons implanted at energy E which annihilate in layer i and S_i the assigned value to the lineshape parameter in layer i, and *bulk* and *surface* refer to the bulk and surface contributions. In the fitting part of the program the model parameters are optimised by minimisation of the residue between the measured lineshape parameter and the calculated lineshape parameter. An analogue approach is used for the lineshape parameter W. The fitting of the two sets of experimental data yields information about the characteristic lineshape parameters for a specific layer. By plotting the measured S and W data as a trajectory in a S-W plot, using the implantation energy as the running parameter, a more direct interpretation of the experimental data in terms of layers with distinct S and W values can be obtained. The S-W curves are a useful aid in determining the kind and the number of annihilation sites that play a roll [36, 37].

The analysis of the contribution of the core-electrons to the momentum distribution is hampered by the background present in a Doppler measurement. The collinearity of the annihilation photons can however be used to reduce the background in a Doppler broadening measurement. A second detector is placed at the opposite side of the sample to measure the other annihilation photon in coincidence with the first detector. Two options are possible for the second detector:

- Using a simple scintillation detector with a high efficiency but a poor energy resolution. The background reduction is obtained by the coincidence condition that both detectors should detect a 511 keV photon. This setup is for example employed by the Helsinki University of Technology.
- Using a second Ge-detector. This technique was proposed by Lynn *et al.* [38]. The advantage is the use of the known relation between both energy shifts. This technique is for example applied at Brookhaven National Laboratory and at Delft University of Technology, and leads to a considerably lower background compared to the previous option.

1.3.3 Positron Annihilation Lifetime

Positron lifetime spectroscopy is the most widespread positron annihilation technique due to the simple experimental setup and low cost. A source is used which emits both a gamma ray and a positron. The detection of the gamma ray is used as a start signal, the 511 keV annihilation radiation is used as a stop signal.

In a solid a positron has a finite lifetime τ. In metals this is of the order of 100 ps while in semiconductors lifetimes above 200 ps are measured. When a positron is trapped in a vacancy, the overlap between the electron and positron will be smaller and the lifetime will increase. A positron which is trapped in a mono-vacancy typically has a lifetime which is $\sim$ 60 ps longer

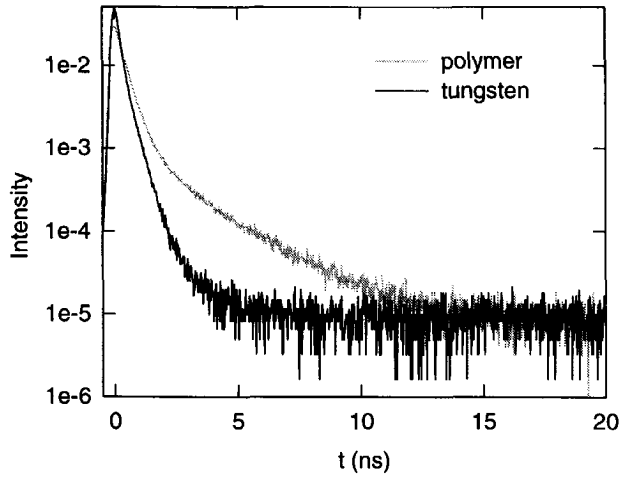

Figure 1.8: *Lifetime spectra for a polymer and for tungsten.*

than a positron annihilating in defect-free material.

A lifetime spectrum takes the shape

$$F(t) = \sum_{i=1}^{N} \frac{I_i}{\tau_i} exp(-t/\tau_i) \tag{1.11}$$

where N is the number of different annihilation states, τ_i is the lifetime of positrons in state i and I_i is the intensity. For defect states the intensity is related to the concentration of the specific defect type. Figure 1.8 shows two examples of lifetime spectra. The lifetime spectrum of the tungsten sample contains only short lifetime components while the lifetime spectrum of the polymer also contains components with a long lifetime ($\sim$ ns) due to the annihilation of o-Ps.

References

[1] I.K. MacKenzie, T.L. Khoo, A.B. McDonald and B.T.A. McKee, *Phys. Rev. Let.* **19** (1967) 946.

[2] P.J. Schultz and K.G. Lynn, *Rev. Mod. Phys.* **60** (1988) 701.

[3] M.J. Puska and R.M. Nieminen, *Rev. Mod. Phys.* **66** (1994) 841.

[4] R.H. Howell, T.E. Cowan, J. Hartley, P. Sterne and B. Brown, *Appl. Surf. Sci.* **116** (1997) 7.

[5] M. Alatalo, B. Barbiellini, M. Hakala, H. Kauppinen, T. Korhonen, M.J. Puska, K. Saarinen, P. Hautojärvi and R.M. Nieminen, *Phys. Rev. B* **54** (1996) 2397.

[6] P. Asoka-Kumar, M. Alatalo, V.J. Ghosh, A.C. Kruseman, B. Nielsen and K.G. Lynn, *Phys. Rev. Lett.* **77** (1996) 2097.

[7] M.J. Puska and R.M. Nieminen, *J. Phys. F* **13** (1983) 333.

[8] P.A.M. Dirac, *Proc. Roy. Soc. (London)* **A126** (1930) 360.

[9] P.A.M. Dirac, *Proc. Camb. Phil. Soc.* **26** (1930) 361.

[10] C.D. Anderson, *Science* **76** (1932) 238, *Phys. Rev.* **41** (1932) 405 and *Phys. Rev.* **43** (1933) 491.

[11] A. Ore and J.L. Powell, *Phys. Rev.* **75** (1949) 1696.

[12] A. Perkins and J.P. Carbotte, *Phys. Rev. B* **1** (1970) 101.

[13] B. Bergersen and E. Pajanne, *Appl. Phys.* **4** (1974) 25.

[14] P. Kubica and A.T. Stewart, *Phys. Rev.* B **4** (1975) 2490.

[15] P.E. Bisson, P. Descout, A. Dupanloup, A.A. Manuel, E. Perreaud, M. Peter and R. Sachot, *Helv. Phys. Acta.* **55** (1982) 100.

[16] J. de Vries, *Positron lifetime technique with applications in materials science*, PhD dissertation, (Delft Universitaire Pers, Delft, 1987).

[17] K.F. Canter, T. Horskey, P.H. Lippel, W.S. Crane and A.P. Mills Jr., in *Positron (Electron)-Gas Scattering*, eds. W.E. Kauppila, T.S. Stein, J.M. Wadehra, (World Scientific, Singapore, 1986) p. 202.

[18] D. Taqqu, *Appl. Surf. Sci.* **116** (1997) 28.

[19] A. van Veen, F. Labohm, H. Schut, J. de Roode, T. Heijenga and P.E. Mijnarends, *Appl. Surf. Sci.* **116** (1997) 39.

[20] G. Triftshäuser, G. Kögel, W. Triftshäuser, M. Springer B. Strasser and K. Schreckenbach, *Appl. Surf. Sci.* **116** (1997) 45.

[21] L.J. Seijbel, *An instrument for positron micro-analysis*, PhD. dissertation, Delft University of Technology, Delft (1995).

[22] S. Mohorovicic, *Astron. Nachr.* **253** (1934) 94.

[23] A.E. Ruark, *Phys. Rev.* **68** (1945) 278.

[24] M. Deutsch, *Phys. Rev.* **82** (1951) 455.

[25] C.I. Westbrook, D.W. Gidley, R.S. Conti and A. Rich, *Phys. Rev. A* **40** (1989) 5489.

[26] A. Rich, *Rev. Mod. Phys.* **53** (1981) 127.

[27] R.M. Singru, *Phys. Lett.* **46a** (1973) 61.

[28] S. Berko, in *Positron Spectroscopy of Solids* , Proc. of the International School of Physics "Enrico Fermi", Course LXXXIII, eds. W. Brandt and A. Duasquier (North-Holland, Amsterdam, 1983) p. 105

[29] I.K. MacKenzie, J.A. Cadly and R.R. Gingerich, *Phys. Lett. A* **33** (1970) 279.

[30] A. van Veen, *J. Trace Microprobe. Tech.* **8** (1990) 1.

[31] H. Schut, *A variable energy positron beam facility with applications in material science*, PhD dissertation, Delft University of Technology, Delft (1990).

[32] A.F. Makhov, *Sov. Phys. -Solid State*, **2** (1961) 1934.

[33] A. Vehanen, K. Saarinen, P. Hautojärvi and H. Humo, *Phys. Rev. B* **35** (1987) 4606.

[34] V.J. Ghosh, *Appl. Surf. Sci.* **85** (1995) 187.

[35] A. van Veen, H. Schut, J. de Vries, R.A. Hakvoort and M.R. IJpma, *AIP Conf. Proc. No. 218* (AIP, New York, 1990) p. 171.

[36] M. Clement, J.M.M. de Nijs, A. van Veen, H. Schut and P. Balk, *IEEE Trans. on Nuc. Sci.* **42** (1995) 1717.

[37] M. Clement, J.M.M. de Nijs, H.Schut, A. van Veen and P. Balk, *J. Appl. Phys* **79** (1996) 9029.

[38] K.G. Lynn, J.R. MacDonald, R.A. Boie, L.C. Feldman, J.D. Gabbe, M.F. Robbins, E. Bonderup and J. Golovchenko, *Phys. Rev. Lett.* **38** (1977) 241.

Chapter 2

Theory

2.1 Introduction

The two-detector Doppler broadening setup mentioned in section 1.3.2 enables us to measure the momentum distribution almost background-free up to 50 mrad. In the central region the main contribution to the momentum distribution stems from annihilation with valence electrons, and the core-electrons only play a minor role. Starting from 20 mrad this changes and the core electrons form the dominant contribution to the momentum distribution. To support the interpretation of the two-detector measurements calculations are necessary which include the contributions of core electrons.

This chapter describes a method for calculating the high-momentum part of the momentum distribution. The program was developed at Helsinki University of Technology and extended at Brookhaven National Laboratory. In the program free-atom wavefunctions are used to describe the electrons. This approximation is not valid for valence electrons and the program is therefore not suited to calculate the complete momentum distribution. But since no band calculations are used the program is fast compared with other methods such as KKR (Korringa-Kohn-Rostoker) [1, 2] and LMTO (linear-muffin-tin-orbital) [3, 4]. The program gives good qualitative agreement with experimental results [5]. Note that atomic units are used in this chapter i.e. $\hbar = m_0 = e = 1$.

2.2 Momentum distribution

The momentum distribution of the annihilating positron-electron pair [6] can be written as:

$$\rho^{2\gamma}(\mathbf{p}) = \pi r_0^2 c \sum_j |\int d\mathbf{r} e^{-i\mathbf{p}\cdot\mathbf{r}} \psi_j^{ep}(\mathbf{r},\mathbf{r})|^2, \tag{2.1}$$

where $\mathbf{p}$ is the total momentum of the annihilating pair, the summation is over all occupied electron states j and $\psi_j^{ep}(\mathbf{r},\mathbf{r})$ is the positron-electron two-particle wavefunction, restricted to the case where the positron and electron reside at the same point. Furthermore, r_0 is the classical electron radius and c is the velocity of light. The two-particle wavefunction $\psi_j^{ep}(\mathbf{r},\mathbf{r})$ can be approximated by

$$\psi_j^{ep}(\mathbf{r},\mathbf{r}) = \psi_+(\mathbf{r})\psi_j(\mathbf{r})\sqrt{\gamma_j(\mathbf{r})}, \tag{2.2}$$

where $\psi_+(\mathbf{r})$ and $\psi_j(\mathbf{r})$ are the positron and electron wavefunction calculated without positron-electron correlation effects and γ_j is the enhancement function, which takes into account the short-range electron pileup at the positron. The total annihilation rate λ ($\lambda = 1/\tau$, where τ is the positron lifetime) is given by

$$\lambda = \int d\mathbf{p}\rho^{2\gamma}(\mathbf{p}). \tag{2.3}$$

Using the approximation of formula 2.2 this can be written as

$$\lambda = \pi r_0^2 c \int d\mathbf{r}|\psi_+(\mathbf{r})|^2 \sum_j |\psi_j(\mathbf{r})|^2 \gamma_j(\mathbf{r}). \tag{2.4}$$

The simplest approximation is the independent-particle model (IPM) in which electron-positron correlation is omitted and $\gamma_j = 1$ for all $\mathbf{r}$ and j. Within the IPM and assuming $\psi_+(\mathbf{r}) = 1$, equation 2.4 reduces to the Sommerfeld result

$$\lambda^{IPM} = \pi r_0^2 c n_-, \tag{2.5}$$

where n_- is the electron density. The annihilation rates obtained with the Sommerfeld equation are an order of magnitude too small. This is caused by neglect of the correlation effects. In a solid, the positron is screened by an electron cloud. This increases the positron-electron contact density. Since correlation effects are not exactly known some approximation is needed. In electronic structure calculations the Local Density Approximation (LDA) is often used. In this approximation the enhancement is a functional of the electron and positron local density. Lantto [7] obtained numerical results based on a hypernetted-chain approximation of a single positron in a homogeneous electron gas. These results were interpolated by Boroński and Nieminen [8]. They constructed $\gamma(n_-)$ as a function of the electron density for three different positron densities. The most commonly used interpolation function is that for vanishing positron density ($n_+ \to 0$):

$$\gamma(r_s) = 1 + 1.23r_s + 0.8295r_s^{3/2} - 1.26r_s^2 + 0.3286r_s^{5/2} + \frac{1}{6}r_s^3, \tag{2.6}$$

where $r_s = (3/4\pi n_-(\mathbf{r}))^{1/3}$. In this interpolation the first two terms and the last term are fixed. At high-density regions ($r_s \to 0$) the enhancement factor is given by the random-phase approximation term of $1 + 1.23r_s$ [9]. The last term is determined by the low-density positronium limit. Recently Puska *et al.* [10] constructed a new interpolation function based on the calculations of Lantto [7]. This function provides a slightly better agreement between calculated and

experimental annihilation rates [10]. The function has the same form as that of Boroński and Nieminen but different coefficients,

$$\gamma(r_s) = 1 + 1.23r_s + 0.9889r_s^{3/2} - 1.482r_s^2 + 0.3956r_s^{5/2} + \frac{1}{6}r_s^3. \tag{2.7}$$

The above formulas for the enhancement are based on calculations for a positron in a homogeneous electron gas. In semiconductors or insulators the screening of the positron is not perfect. For semiconductors Puska *et al.* [11] proposed a semi-empirical model that includes the high-frequency dielectric constant to account for the imperfect screening.

It is known that the LDA has several limitations [12, 13]. For example, a comparison between theoretical and experimental ACAR curves at high momenta indicates that the annihilation with the *d* electrons is overestimated in the calculations [14]. Several attempts have been made to go beyond the LDA. One of the recent attempts is that of Barbiellini *et al.* [15] who introduced the Generalised Gradient Approximation (GGA) [16,17] to the positron field. In this approximation the gradient of the electron density is used in addition to the local density for calculating the enhancement. A parameter ε is introduced, given by

$$\varepsilon = |\nabla n(\mathbf{r})|^2/(n(\mathbf{r})q_{TF})^2, \tag{2.8}$$

where $\nabla n(\mathbf{r})$ is the gradient of the charge density and q_{TF} is the Thomas Fermi screening length (in atomic units $q_{TF} = \sqrt{(4/\pi)p_F}$). For a uniform electron gas $\varepsilon = 0$ whereas in the case of rapid density variations such as for tightly bound core electrons, $\varepsilon \to \infty$. The enhancement factor becomes:

$$\gamma_{GGA} = 1 + (\gamma_{LDA} - 1)e^{-\alpha\varepsilon}. \tag{2.9}$$

In equation 2.9, α is an adjustable parameter. For $\alpha = 0$ the GGA enhancement is identical to the LDA. Barbiellini *et al.* [15] used as LDA function,

$$\gamma(r_s) = 1 + 1.23r_s - 0.0742r_s^2 + \frac{1}{6}r_s^3. \tag{2.10}$$

This function is based on the results of Arponen and Pajanne [18] and consistent with the correlation energy used by them. In combination with this enhancement function they found that $\alpha = 0.22$ gives lifetimes in good agreement with experimental results.

Figure 2.1 shows the enhancement as a function of the distance from the nucleus in Al for the LDA enhancement function of equations 2.6, 2.7 and 2.10 and the effect of using the GGA modification of the LDA enhancement. The GGA results in a smaller enhancement close to the nucleus than the LDA. For large r the GGA enhancement tends to its LDA counter part. The differences between the LDA of Boroński and Nieminen and the LDA of Puska *et al.* are small. This is not surprising since both LDA's are interpolations of the calculations of Lantto [7].

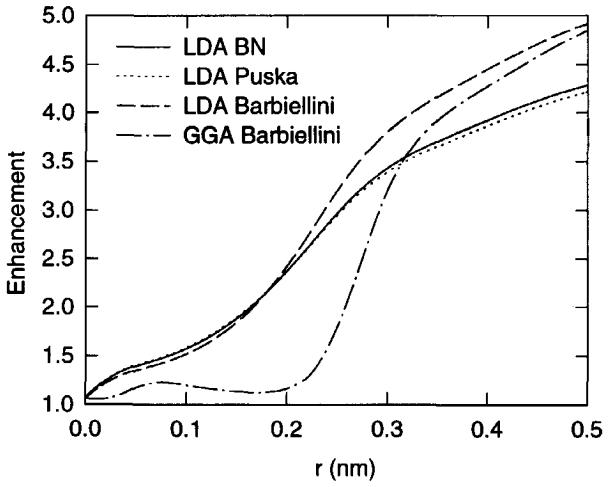

Figure 2.1: *Enhancement functions in Al as a function of the distance from the nucleus for the LDA as proposed by Boroński and Nieminen [8], Puska et al. [10], and Barbiellini et al. [15] and its GGA modification as proposed by Barbiellini et al. [15].*

2.3 Atomic superposition calculations

Until recently, the greatest interest was in the calculation of annihilations with the outermost electrons since the annihilations with these electrons largely determine the lifetime and form the most important contribution to ACAR spectra. Nowadays, the high-momentum part has also attracted interest by the revival of two-detector Doppler broadening measurements. The two-detector setup contains two improvements over single-detector Doppler broadening measurements:

- very low background
- improved resolution

Especially the low background opens the possibility to measure the high-momentum part of the Doppler broadening curve. The annihilations in this region occur mainly with core electrons. Alatalo *et al.* [5] showed that it is possible to obtain information about the chemical environment where the annihilation event took place from the high-momentum part of the Doppler curve. To accomplish this they expanded the atomic superposition (AS) method of Puska and Nieminen [19] to calculate the momentum distribution of the core electrons besides the lifetime.

The AS method uses electron wavefunctions for free atoms and the method is not self-consistent, contrary to the LMTO or the KKR methods, but has the advantage that the calculations are less demanding. It is relatively easy to calculate momentum distributions of defects and to include relaxation effects. In equation 2.1 the two-particle wavefunction is used. This wavefunction is a solution of the Schrödinger equation for the two-particle positron-electron pair with position vectors $\mathbf{r}_1$ and $\mathbf{r}_2$. Alatalo *et al.* [5] applied a trial function that consists of the product of two functions. One function describes the orbital motion of the particles ignoring each other and the other describes the correlated motion. The orbital motion is approximated by a product of single-particle orbitals as in the IPM, i.e.,

$$G_j(\mathbf{r}_1,\mathbf{r}_2) = \psi_+(\mathbf{r}_1)\psi_j(\mathbf{r}_2). \tag{2.11}$$

For the correlated motion they applied the Jastrow approximation [20] which assumes that the pair interaction, $V(\mathbf{r}_1,\mathbf{r}_2)$ is a function of the distance $r_{12} = |\mathbf{r}_1 - \mathbf{r}_2|$ only. The second part of the trial function can thus be written as $f_j(\mathbf{r}_1,\mathbf{r}_2) = u_j(r_{12})$. This leads to a local annihilation rate for state j,

$$\Lambda_j(\mathbf{r}) = \pi r_0^2 c u_j^2(0)\psi_+^2(\mathbf{r})\psi_j^2(\mathbf{r}). \tag{2.12}$$

For the annihilation rate only the contact value $u_j(0)$ is needed. By integrating the local annihilation rate of equation 2.12 over $\mathbf{r}$ space Alatalo *et al.* found that

$$u_j^2(0) = \lambda_j^{LDA,GGA}/\lambda_j^{IPM}, \tag{2.13}$$

which is the state-dependent enhancement factor. Here, λ_j^{IPM} is the annihilation rate with the electrons in the state j, calculated within the independent particle model (IPM) and thus neglecting all correlations between the electrons and the positron. Correspondingly, $\lambda_j^{LDA,GGA}$ is the annihilation rate for the same electronic state calculated in the local density approximation or the generalised gradient approximation, respectively. When the enhancement factor $u_j^2(0)$ is known, the momentum distribution for annihilation with an electron in state j can be calculated as

$$\rho_j^{2\gamma}(\mathbf{p}) = \pi r_0^2 c\, u_j^2(0)\left|\int dr\, e^{-i\mathbf{p}\cdot\mathbf{r}}\psi_+(\mathbf{r})\psi_j(\mathbf{r})\right|^2. \tag{2.14}$$

For the comparison with the two-detector DBAR curves the main interest is in the high-momentum part which arises from annihilations with core electrons. Two simple approximations are used: the electron wavefunctions of free atoms are used and the positron wavefunction is assumed isotropic around each nucleus. These assumptions result in a spherically symmetric momentum distribution of the form

$$\rho_{I,nl}^{2\gamma}(p) = 4\pi(2l+1)\pi r_0^2 c\frac{\lambda_{I,nl}^{LDA,GGA}}{\lambda_{I,nl}^{IPM}}\left|\int_0^\infty dr\, r^2 R_{I,nl}^-(r)R_{I,10}^+(r)\,j_l(pr)\right|^2,$$

where $R^{-}_{I,nl}$ and $R^{+}_{I,10}$ are the radial parts of the electron (quantum numbers n and l) and positron wavefunctions for ion I, respectively and j_l is the l^{th} spherical Bessel function. The assumption of a spherically symmetric momentum distribution is not true for valence electrons. The contribution of the valence electrons to the momentum distribution dominates the contribution of the core electrons between 0 and $\sim 20 \times 10^{-3}\ m_0c$. So, although the contributions of annihilations with valence electrons are included, no conclusions should be drawn based on the calculated momentum distribution in this region. The total 1D-ACAR or DBAR distribution (for a spherically symmetric distribution) is obtained by

$$\rho^{2\gamma}(p_z) = 2\pi \sum_{I,nl} \int_{|p_z|}^{\infty} dp\ p\rho^{2\gamma}_{I,nl}(p). \tag{2.15}$$

Figure 2.2 shows an example for Ge. Besides the total curve the contribution of each electron state is also shown separately. For this calculation the AS method with a state dependent GGA enhancement was used. The figure shows that depending on the momentum different electron shells yield the dominant contribution to the DBAR profile.

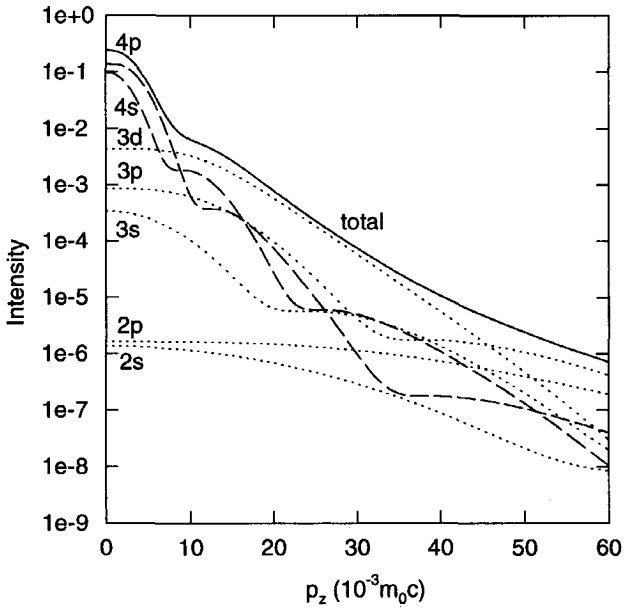

Figure 2.2: *DBAR (1D-ACAR) distribution in Ge and the separate contributions for each electron shell.*

The computer codes used for our atomic superposition calculations are based on the ones developed by Alatalo *et al.* [5]. The program solves the Dirac equation to obtain relativistic electron wave functions and charge densities for free atoms. A supercell is constructed by placing atoms at the appropriate lattice positions. Periodic boundary conditions are imposed at the supercell boundaries. The electron density of the solid is approximated by the superposition of charge densities of free atoms using the non-self-consistent, atomic superposition method of Puska and Nieminen [19]. The electron density and the positron potential are calculated at the node points of a three-dimensional mesh. Typically, $90 \times 90 \times 90$ node points are used. The Schrödinger equation is then solved to obtain the positron energy and the positron wavefunction at the node points. The annihilation rates are calculated using the GGA or LDA and the momentum distribution is calculated. This approach is essentially the same as used by Alatalo *et al.* [5] except that, as proposed by Ghosh *et al.* [21], the AS positron wavefunction (directionally averaged) is used in the calculation of the momentum density instead of using a fit to the positron wavefunction obtained by an LMTO calculation. The 'averaged' positron wavefunction can be easily extracted since the positron wave function is already calculated at all node points. It is also possible to use a position-dependent enhancement factor instead of the state-dependent enhancement since also the enhancement is known for all node points. The enhancement used strongly influences the calculated lifetime and the shape of the high-momentum part of the calculated momentum distribution. The shape of the central part of the momentum distribution is almost independent of the enhancement used [22]. To get an impression of the effects of the approximations used in the AS method we compared the results with those of KKR calculations. As a test case the momentum distribution of Al was calculated with three different enhancement functions. The KKR-based methodology is used as described by Mijnarends *et al.* [23]. Figures 2.3 and 2.4 shows that, although small differences exist, the KKR and AS results are very similar. The effects introduced by the enhancement function are larger than the differences between the KKR and AS results at high momenta.

2.4 Conclusions

The atomic superposition method provides a simple and fast scheme for calculating the high-momentum part of the momentum distribution. This makes the AS method a useful tool to support the interpretation of two-detector measurements. The method is not suited for calculating the contribution of the valence electrons to the momentum distribution, and the central part, $|p| < 20 \times 10^{-3}\ m_0 c$, of the momentum distribution is incorrectly calculated. The results of the AS method for the high-momentum part are however in good agreement with the results of KKR calculations. In chapters 5 and 6 experimental results are compared with the results of calculations.

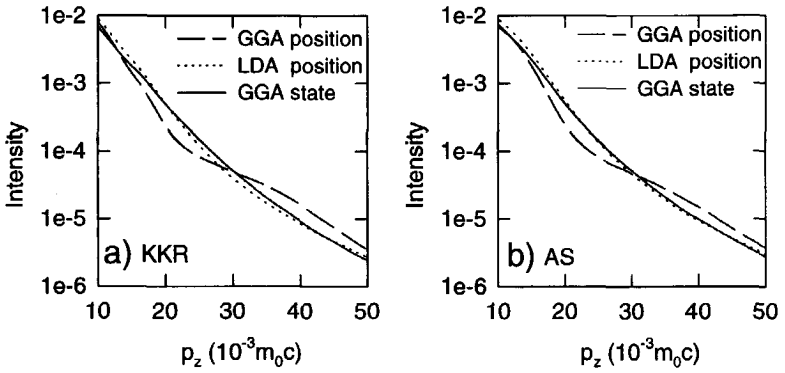

Figure 2.3: *The one-dimensional momentum distribution in Al as calculated by a) the KKR and b) the AS method using the GGA enhancement of Barbiellini et al. [15], the LDA enhancement of Puska et al. [10] (both position dependent) and the state dependent GGA enhancement of Barbiellini et al. [15].*

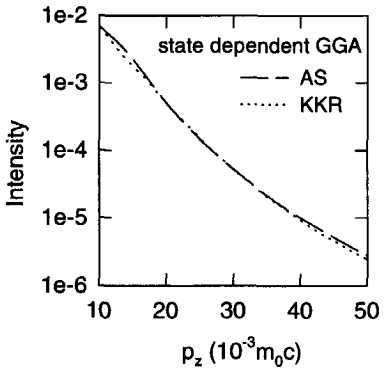

Figure 2.4: *The one-dimensional momentum distribution in Al as calculated by the KKR and AS methods using the state dependent GGA enhancement of Barbiellini et al. [15] (solid line) and the contributions for each electron state (dashed and dotted lines).*

References

[1] J. Korringa, *Physica* **13** (1947) 392.

[2] W. Kohn and N. Rostoker, *Phys. Rev.* **94** (1954) 1111.

[3] O.K. Andersen, *Phys. Rev. B* **12** (1975) 3060.

[4] H.L. Skriver, *The LMTO Method* (Springer, New York, 1984).

[5] M. Alatalo, B. Barbiellini, M. Hakala, H. Kauppinen, T. Korhonen, M.J. Puska, K. Saarinen, P. Hautojärvi and R.M. Nieminen, *Phys. Rev. B* **54** (1996) 2397.

[6] M.J. Puska and R.M. Nieminen, *Rev. Mod. Phys.* **66** (1994) 841.

[7] L. Lantto, *Phys. Rev. B* **36** (1987) 5160.

[8] E. Boroński and R.M. Nieminen, *Phys. Rev. B* **34** (1986) 3820.

[9] R.M. Nieminen and M. Manninen, in *Positrons in Solids*, ed. P. Hautojärvi, *Topics in Current Physics* **12** (Berlin, 1979) p. 145.

[10] M.J. Puska, A.P. Seitsonen and R.M. Nieminen, *Phys. Rev. B* **52** (1995) 10947.

[11] M.J. Puska, S. Mäkinen, M. Manninen and R.M. Nieminen, *Phys. Rev. B* **39** (1989) 7666.

[12] B. Barbiellini, M.J. Puska, T. Kornhonen, A. Harju, T. Torsti and R.M. Nieminen, *Phys. Rev. B* **53** (1996) 16201.

[13] R.O. Jones and O. Gunnarsson, *Rev. Mod. Phys.* **61** (1989) 689.

[14] T. Jarlborg and A.K. Singh, *Phys. Rev. B* **36** (1987) 4660.

[15] B. Barbiellini, M.J. Puska, T. Torsti and R.M. Nieminen, *Phys. Rev. B* **51** (1995) 7341.

[16] J.P. Perdew, *Physica B* **172** (1991) 1.

[17] J.P. Perdew, J.A. Chevary, S.H. Vosko, K.A. Jackson, M.R. Pederson, D.J. Singh and C. Fiolhais, *Phys. Rev. B* **46** (1992) 6671; **48** (1993) 4978(E).

[18] J. Arponen and E. Pajanne, *Ann. Phys.* (N.Y.) **121** (1979) 343.

[19] M.J. Puska and R.M. Nieminen, *J. Phys. F* **13** (1983) 333.

[20] R. Jastrow, *Phys. Rev.* **98** (1955) 1479

[21] V.J. Ghosh, M. Alatalo, P. Asoka-Kumar, K.G. Lynn and A.C. Kruseman, *Appl. Surf. Sci.* **116** (1997) 278.

[22] B.K. Panda, W. LiMing, S. Fung and C.D. Beling, *Phys. Rev. B* **56** (1997) 7356.

[23] P.E. Mijnarends, A.C. Kruseman, A. van Veen, V.J. Ghosh, P. Asoka-Kumar, A. Bansil, S. Kaprzyk and K.G. Lynn, *Mater. Sci. Forum* **255-257** (1997) 784.

Chapter 3

Experimental setup

3.1 Introduction

This chapter describes two newly built systems which enable us to improve the characterisation of defects in materials. The first system is a two-dimensional angular correlation of annihilation radiation system (2D-ACAR). The resolution is better than that of a DBAR system and it yields a two-dimensional momentum distribution while the DBAR technique only obtains a one-dimensional momentum distribution. In the near future the 2D-ACAR system will be placed in the recently constructed experiment hall and connected to the high-intensity, slow positron beam called POSH. The second system is an extension of the DBAR setup. A second Ge-detector is used to perform measurements in coincidence. This reduces the background by a factor of 100. The resulting peak to background ratio is better than 10^5 and opens the possibility of measuring the contribution of core electrons to the momentum distribution.

3.2 2D-ACAR

3.2.1 Experimental setup

In February 1995 the ACAR setup became operational in a temporary setting. Since at that time the POSH beam was in its preliminary testing phase, a conventional positron source was used. Figure 3.1 shows a top view of the setup. In the centre of the figure is the vacuum chamber and on top of that a lead container with the positron source. The two detectors are positioned on the left and the right. The detectors are mounted on rails which allows variation of the sample-detector distance. A larger sample-detector distance improves the resolution but at the cost of a lower count rate. In this section the different parts of the ACAR setup will be described.

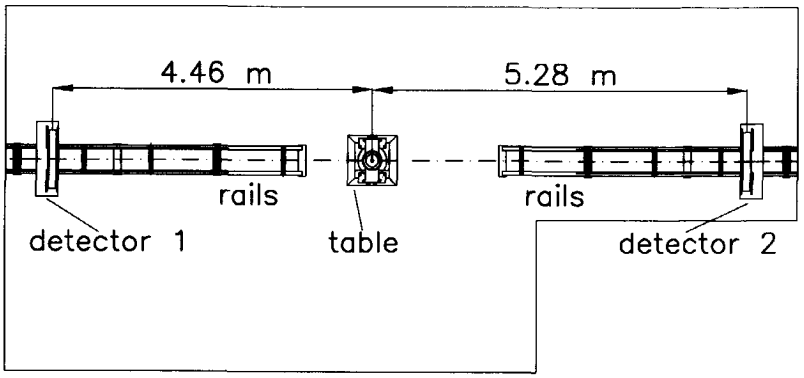

Figure 3.1: *Top view of the ACAR setup at the present location.*

3.2.2 Central part

The central part for use with a conventional source is shown in figure 3.2. It consists of a positron source, an electromagnet, a lead container and a vacuum chamber. The latter is mounted on a table which is adjustable in height to allow the alignment of the vacuum chamber with the centre of the detectors. A $3.9 \cdot 10^8$ Bq ^{22}Na source* of Du Pont is used. A large fraction of the emitted positrons will annihilate in the source itself. Approximately 20 % of the positrons is emitted into a 2π hemisphere. The source is mounted on a rod which fits into the bore of one of the poles of a water-cooled electromagnet. During sample mounting the source is raised into a lead container to avoid radiation exposure.

Annihilation in air reduces the positron intensity and gives erroneous information if the radiation is detected by the detectors. To avoid this the sample is placed in a vacuum chamber. The pressure in the vacuum chamber is $5 \cdot 10^{-2}$ mbar which is sufficiently low to avoid almost all annihilations in air. Lower pressures can be reached with the aid of a diffusion pump. For safety reasons the source is situated outside the vacuum chamber. A titanium foil of 5.5 μm is used to seal the window in the vacuum chamber. The transmission of the foil was experimentally determined to be 88 %. A cross-cut of the vacuum chamber is shown in figure 3.3.

The positrons emitted by the source have an energy distribution between 0 and 540 keV and angles between 0 and 90 degrees with respect to the vertical axis. A magnetic field is used to guide the positrons in helical trajectories towards the sample. This reduces the spot size of the positrons and increases the number of positrons that annihilate in the sample. The strength of the magnetic field depends on the current through the electromagnet and the distance between

*source strength in May 1996

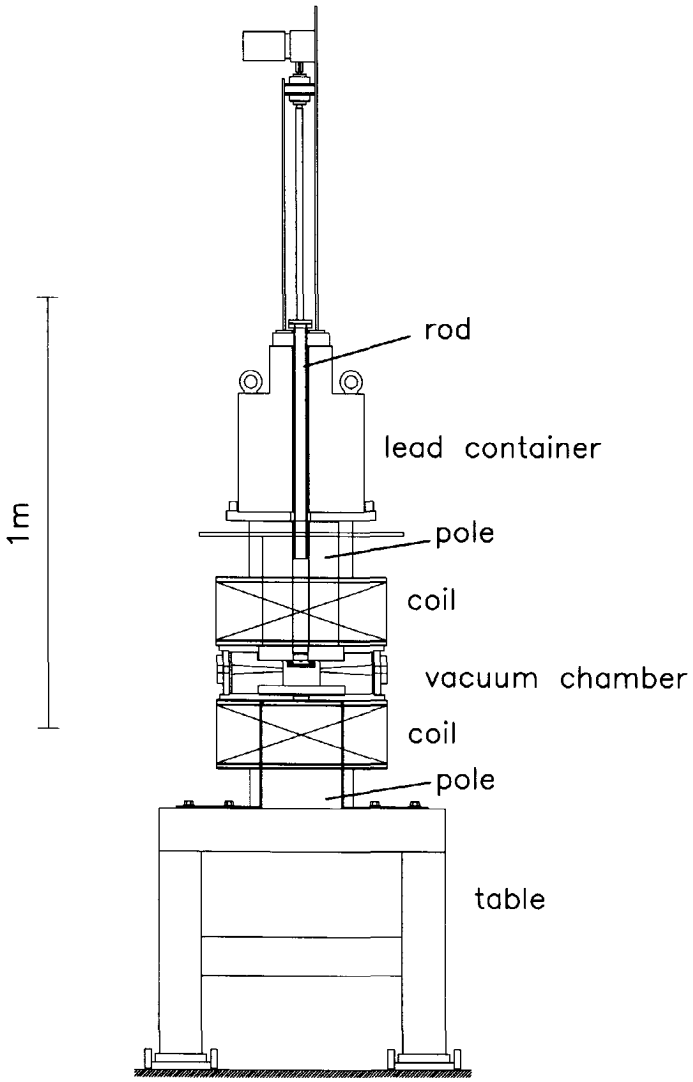

Figure 3.2: *Drawing of the central part of the 2D-ACAR setup.*

the poles (see figure 3.4). In the present setup the distance between the poles is 82 mm and the current is 14 A resulting in a magnetic field of 0.5 T. For this magnetic field the maximum radius of the helix is 6 mm. This maximum is only reached for positrons with the maximum energy and a direction perpendicular to the B-field. The average radius will therefore be sig-

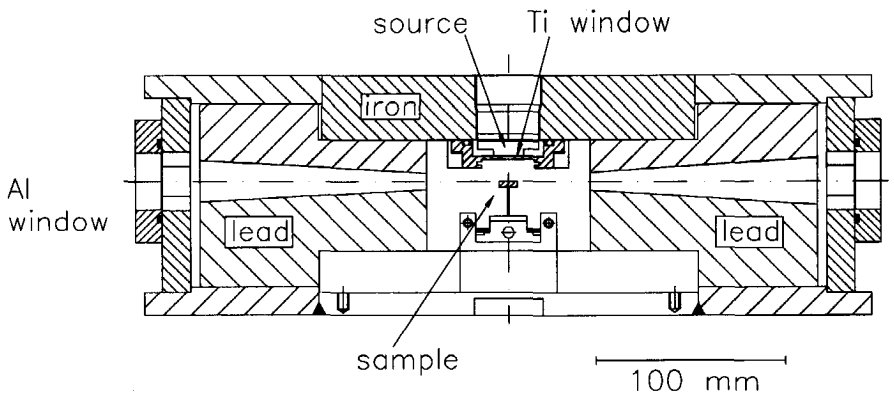

Figure 3.3: *Cross-cut of the vacuum chamber. The central part is rotated over 45°for the sake of clarity.*

nificantly smaller. A lead collimator is placed inside the vacuum chamber. The collimator only exposes the two detectors and shields the rest of the room from radiation. The annihilation radiation is emitted through an aluminium window in the direction of the detectors. The windows are 0.3 mm thick and have an transmission of 99 % for 511 keV annihilation radiation.

Since we are only interested in annihilation in the sample we should avoid annihilations in the sample mount. To achieve this the samples are mounted on top of small sticks. The samples used are thick enough to stop more than 99 % of the positrons and thereby shield the sticks from the positrons. The height of the sample is adjusted to be in line with the centres of the detectors and the lead collimators. Besides the height also the orientation of the sample is important. The momentum distribution reflects the crystallographic orientation of the sample. For the data analysis it is important that the orientation of the surface of the sample and one of the axes in the plane is known. The sample is rotated such that a known crystallographic axis is in line with the detectors. The rotational orientation of the sample is done by eye. The estimated error is between 1 to 3 degrees. In the present setup there is no equipment present for heating nor for cooling. All 2D-ACAR measurements described in this thesis are performed at room temperature.

3.2.3 Detectors

Three different types of detectors are commonly used for 2D-ACAR measurements: multi-detector systems [1, 2], Anger detectors with a NaI(Tl) crystal [3] and high-density multiwire chambers [4]. A description and a comparison of these different types of detectors can be found

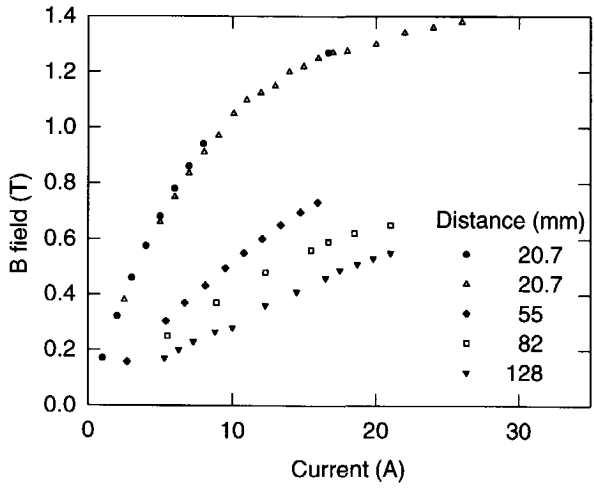

Figure 3.4: *The magnetic field at the sample position as a function of the current and the distance between the poles of the magnet.*

in Rabou *et al.* [5]. A compete overview of all design considerations of a 2D-ACAR system is given by West [6]. The detectors used for the present setup are of the Anger camera type [7] and have been purchased from AuRa Scientific. The data-acquisition system is based on the system developed by Lee at Brandeis University and further developed at the University of East Anglia, and was also bought from AuRa Scientific. The detector consists of a single NaI(Tl) crystal with a hexagonal shape and a thickness of 9.6 mm. The photomultiplier tubes (61) are optically coupled to the glass window of the crystal in a honeycomb formation. The edges of the crystal are shielded by a 27 mm lead ring leaving a circular area with a diameter of 0.418 m exposed to the radiation. All photomultiplier tube and pre-amplifier combinations are adjusted to have identical gain. A photon hitting the scintillator crystal will generate scintillations. These scintillations will be detected by several photomultiplier tubes. To obtain correct position information the signals of the photomultipliers are combined in the MIxer And Mother Interface (MIAMI) board. The signals are fed into summing resistor networks and four signals are produced (X,Y,Z,E). The E-signal is the combination of the signals of all the photomultiplier tubes and represents the energy of the photon. Only events with an energy of 511 $\pm$ 75 keV are processed. The X and Y signals are the position information in the x and y direction with respect to the detector. When the event has the correct energy the signal is clamped to provide a constant position signal with a duration of 4 μs. This constant signal is necessary for the processing of the signal by the data-acquisition electronics.

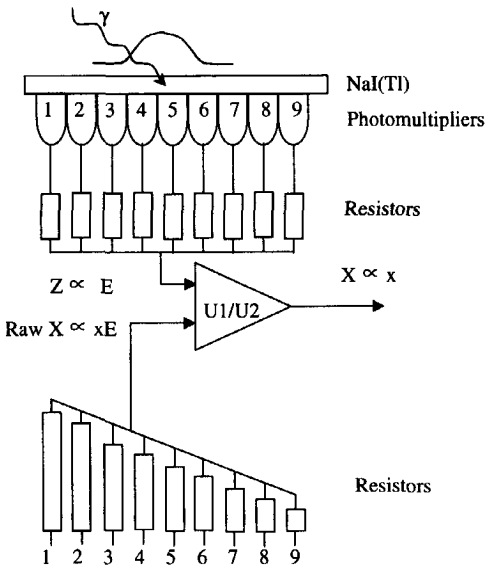

Figure 3.5: *Schematic diagram of the signal handling in the detector.*

The raw position signals contain statistical fluctuations. To reduce the effect of these fluctuations the Z signal (comparable to the E signal) is used to normalise the X and Y signals. A schematic diagram of the signal handling in the detector is shown in figure 3.5. The photon hits the NaI(Tl) crystal and creates scintillations which are detected by the photomultiplier tubes. The signals of the photomultiplier tubes are combined to yield the Z signal which only depends on the energy. Another resistor network is used to add the signals as a function of the position. This output signal (raw X) depends on the position where the photon hit the NaI(Tl) crystal and the energy. By dividing the two signals one obtains a signal that is only a function of the position.

The energy window used to exclude events with incorrect energies is also used to check the 511 keV peak position with respect to the internal reference voltages of the detector. The count rates in the upper and lower parts of the window are compared. A difference in count rate indicates a shift in the peak position. The difference is translated into a voltage and also shown by a red-green LED. A red or green colour indicates a shift of the peak. One high voltage power supply is used for all photomultiplier tubes of a detector. The peak position is adjusted by changing this high voltage. The operational voltage is around 700 V.

Figure 3.6 shows a block diagram of the 2D-ACAR data-acquisition electronics. Both annihilation gammas are detected by the Anger cameras. Each detector generates three signals: a trigger pulse (A/E) for each valid event and two analogue signals between -3 and 3 V representing the position in the horizontal (X) and vertical directions (Y) with respect to the detector. These position signals are fed into the data-acquisition electronics. The signals are amplified in the analogue interface and an offset of 5 V is added to obtain a signal between 0 and 10 V which is the operational range of the Analogue to Digital Converter (ADC). The four position signals are fed into a multiplexer. The signals of both detectors are adjusted such that the same voltage difference corresponds to the same difference in angle. The flank of the trigger pulse is used as timing for the coincidence condition. The coincidence window is set to 100 ns. A signal from the acquisition electronics inhibits the acceptance of new signals during the processing of the data. The coincidence unit generates a trigger pulse of 2 μs and the multiplexer stores the highest voltage during that period. These values are read one by one by the ADC, digitised into 12 bits and sent to an i486-PC with an Iguana data acquisition card. The software combines the four signals of the ADC and increases a counter at the appropriate position in a two-dimensional array of 256 $\times$ 256 channels. One channel corresponds to 0.49 mrad in the default setup of the system.

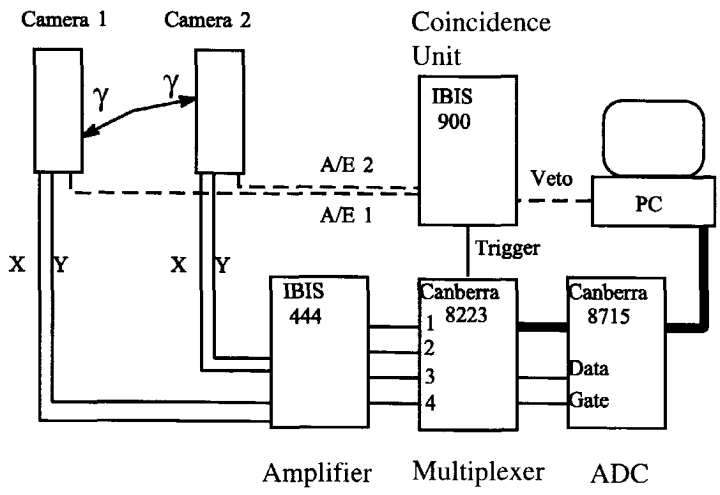

Figure 3.6: *Block diagram of the 2D-ACAR data-acquisition electronics.*

The NaI(Tl) crystal is very fragile. Temperature fluctuations therefore should remain less than 5 K/h. To protect the crystal from temperature influences of the sun the room is kept dark. After installation the system has proven to be very stable. Only a check of the red-green LED and an adjustment of the high voltage of the photomultiplier tubes once every month is sufficient as long as the power supply of the detector is not turned off.

After installation of the detectors the whole setup was aligned. The centre of the detectors and the lead collimators should be in line with the top of the sample. This alignment is performed with optical and mechanical aids. The vacuum chamber is placed between the poles of the electromagnet which is mounted on top of a table. The four legs of the table are adjusted to level the vacuum chamber. The detectors are mounted on two cradles which themselves are mounted on two rails. The detectors can be moved over the rails in a controlled manner. It has certain advantages to place the detectors at non-identical distances to the sample as will be explained in section 4.2. The cradle can be moved perpendicular to the rails. By adjusting two mounting pieces the height of the detector can be adjusted. For this adjustment a mechanical aid is needed to lift the detectors which have a weight of over 80 kg. The detector can be rotated over 360°.

3.2.4 Resolution

The resolution of a 2D-ACAR measurement consists of at least the following contributions:

- The resolution of the detector
- The dimensions of the annihilation volume in the sample
- The thermal motion of the positron

The first two contributions can be described as uncertainties in the detection and the annihilation position.

The finite size of the spot provides an uncertainty in the origin of the annihilation and the scintillation process in the NaI(Tl) crystal provides an uncertainty in the detection position. Let (x_0, y_0, z_0) be the origin of the annihilation radiation which is detected at (x_1, y_1, z_1) for detector 1 and at (x_2, y_2, z_2) for detector 2 (see figure 3.7). The components of the electron-positron momentum p_x and p_y, in the small angle approximation, are given by

$$p_x = \frac{x_1 - x_0}{z_0 - z_1} + \frac{x_2 - x_0}{z_2 - z_0} \tag{3.1}$$

$$p_y = \frac{y_1 - y_0}{z_0 - z_1} + \frac{y_2 - y_0}{z_2 - z_0} \tag{3.2}$$

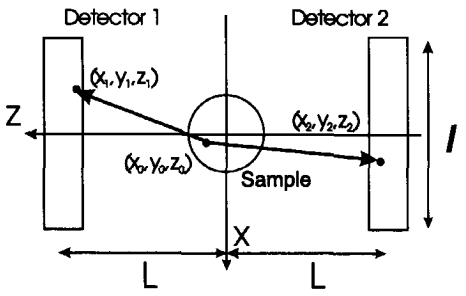

Figure 3.7: *Schematic top view of the ACAR setup. A positron annihilates at* (x_0, y_0, z_0) *and two annihilation photons are emitted. One is detected at* (x_1, y_1, z_1) *in detector 1 and the other at* (x_2, y_2, z_2) *in detector 2. The detector-sample distance is L and the detector dimension* l_d*. For the sake of clarity the dimensions of the sample and the detectors have been exaggerated.*

in which the z-direction lies along the line between the two detectors. The relative importance of the errors can be found by partial differentiation. The following results are obtained:

$$\frac{\delta p_x}{\delta x_0} = -\frac{1}{z_0 - z_1} - \frac{1}{z_2 - z_0} \propto \frac{2}{L} \tag{3.3}$$

$$\frac{\delta p_x}{\delta x_1} = \frac{1}{z_0 - z_1} \propto \frac{1}{L} \tag{3.4}$$

$$\frac{\delta p_x}{\delta x_2} = \frac{1}{z_2 - z_0} \propto \frac{1}{L} \tag{3.5}$$

$$\frac{\delta p_x}{\delta z_0} = -\frac{x_1 - x_0}{(z_0 - z_1)^2} + \frac{x_2 - x_0}{(z_2 - z_0)^2} \propto \frac{0.4 \cdot l_d}{L^2} \tag{3.6}$$

$$\frac{\delta p_x}{\delta z_1} = \frac{x_1 - x_0}{(z_0 - z_1)^2} \propto \frac{0.2 \cdot l_d}{L^2} \tag{3.7}$$

$$\frac{\delta p_x}{\delta z_2} = -\frac{x_2 - x_0}{(z_2 - z_0)^2} \propto \frac{0.2 \cdot l_d}{L^2} \tag{3.8}$$

with L the detector-sample distance and l_d the detector size. Analogous expressions are obtained for p_y by substituting all x by y. The average value for $|x_{1,2} - x_0| \approx 0.2 l_d$ due to the circular shape of the detector area. The contribution due to the uncertainty in the z-direction scales with l_d/L^2 while those of the x- and y-direction scale with L^{-1} The L^{-1} terms will dominate the contribution to the resolution for $L \gg l_d$. All contributions scale with the sample-detector distance. In the present, temporary setup the resolution of our system is poor compared with that of other 2D-ACAR systems in the world since our sample-detector distance is only 5 m, while 10 m is a more typical distance. In the experimental hall this situation improves and the sample-detector distance will be variable between 4.5 and 12.5 m.

Table 3.1: Uncertainties in the different co-ordinates, their source and the contribution to the resolution. The uncertainties in the z-direction contribute to the x- and the y-direction. A detector diameter of 0.42 m and a detector-sample distance of 5 m are assumed

Co-ordinate	Uncertainty Δ (mm)	Contribution Γ (mrad)	Source
x_0	4	1.7	spot size on sample
$x_{1,2}$	3.5	0.7	position resolution of the detector
y_0	0.1	0.03	implantation profile in sample
$y_{1,2}$	3.5	0.7	position resolution of the detector
z_0	4	0.03	spot size on sample
$z_{1,2}$	5	0.02	half of thickness of the NaI crystal

The contribution to the resolution function for co-ordinate c ($x_0, x_1, x_2, z_0, z_1, z_2$) is:

$$\Gamma_c = |\frac{\delta p_x}{\delta c}|\Delta c, \tag{3.9}$$

where Γ_c denotes the FWHM of co-ordinate c and Δc the uncertainty in co-ordinate c. The uncertainties in the different co-ordinates can be found in table 3.1. The contributions that scale with l_d/L^2 are small and do not significantly affect the system resolution. From table 3.1 it is also clear that the resolution is different for the x- and the y-direction. Both have a contribution from the uncertainty in the detection position but in the x-direction there is also a large contribution from the uncertainty in the x_0 position due to the spot size. In the y-direction this last contribution is smaller since the positron implantation depth in the sample is only of the order of 0.1 mm. This gives a contribution of only 0.03 mrad to the resolution in the p_y direction. The uncertainty in the p_x direction is equal to the spot size of the positrons. The spot size is determined by the size of source and the applied magnetic field. The source is 3×2 mm and since the maximum radius of the helical trajectories is 6 mm our spot size has a radius of $\sim$ 13 mm. The resolution can be improved by using a line source. Another way to reduce the beam spot is to reduce the size of the sample. This reduces the count rate but improves the resolution. Measurements were performed for different orientations of the source and a small line shaped sample. A variation of only 5 % in the count rate was observed. The almost circular spot size does not provide a preferential direction. Irradiation of photographical paper confirmed the circular shape. Usually the samples have a width between 6 and 10 mm. For a sample with a width of 7 mm a gaussian profile is assumed for the spot size with a FWHM of 4 mm; this yields a contribution to the resolution of 1.7 mrad.

The position resolution of the detector is determined by AuRa scientific to be 3.5 mm for 511 keV gamma-rays. This resolution can be checked by blocking one half of the detector with lead. Due to the finite resolution of the detector the cross-section of the single detector image will not show a sharp edge but an S-shaped curve as shown in figure 3.8. From the experimental data points a background component was subtracted and the intensity was normalised to the count rate at the side that was not shielded. The experimental data are compared to simulated spectra consisting of an edge convoluted with a gaussian function with a FWHM between 2.6 mm and 10.4 mm to include the effect of the resolution function. At the centre the experimental data agrees with the curves obtained after convoluting with gaussians of 3.1 or 3.9 mm FWHM. However, it is also clear that the experimental data has a long tail which cannot be obtained with a single gaussian resolution function. To get an impression of the real resolution function a combination of two gaussian components was tried. Figure 3.9 shows the result for the combination of 87 % of a gaussian with a FWHM of 3.1 mm and 13 % of a gaussian with a FWHM of 39 mm. Although the curve does not fit the data very well it becomes clear that the tail is caused by a low intensity ($\sim$ 10 %) broad (FWHM $\sim$ 40 mm) component in the resolution function. Figure 3.10 shows the para-positronium contribution in gypsum after subtracting the contributions of ortho-positronium and annihilations of free positrons. This figure is an approximation of the resolution function and also contains a low-intensity, broad component.

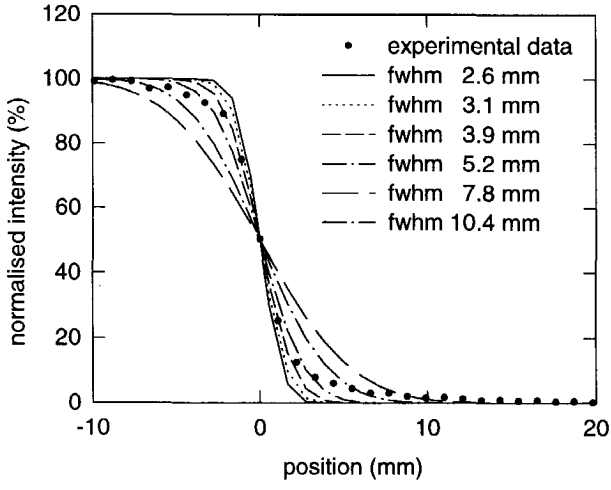

Figure 3.8: *Cross-section of a single detector image where one half of the detector is shielded by lead and simulations of this cross-section for several resolution functions.*

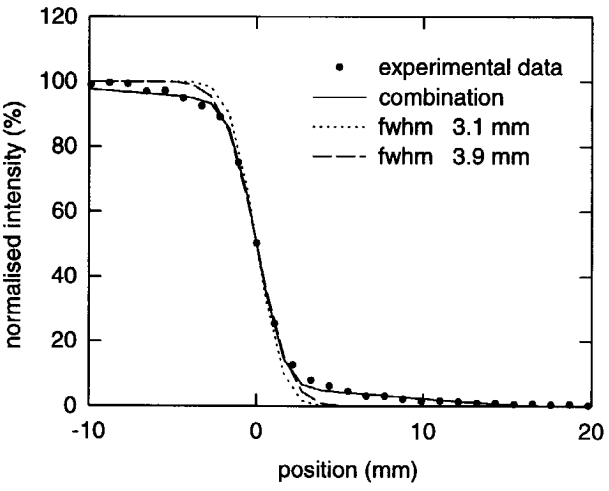

Figure 3.9: *Cross-section of a single detector image where one half of the detector is shielded by lead and simulations of this cross-section for two resolution functions with a FWHM of 3.1 mm and 3.9 mm and a resolution function that consists of two components with a FWHM of 3.1 mm (87 %) and 39 mm (13 %).*

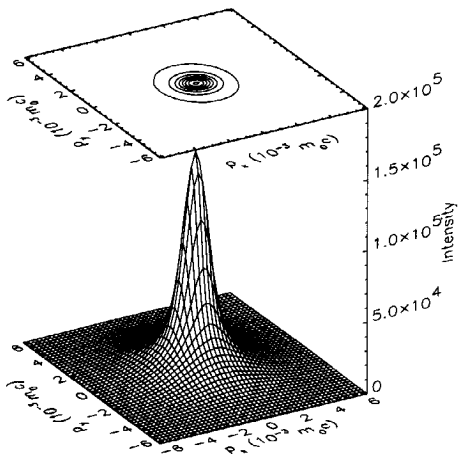

Figure 3.10: *Para-positronium contribution in gypsum.*

The thermal motion of the positron causes an additional smearing which is usually included in the resolution function. The positron momentum distribution can be described by the Maxwell-Boltzmann distribution which in atomic units is given by:

$$F(k_x,k_y,k_z) = (\frac{1}{2\pi m^* k_b T})^{3/2} e^{-(k_x^2+k_y^2+k_z^2)/(2m^* k_b T)}, \tag{3.10}$$

with m^* the effective mass of the positron (usually between 1 and 1.6 [8]), T the temperature and k_b the Boltzmann constant. The contribution of the positron momentum to the FWHM of the resolution function is:

$$\Gamma_{e^+} = 2\sqrt{(2m^* k_B T ln2)} \tag{3.11}$$

$$= 0.0306\sqrt{m^* T}\ [mrad\, K^{-1/2}]. \tag{3.12}$$

All our measurements are performed at 300 K. The positron motion contributes a smearing of 0.7 mrad for m^* = 1.6. High resolution ACAR measurements should therefore be performed at low temperatures since this contribution scales with $\sqrt{T}$.

Assuming gaussian contributions which are independent of each other, the overall resolution is:

$$\Gamma_{x,y}^2 = \sum_i \Gamma_i^2 \tag{3.13}$$

where Γ_i denotes the FWHM of the i^{th} contribution and $\Gamma_{x,y}$ the overall resolution in the x- or y-direction. Using the previously mentioned contributions we obtain $\Gamma_x = 1.2$ mrad and $\Gamma_y = 2.1$ mrad. Experimentally we can determine the resolution by measuring the width of the positronium peak in the ACAR-distribution. This peak is a delta-function broadened by the resolution function in which the contribution of the thermal motion of the positron should be replaced by the contribution for positronium. At 300 K the thermal motion of positronium contributes $\Gamma_{Ps} = 1.0$ mrad [9]. The measured resolution was $\Gamma_x = 1.7$ mrad and $\Gamma_y = 2.5$ mrad. In the p_x and p_y direction there is a large discrepancy between the measured and the calculated resolution. A contribution of 1.0 mrad, so far unaccounted for, would be necessary to explain the difference.

The discrepancy between the measured and the expected resolution can stem from a mismatch in the gain settings of the setup. To correctly add the signals of the detectors in the computer, it is necessary that one volt represents the same angle for both detectors. The output of a detector is fed into an amplifier unit to correct for the different detector-sample distances and the slightly different amplification in the hardware of the detector before the digitisation and computation of the angle. An incorrect amplification will make the resolution worse. Rotating both detectors over 90°did not show a difference in the resolution in the x- and y-direction for the positronium peak in quartz. If a mismatch is present it is identical for both directions. The settings were varied to determine the best resolution. Instead of adjusting the gain, the detector-sample

distance of one detector was varied while the other detector remained at a distance of 5.28 m from the sample. This is equivalent to adjusting the amplification factors of one detector for both directions simultaneously. Figure 3.11 shows the cross-section along the p_x axis through a number of 2D-ACAR measurements performed as a function of the detector-sample distance. All two-dimensional distributions are normalised to equal volume. The higher the central peak, the better the resolution is. Based on this measurement a sample-detector distance of 4.46 m would give the best resolution if the other detector is positioned at 5.28 m from the sample.

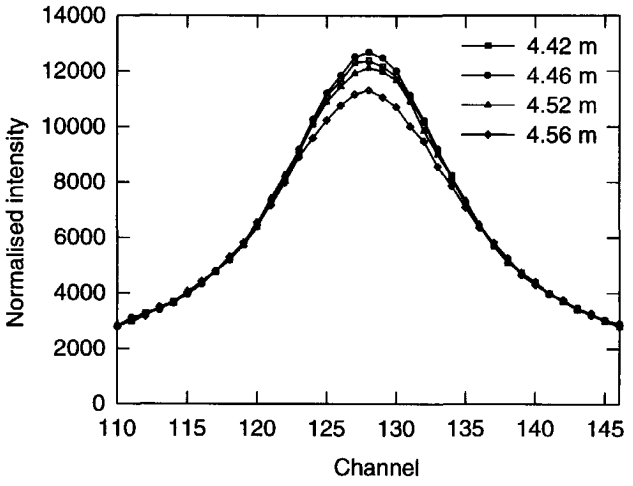

Figure 3.11: *Selection of cross-sections in the p_x direction at $p_y = 0$ of 2D-ACAR distributions for calcium sulphate as a function of the distance between detector 1 and the sample. The distributions are first normalised to equal numbers of counts. The curve with the highest top corresponds to the best resolution.*

With the 2D-ACAR setup we are measuring a once integrated three-dimensional distribution. Events detected at the edges of the detector have a slightly different integration direction compared with events detected at the centre of the detectors. West *et al.* [3] calculated the following criterion:

$$\Omega < (\delta\theta/\theta_{0.5})^2 \tag{3.14}$$

where $\theta_{0.5}$ is the FWHM of the momentum distribution, Ω the solid angle of a detector and $\delta\theta$ the resolution. When this criterion is met, only a modest degeneration of the effective momentum resolution would be present. The short sample-detector distances result in a large field of view and our ratio only just satisfies the criterion.

At the moment we do not have an explanation for the discrepancy between the measured and the expected resolution. West [6] mentioned that a combined position resolution of $\sqrt{2}\Gamma_s$ (with Γ_s the single detector resolution) is rarely achieved in practice with position sensitive detectors as a consequence of nonlinearities in their intrinsic position response. It is more realistic to assume a combined resolution of $2\Gamma_s$. The consequence is that instead of using $\Gamma_{1,2} = 0.7$ mrad one should use $\Gamma_{1\&2} = 1.4$ mrad. Assuming this new value a resolution of $\Gamma_x = 1.7$ and $\Gamma_y = 2.4$ mrad can be expected. This is in very good agreement with the experimentally obtained values of $\Gamma_x = 1.7$ and $\Gamma_y = 2.5$ mrad. The conformation of this relation is easier to determine in a setup with a larger sample-detector distance (as for example in the experiment hall) than with the present setup. The positronium peak in the ACAR distribution will be sharper with a longer sample-detector distance and a more accurate resolution determination is possible. Furthermore, the effect of the unknown contribution can be investigated as a function of the sample-detector distance. This reveals whether the contribution scales with the distance or is a constant.

3.2.5 Count rate

The number of counts expected in a single detector is:

$$N_{single} = 2N_+ t_+ (1-R) t_\gamma \varepsilon \frac{\Omega}{4\pi} \tag{3.15}$$

with N_+ the number of positrons emitted by the source in the direction of the sample, t_+ the fraction of positrons transmitted from the source to the sample, R the backscatter coefficient of the sample, t_γ the transmission of annihilation radiation from the sample to the detector, Ω the solid angle of the detector and ε the efficiency of the detector for detecting 511 keV photons. In the present setup with $N_+ = 6.4 \cdot 10^7$ e^+/s (September 1996), $t_+ = 0.88$ (transmission through the Ti-foil and the air between the source and the Ti-foil), a backscatter coefficient of 0.2, $t_\gamma \sim 0.9$ (including the transmission through the Si sample, the Al windows, the polystyrene shielding of the detector area and the air between the sample and the detector) and an efficiency of the detectors of 0.08 for 511 keV photons a single count rate of $3.5 \cdot 10^3$ was expected for detector 1. The measured count rate for detector 1 was $3.3 \cdot 10^3$ which is in good agreement with the expected count rate based on equation 3.15.

The coincident count rate is equal to:

$$N_c = 2N_+ t_+ (1-R) t_{\gamma,1} t_{\gamma,2} \varepsilon_1 \varepsilon_2 \chi \frac{\Omega}{4\pi} \tag{3.16}$$

$$= N_{single,1}\, \varepsilon_2\, t_{\gamma,2}\, \chi_{21} \tag{3.17}$$

$$= N_{single,2}\, \varepsilon_1\, t_{\gamma,1}\, \chi_{12} \tag{3.18}$$

Table 3.2: Main characteristics of the 2D-ACAR setup in September 1996.

effective detector size	circular d=418 mm
	0.137 m^2
detector-sample distance (L1)	4.46 m
(L2)	5.28 m
field of view detector 1	6.9 msr
field of view detector 2	4.9 msr
data array size	256 × 256 channels
angle / channel	0.49 mrad
field of view momentum distribution	123 × 123 $mrad^2$
measured resolution p_x at 300 K	2.5 mrad (FWHM)
measured resolution p_y at 300 K	1.7 mrad (FWHM)
detector efficiency	8 %
coincidence time	100 ns
single detector count rate	$3 \cdot 10^3\ s^{-1}$
single detector background	$3 \cdot 10^2\ s^{-1}$
count rate coincidences	$2 \cdot 10^2\ s^{-1}$
background coincidences	$2.1\ s^{-1}$
background coincidences (source removed)	$2 \cdot 10^{-3}\ s^{-1}$

with 1,2 indicating the detector, N_c the coincident count rate, ε_i the efficiency of detector i and χ the geometric detection efficiency factor, which is a function of the solid angles of the detectors and the width of the momentum distribution [3]. In our setup in which the detectors have different solid angles, χ_{12} is close to 1 and χ_{21} is 0.7. Using the single count rate as measured, the coincidence rate should be $2 \cdot 10^2$, which is in agreement with the measured count rate.

The accidental coincidence rate is:

$$N_{acc} = 2\tau N_1 N_2 \tag{3.19}$$

with τ the width of the coincidence window and $N_{1,2}$ the single count rate of detector 1 and 2. According to this expression $1.9\ s^{-1}$ could be expected. This value is close to the observed count rate of $2.1\ s^{-1}$.

3.2.6 Artifact

The first measurements showed a strange artifact. The high channels in the x and y-direction showed an increased intensity. Figure 3.12 shows a schematic representation(contour diagram) of a measurement. The concentric circles in the centre represent the 2D-ACAR distribution and the two tails are the artifact. The intensity in a channel of the artifact is in the order of 0.01 of the peak intensity. Such an artifact can be created if three of the four position signals are valid and one is apparently too high. In one direction the angle is correctly calculated, in the other direction it is incorrect. It was noticed that the presence of the artifact was influenced by the amplification and offset used in the IBIS 444 analogue interface unit.

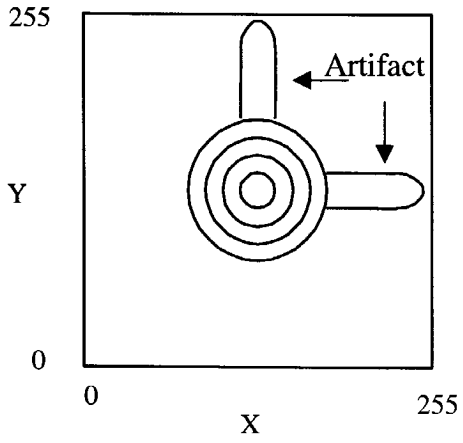

Figure 3.12: *Schematic image of a measurement. X is the angle in the p_x direction and Y the angle in the p_y direction. The artifact consists of two tails in the high channel directions.*

The artifact is caused by an incorrect operation of the multiplexer. The multiplexer is used to digitise the four position signals of the detectors with only one ADC. A trigger pulse will start four peak-detect-and-hold circuits. During the presence of a trigger pulse the **highest** value is stored. Figure 3.13 shows the signals during correct operation. Not all scintillations stem from 511 keV annihilation photons. The detector hardware contains an energy selection part and only photons within an energy window are processed. Events outside the window still generate an output signal but the duration of the signal is shorter and there is no accompanying trigger pulse. Input signals below a lower level setting (LLD) are not processed. It appears however

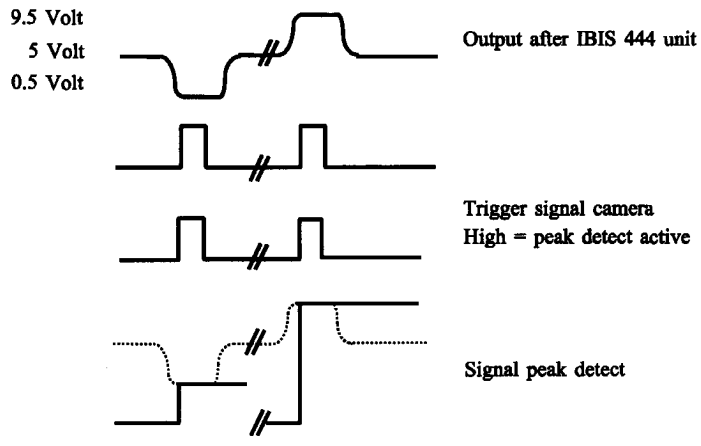

Figure 3.13: *Response of the peak-detect-and-hold circuit for a 'low' and a 'high' value. Events at the center of the detector correspond to a voltage of 5 volt.*

that input signals that are below the LLD but rise above this setting will activate the peak detect and hold circuits! The circuits will operate until a correct trigger pulse is received. During this time interval the highest value is stored. If a higher signal occurred during this period this value is digitised by the ADC. The calculated angle will then be to large. In figure 3.14 two examples are shown of incorrect operation of the peak-detect-and-hold circuits. When the setup is operating in coincidence mode the multiplexer receives only a trigger signal from the coincidence unit when both detectors have detected a valid event (both generated a trigger pulse). The single count rate is 15 times higher than the coincident count rate. The input signal of the multiplexer contains a large fraction of the pulses that are not accompanied by a trigger pulse of the coincidence unit. In figure 3.15 the relevant signals are shown. Due to a pulse that drops below the LLD and rises again above this setting the peak-detect-and-hold circuit is activated. Three valid signals are received and processed by the circuit. In the first three events for detector 1, detector 2 did not detect a pulse and the coincidence unit did not start the multiplexer. The fourth event does generate the trigger pulse and the signals are processed but since the second pulse was higher than the fourth pulse, the value of the second pulse is stored in the peak-detect-and-hold circuit and digitised.

We have solved this problem by building a new amplifier unit to replace the IBIS 444 analogue interface unit. In the new amplifier a negative output signal is clamped to 0 V. No pulses below 0 V will be passed to the multiplexer. Figure 3.16a is an example of a measurement

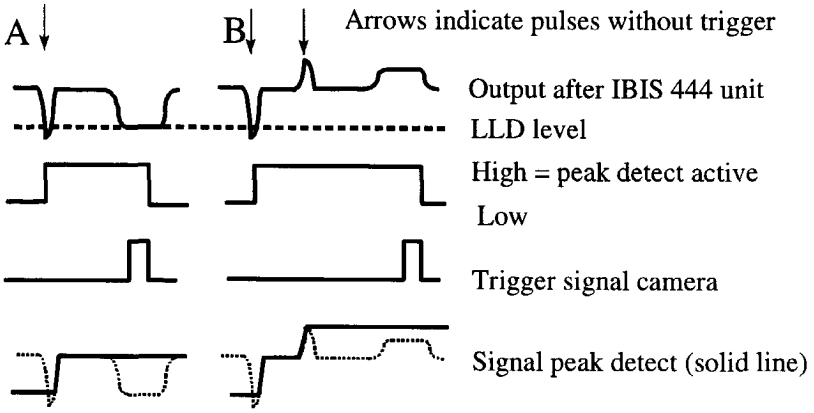

Figure 3.14: *Two examples of incorrect peak values. The peak-detect-and-hold circuit is started by a short pulse below the LLD level.*

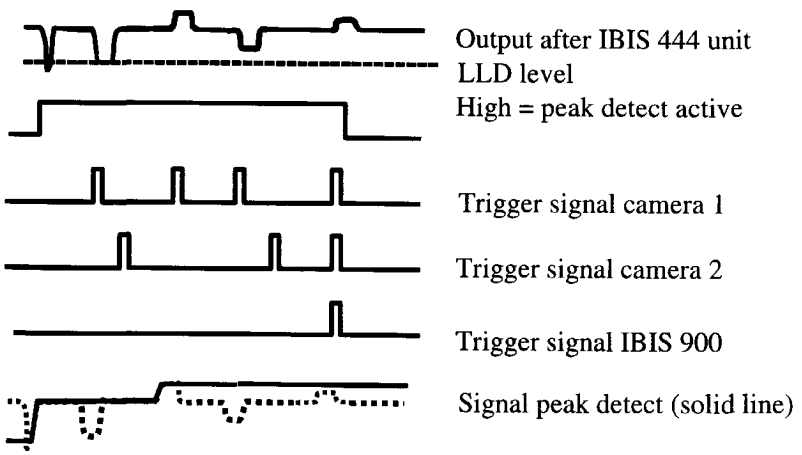

Figure 3.15: *Signals in coincident mode. An 'invalid' pulse starts the peak-detect-and-hold circuit. The circuit is not stopped until both detectors give a trigger pulse. Note that the time scale is compressed and that the time between two pulses is longer under our measurement conditions.*

performed with the old setup. Figure 3.16b shows a measurement of the same sample with the new amplifier unit in which one can see that the artifact is indeed removed.

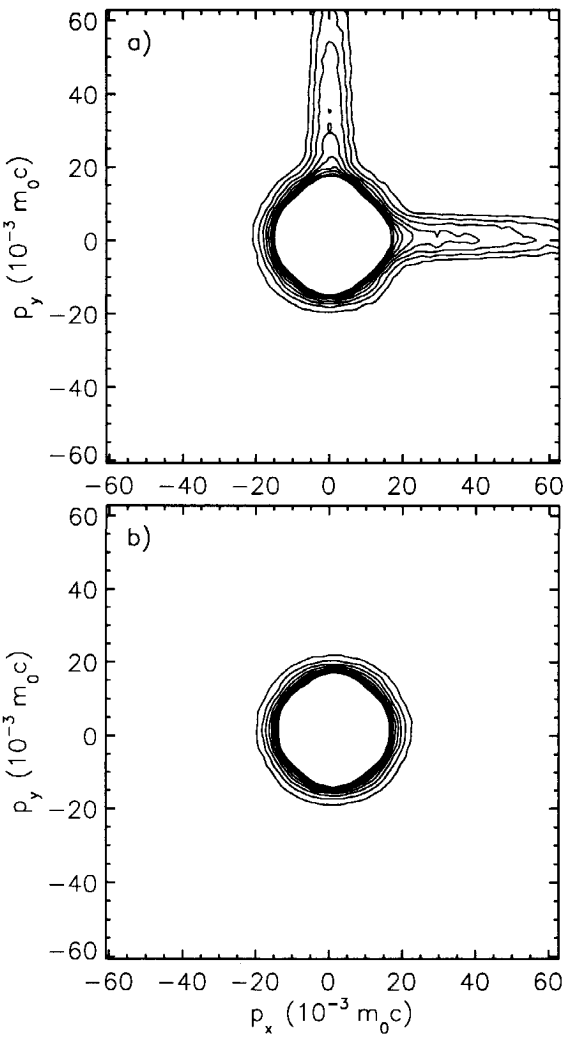

Figure 3.16: *Two measurements on the same Si sample: a) a distribution obtained with the original amplifier unit and b) a distribution obtained with the new amplifier with clamping. The contour lines are separated by 1/2000th of the maximum value.*

3.2.7 Experiment hall and POSH

The present ACAR setup is limited to bulk measurements since unmoderated positrons are used. For depth profiling a high-intensity beam of slow positrons is necessary. The high-intensity POSH beam is in its last phase of development and is based mainly on pair production by high-energy photons in the HOR reactor of the Interfaculty Reactor Institute. Figure 3.17 shows the design of the source of the POSH beamline. The tungsten foils are used as a high Z material for pair production and as a moderator of the created positrons. Electrodes are used to extract the positrons from the source, and the beam is magnetically guided to the 2D-ACAR system or the micro-analysis apparatus. The test in the summer of 1997 yielded already 8×10^7 positrons/s at full reactor power (2000 kW). Test with an improved source design and at low reactor powers have shown that the yield is increased by a factor of four putting it well above the design value of 10^8 positrons/s.

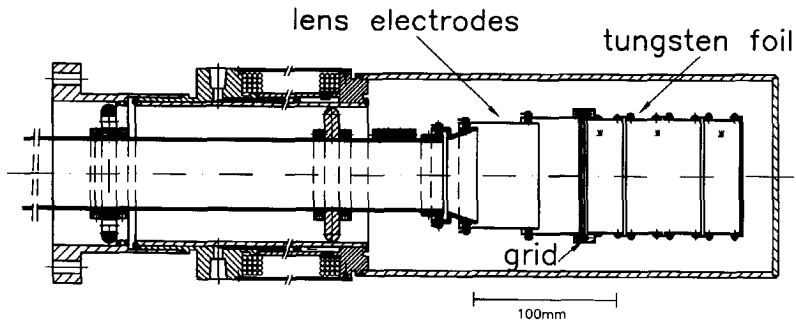

Figure 3.17: *Setup of the positron source of the POSH beamline.*

The initial beam size will be 10 mm FWHM at 2 keV. To improve the resolution of the 2D-ACAR setup a reduction of the beam size to 1 mm is preferable. It is only necessary to reduce the dimension of the beam spot perpendicular to the detector-detector line since this dimension has a large influence on the resolution of the setup. An elliptical spot with a short axis of 1 mm and a long axis of 10 mm would be fine. A long axis of more than 10 mm results in the loss of intensity as a fraction of the positrons miss our sample which typical have the dimensions of 10 mm $\times$ 10 mm. The final stage of the POSH beam will be electro-statically guide to the 2D-ACAR setup and since we are only interested in a small spot size and not in the quality of the spot (e.g. aberration) a simple quadrupole could be sufficient to focus the beam without severely reducing the beam intensity.

At the present location the maximum detector-detector distance is 10 m. In the recently completed hall more space is available for the 2D-ACAR setup. Detector-detector distance of up to

25 m can be used. A detector-detector distance of 25 m will improve the position resolution of the detectors by a factor of 2.5. This will also considerably improve the resolution of the ACAR setup since the position resolution is an important contribution to the resolution function of the ACAR setup. In combination with a smaller spot size resolutions better than $1 \times 10^{-3}\ m_0c$ in both directions could be obtained. This enables us to perform measurements with a better resolution, although at the cost of a reduced count rate. The better resolution makes it easier to observe differences between measurements, thus improving the abilities for defect identification.

The vacuum requirements for bulk and depth profile measurements are quite different; consequently the vacuum chamber used for the bulk measurements is not suited for surface measurements. A new vacuum chamber will be used for the measurements with the POSH beam. The new vacuum chamber and the vacuum chamber used for the present setup will be placed in the experiment hall. The two position-sensitive detectors and the data-acquisition system will be common to the beam-based and the source-based setup. Figure 3.18 shows the 2D-ACAR section of the hall. This provides us with two possible positron sources: one based on the POSH beam for depth profiling and one based on an unmoderated positron source for measurements on bulk materials.

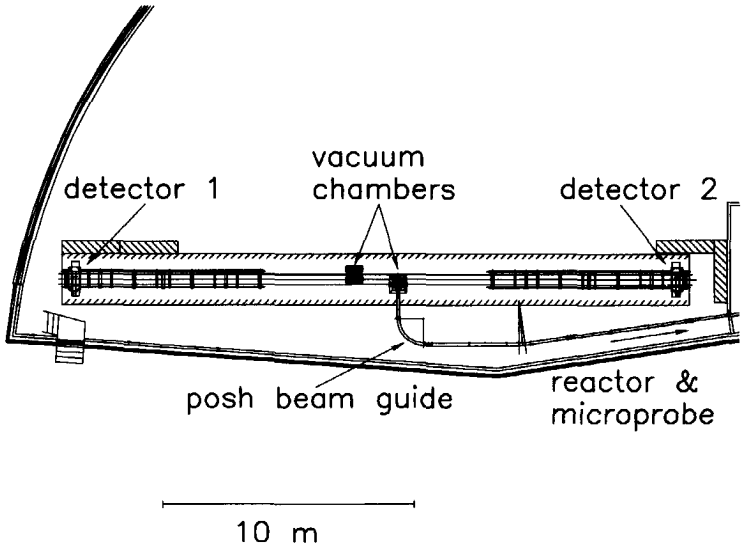

Figure 3.18: *The 2D-ACAR section of the hall.*

3.3 Two detector Doppler broadening

3.3.1 Introduction

Lynn *et al.* [12] recognised the advantages of using a combination of two Ge-detectors to perform Doppler broadening measurements. The advantages are an important reduction of the background and an improved resolution. The two Ge detectors are used in coincidence and positioned collinearly with the sample. Both the annihilation photons are measured. Let E_1 and E_2 be the energies measured by detector 1 and detector 2. The energy of one annihilation photon is shifted upward by $cp_z/2$, that of the other photon is shifted downward by $cp_z/2$, with c the velocity of light and p_z the momentum component of the positron-electron pair in the direction of the detectors. When the two photons are detected within the time window this event is stored in a two-dimensional array. It is then useful to define two other energies: the sum, $E_s = E_1 + E_2$, and the difference, $E_d = E_1 - E_2$. The sum energy E_s is equal to the total energy of the positron-electron system before annihilation. For thermalised positrons this is equal to $2m_0c^2 - E_B$, where m_0 is the rest mass of the electron and E_B is the binding energy of the electron and the positron in the solid. The difference energy, E_d, is equal to cp_z. Both detectors measure the same energy shift so we measure twice the Doppler shift. Since the two detection processes themselves are not correlated the resolution of this measurement is $\sqrt{\sigma_1^2 + \sigma_2^2}$, with σ_i the resolution of the single detectors. For two identical detectors an improvement of $\sqrt{2}$ is obtained.

Figure 3.19 shows an example of a two-dimensional spectrum. The gray tone indicates the number of counts on a logarithmic scale. The central peak is caused by events in which two photons are detected with only a small Doppler shift. The four broad bands extending from the center in the vertical and horizontal directions are coincidences of one "background" photon with a 511 keV photon. The elliptical region with the long diagonal axis reflects the distribution of p_z. By taking a cross-section along the diagonal line $E_1 + E_2 = constant = 2m_0c^2$ and with a small width we can avoid almost all background, thus improving the peak to background ratio by a factor of 100.

3.3.2 Experimental setup

The system consists of two high-purity Ge detectors, amplifiers, analogue to digital converters (ADC), a busbox and a computer system (see figure 3.20). We use a variable energy positron beam as a positron source. The Ge detectors are positioned collinearly with the sample; the distance between the sample and each detector is 4 cm. Different combinations of Ge-detectors have been used. The energy resolution of each detector is 2.2 keV (FWHM) for the 1.33 MeV gamma ray of ^{60}Co, using a shaping time of the spectroscopy amplifiers of 3 μs. The relative

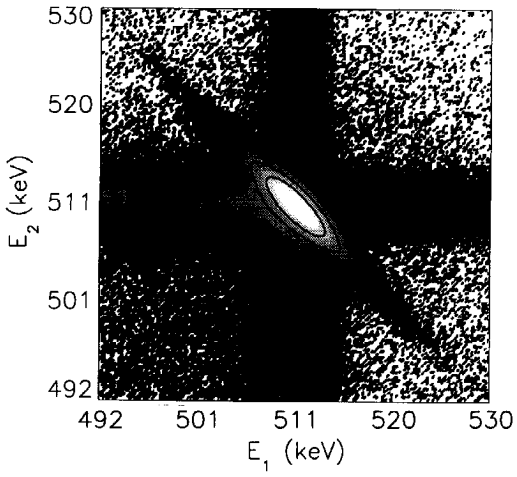

Figure 3.19: *Two-dimensional spectrum of pure tungsten. E_1 denotes the energy measured by detector 1 and E_2 that by detector 2. The gray scale represents the number of counts on a logarithmic scale. Contour lines are drawn at 3,30,300 and 3000 counts.*

efficiency for the photo peak compared to a NaI(Tl) detector is between 25 % and 35 %.

After amplification and digitisation the data are fed into a busbox which contains the coincidence electronics. The coincidence time window is set to the shortest setting of 0.35 μs. This reduces the background compared to longer settings without a decrease in the count rate in the peak. The pile-up rejection signal of the spectroscopy amplifier is used to gate the ADC. Typical measurements take several hours with a coincident count rate of 200 c/s in the peak. The count rates of the single detectors are 10 times higher. The response of each of the detectors is adjusted such that one channel corresponds to a momentum of $0.580 \times 10^{-3}\ m_0c$.

3.3.3 Background

In a conventional, one-detector, Doppler broadening measurement the background consists of several contributions. The background for energies above 511 keV consists of sum events, pile-up and radiation from sources other than the annihilation process itself, such as Compton scattered 1.274 MeV photons (also emitted by ^{22}Na). The pile-up can be minimised by using a short shaping time and a pile-up rejection circuit. The penalty for a shorter shaping time is a worsening of the resolution of the system. The background below 511 keV contains contribu-

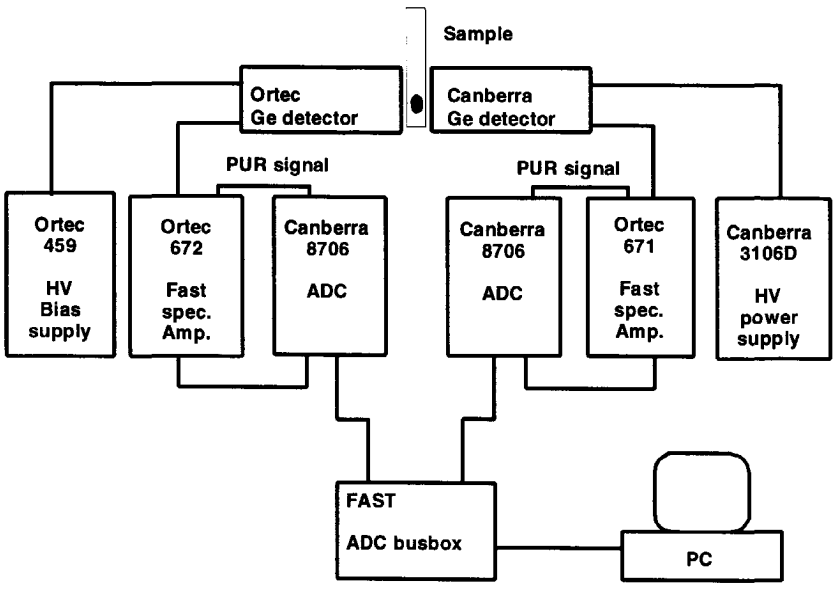

Figure 3.20: *Block diagram of the experimental setup.*

tions from 511 keV photons which are Compton scattered outside the detector, events with an incomplete charge collection in the detector and events due to radiation from other sources. The radiation from other sources can be reduced by shielding. If positronium formation is possible, three gamma decay will also contribute to the background. All contributions mentioned above will occur, but the fraction of each contribution to the total background is system dependent. A system with a low intensity beam will have a smaller fraction of the background coming from sum and pile-up events than a high intensity beam.

The use of a coincidence circuit reduces the background. In our setup the peak to background ratio improved from 7.7×10^2 to 1.2×10^3 (high-energy side). However, the background is only partly removed by the coincidence circuit since a part of the "background" is coincident. These events can only be filtered out by using the energy relation between both photons. A diagonal cross-section of the two-dimensional spectrum is made with a width of ($2m_0c^2 - 1.3$ keV $< E_1 + E_2 < 2m_0c^2 + 1.3$ keV). This results in a peak to background ratio of 10^5, i.e. an improvement by a factor of 100. Compared to a single-detector system without any pile-up rejection the peak to background ratio is even improved by a factor of almost 1000. The diagonal

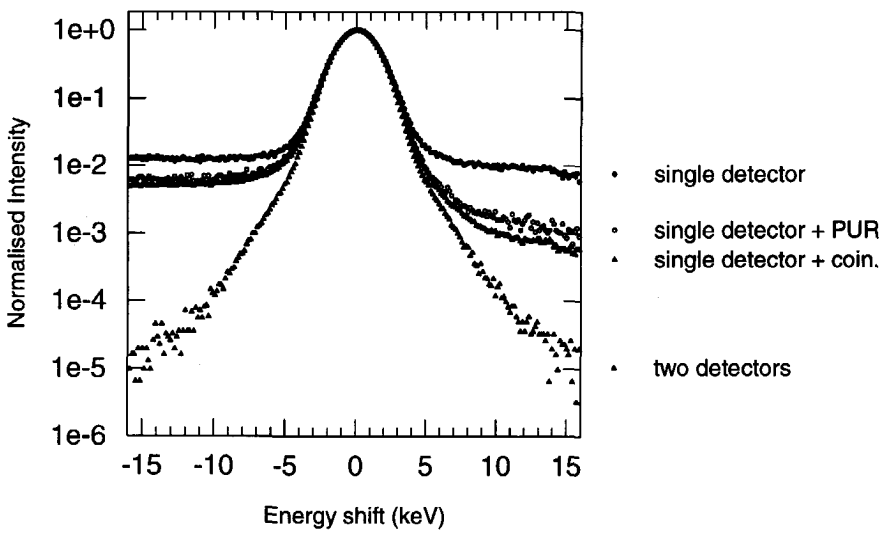

Figure 3.21: *The measured energy spectrum of the annihilation peak under different conditions: the one-detector spectrum without pile-up rejection(filled circles), with pile-up rejection(open circles), the one-detector spectrum of events which satisfy the coincidence condition in combination with pile-up rejection(filled triangles) and the diagonal cross-section of a two-dimensional spectrum(open circles). All spectra are normalised to a peak height of 1.*

cross-section contains $\sim$ 90% of the total number of counts. Figure 3.21 shows the Doppler-broadening curves for the different setups. Note also the symmetrical shape of the Doppler broadening curve obtained by taking a cross-section through the two dimensional spectrum.

Figure 3.19 has four quadrants. The quadrants are separated from each other by broad vertical and horizontal bands. A reference to a particular quadrant means the area of that quadrant excluding the broad bands. The background in the quadrants is very low, but so is the intensity of the high momentum tail. Especially in the top-left quadrant and the bottom-right quadrant we want to minimise the background. A part of the background will stem from accidental coincidences not related to annihilations. This contribution is present in the entire area of the two-dimensional spectrum. To minimise these accidental coincidences we use the smallest coincidence window possible. The other contribution to the background in the quadrants comes from coincidences of a "background" photon with a photon of an energy a few keV

higher or lower than m_0c^2. This second photon can be another "background" photon or a photon resulting from an annihilation with a core electron. In the two-dimensional spectrum the cross-section with $E_1 = constant$ will have a distribution that resembles the distribution of the one-dimensional spectrum of detector 2. The cross-section with $E_2 = constant$ resembles that of the one-dimensional spectrum of detector 1. This dependence is the cause for the different intensities in the four quadrants. The bottom-left quadrant has the highest intensity and the top-right quadrant has the lowest intensity since the low-energy background in the one-dimensional spectra is higher than the high-energy background. The background in the four quadrants will be reduced if one can reduce the background in the one-detector spectra.

3.3.4 Resolution

The energy resolution (related to the 511 keV annihilation photo peak) which can be achieved theoretically is at most a factor of $\sqrt{2}$ better than that of a one-detector spectrum. A good approximation of the resolution of the two-detector system can be obtained by taking a cross-section of the two-dimensional spectrum along a diagonal with $E_1 - E_2 = 0$. The resolution of the system is 0.9 keV (FWHM), while a single detector with identical settings would have a resolution of 1.3 keV at the 511 keV annihilation photo-peak. Although the cross-section looks like a single peak, it is in fact a combination of delta functions, each broadened by the resolution function and shifted by the binding energy of a particular group of electrons. A large fraction of the annihilations occurs with valence electrons. Matsui [14] measured the average binding energy for Al as observed by positrons to be 9 eV. This is small compared to the resolution of the system (0.9 keV FWHM at 511 keV). The cross-section can be used to monitor the system, but it does not constitute a universal response function of the system valid at all energies. Annihilations with core electrons will deform the sum peak somewhat and shift it to lower energies. A cross-section at $E_1 - E_2 \neq 0$ will contain a larger fraction of annihilations with core-electrons, resulting in a downward shift of the peak centroid. MacDonald *et al.* [15] observed this shift for Al.

The resolution of the setup is dependent on the shaping factor used in the spectroscopic amplifiers. To avoid timing problems within the coincidence circuit identical shaping times for both amplifiers should be used. An improvement in the resolution can be achieved by using a longer shaping time as one can see in table 3.3. The disadvantage of a longer shaping time in combination with a pile-up-rejection circuit is the decrease in count rate. A shaping time of 3 μs is used. With this shaping time an improvement in resolution was achieved compared to the single-detector setup without a severe reduction in count rate.

Table 3.3: The resolution and the count rate as a function of the shaping time used for our two-detector Doppler-broadening system.

Shaping times (μs)	Resolution (FWHM in keV)	Count rate (s^{-1})
1	2.24	190
2	1.12	180
3	0.90	160
6	0.85	90

3.3.5 Conclusions

The advantages of the two-detector setup are first of all an important reduction of the background and secondly an improved resolution. The former makes it possible to perform accurate measurements of the contribution to the momentum distribution of annihilations with core electrons. The peak to background ratio is improved by a factor of 100 compared to a single-detector system with a pile-up rejection circuit. The achieved resolution of the system of 0.9 keV (at 511 keV) is better than the 1.3 keV which a single detector in combination with an amplifier with a shaping time of 3 μs would have had. The resolution is even better than the 1.1 keV resolution obtained with a single detector and an amplifier with a shaping time of 6 μs.

In the present setup the main interest is to investigate the high-momentum region. Settings with a better counting efficiency are therefore preferred over those with a better resolution since for each point in the two-dimensional array both photons should be detected.

References

[1] S. Berko, M. Haghgooie and J.J. Mader, *Phys. Lett. A* **63** (1977) 335.

[2] S. Tanigawa, R. Suzuki and Y. Iwase, in *Positron Annihilation*, Proceedings of the 7th International Conference on Positron Annihilation, eds. P.C. Jain, R.M. Singru and K.P. Gopinathan (World Scientific, Singapore, 1985) p. 839.

[3] R.N. West, J. Mayers and P.A. Walters, *J. Phys. E* **14** (1981) 478.

[4] A.P. Jeavons, D.W. Townsend, N.L. Ford, K. Kull, A. Manuel, Ø. Fisher and M. Peter, *IEEE Trans. Nucl. Sci.* **NS-25** (1978) 164.

[5] L. Rabou, P. Zwart, G.J. Langedijk and P.E. Mijnarends, *Panda II, An apparatus for positron annihilation angular correlation measurements in two dimensions*, ECN report 211 (1988).

[6] R.N. West, in *Positron Spectroscopy of Solids* , Proc. of the International School of Physics "Enrico Fermi", Course CXXV, eds. A. Duasquier and A.P. Mills jr. (IOS press, Amsterdam, 1995) p. 75.

[7] H.O. Anger, *Rev. Sci. Instr.* **29** (1958) 27.

[8] P. Kubica and A.T. Stewart, *Can. J. Phys.* **61** (1983) 971.

[9] A. Dupasquier, in *Positron Spectroscopy of Solids* , Proc. of the International School of Physics "Enrico Fermi", Course LXXXIII, eds W. Brandt and A. Duasquier (North-Holland, Amsterdam, 1983) p. 510.

[10] L.J. Seijbel, *An instrument for positron micro-analysis*, PhD. Dissertation, Delft University of Technology, Delft, 1995.

[11] L.V. Jørgensen, *Positron moderation and re-emission experiments*, PhD. Dissertation, Delft University of Technology, Delft, 1998.

[12] K.G. Lynn, J.R. MacDonald, R.A. Boie, L.C. Feldman, J.D. Gabbe, M.F. Robbins, E. Bonderup and J. Golovchenko, *Phys. Rev. Lett.* **38** (1977) 241.

[13] K.G. Lynn, J.E. Dickman, W.L. Brown, M.F. Robbins and E. Bonderup, *Phys. Rev. B* **20** (1979) 3566.

[14] S. Matsui, *J. Phys. Soc. Jpn.* **61** (1992) 187.

[15] J.R. MacDonald, K.G. Lynn, R.A. Boie and M.F. Robbins, *Nuc. Inst. Meth.* **133** (1978) 189.

Chapter 4

Data Analysis of 2D-ACAR Spectra

4.1 Introduction

The data analysis can be divided into two stages. In the first stage the data is corrected for finite detector aperture and centred. In the second stage the data is analysed by calculating the anisotropy. A correction of the elliptical resolution function is also applied since this facilitates the interpretation of the data.

The data handling in the first stage consists of :

- Correcting for the momentum sampling function
- Calculating the position of $\mathbf{p} = 0$ and centring of the distribution
- Symmetrising the distribution (only applied in certain cases)

Coincidence events are collected in groups of 30,000 s. At least ten of these measurements are collected. Each measurement is corrected for the momentum sampling function and centred. When all measurements are corrected they are summed. The final distribution has a total number of counts of $\sim 6 \cdot 10^7$ counts obtained during 300,000 s.

4.2 Momentum sampling function

A correction of the measured data for the finite geometry of the detectors and to a lesser extent for the non-uniformity of the efficiency across the detector area is necessary [1, 2]. The finite geometry of the detectors affects the probability of event detection. Events with a low angular deviation have a higher probability of being detected than those with a high angular

deviation. The measured distribution $n_m(p_x, p_y)$ (with p_x and p_y defined by equations 3.1 and 3.2, respectively) is related to the true distribution $n_t(p_x, p_y)$ by

$$n_m(p_x, p_y) = c(p_x, p_y) n_t(p_x, p_y), \tag{4.1}$$

where

$$c(p_x, p_y) = \int\int dp'_x dp'_y \varepsilon_1(p_x - p'_x, p_y - p'_y)\varepsilon_2(p'_x, p'_y) \tag{4.2}$$

is the convolution of the single detector efficiencies, ε_i. The function $c(p_x, p_y)$ represents the probability of detecting both gammas for a specific (p_x, p_y) and is called the momentum sampling function. The probability for a specific (p_x, p_y) is the product of efficiency of detector 1 times the efficiency of detector 2 at positions that result in the observed (p_x, p_y) combination. For identical detectors with uniform efficiencies, equal sample-detector distances and with the centres of the detectors in line with the sample the probability of detecting events with $\mathbf{p} = 0$ is higher than for any other momentum. The probability for detecting events with the maximum measurable angle (momentum) is very small since these events only occur when both gammas hit the edges of the two detectors at exactly opposite positions. For circular detectors $c(p_x, p_y)$ is a circular cone with the maximum detectable momentum as radius. For detectors with a square shaped detector area the distribution would be a pyramid with a square base. Because of the peaked shape, the momentum sampling function is also known as tent function.

The term single detector efficiency is somewhat misleading since it is not the efficiency of the detector but the efficiency of the detector *for annihilation gamma-rays emitted from the sample* that is important. This includes the efficiency of the detector but also includes obstructions in the vacuum chamber. The most prominent obstruction is the sample itself. Gamma-rays emitted downwards travel through the sample and a larger fraction of them will be scattered than of the gamma-rays emitted upwards. This difference is reflected in a measurement with a single detector as can be seen in figure 4.1. More annihilation gamma-rays are detected in the upper part of the detector than in the lower part. To calculate the momentum sampling function it is necessary to measure the single distributions of both detectors (without coincidence condition) under identical conditions as the 2D-ACAR measurement. Since each sample is different this should be repeated for each new sample and for each new measurement condition.

The correction for the momentum sampling function is performed by dividing the measured distribution by the calculated momentum sampling function at each position. This correction should be performed before any other data correction including the centring is carried out. If both detectors are placed at identical sample-detector distances the momentum sampling function has a peaked shape. Successively measured distributions exhibit small shifts in the position of the centre. Any misalignment between the momentum sampling function and the measured distribution will introduce artificial structure in the corrected distribution; especially when a

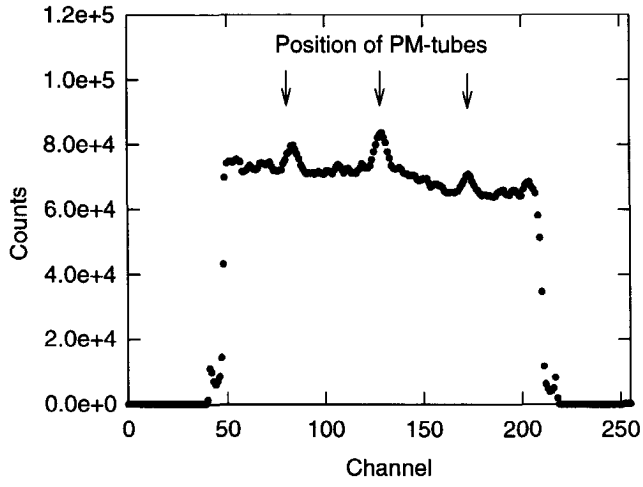

Figure 4.1: *Cross-section of a single detector measurement at p_x=0 without applying a coincidence condition. The low channels denote gamma-rays detected in the upper part of the detector, high channels denote gamma-rays detected in the lower part of the detector. In the lower part a fraction of the gamma-rays is scattered in the sample. The three arrows mark the positions of photomultiplier tubes.*

distribution with sharp features at the centre of the distribution is measured this can give erroneous results. To avoid these problems the sample-detector distances are chosen different for the two detectors. The distance between the sample and detector 2 is 1.18 times the distance between the sample and detector 1. Instead of a sharp peak the momentum sampling function will then have a flat top, and as a result a slightly different position of the momentum sampling function with respect to the ACAR distribution will not influence the central region of the distribution. Figure 4.2 shows an example of the momentum sampling function of our setup. Figure 4.3 is a cross-section through this distribution at $p_y = 0$. The flat part of the momentum sampling function is limited to the range between -10 and 10×10^{-3} m_0c but this also the range where the main features of a 2D-ACAR distribution occur. The single detector measurements which are used to calculate the momentum sampling function can be obtained before or after the 2D-ACAR measurement. Figure 4.4 shows the result of a division of the momentum sampling functions obtained before and after the measurement. In the ideal case both distributions are identical and the division only results in 1's. The figure shows that in the central region only very small variations ($< 0.1\%$) exist. The medium grey area covers roughly the area between -50 and 50×10^{-3} m_0c for both directions. This area is comparable with the area which is ac-

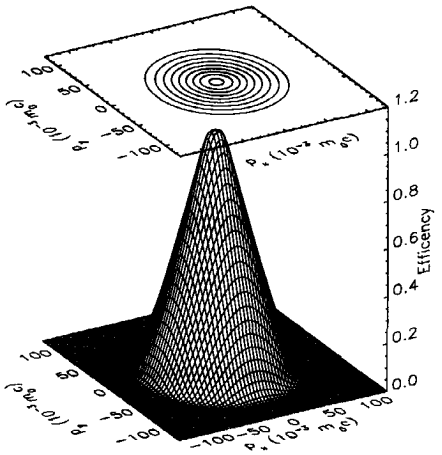

Figure 4.2: *Example of the momentum sampling function of the 2D-ACAR setup.*

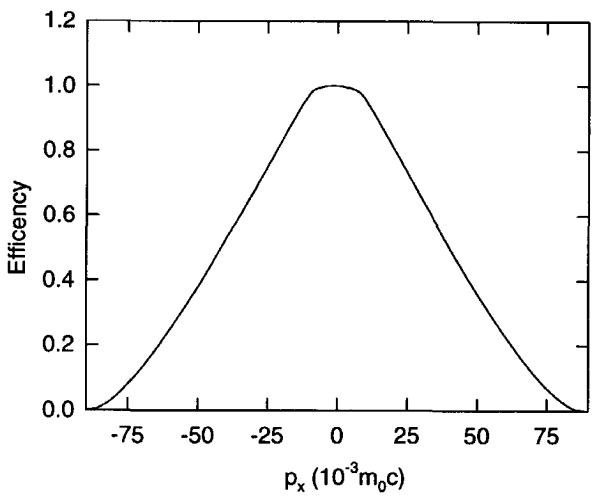

Figure 4.3: *Cross-section at $p_y = 0$ through the momentum sampling function.*

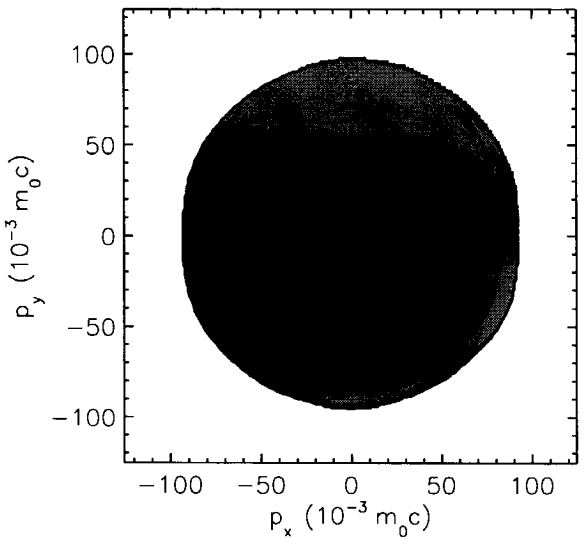

Figure 4.4: *Division of the momentum sampling functions as calculated before and after the 2D-ACAR measurement. The contour lines are shown between 0.996 and 1.004 with a spacing of 0.001 . The light grey area denotes parts with values below 0.999, the medium grey area values between 0.999 and 1.001 and the dark grey area values above 1.001 .*

quired during a 2D-ACAR measurement.

In figure 4.1 one can clearly see the position of the photomultiplier tubes. Along the cross-section only five photomultiplier tubes are present, two of which are positioned outside the active detector area. In other directions, with up to nine photomultiplier tubes, the position of the photomultiplier tubes is less obvious. Two matching photomultiplier patterns in the single detector efficiencies of detector 1 and 2 would create features in the momentum sampling function. This is not desirable since one wishes to obtain a smoothly varying, feature less function. The use of different detector-sample distances for the detectors also reduces the effects of matching photomultiplier patterns. To avoid these effects even further one detector is rotated over 90 °with respect to the other detector. This creates two different photomultiplier patterns and results in a smoothly varying momentum sampling function such as the curve in figure 4.2.

4.3 Determination of the centre

The centre of the distribution, (x_c, y_c), is calculated by taking advantage of the symmetry between the top and the bottom half of the true distribution. The distribution is rotated over 180°and χ^2 is calculated according to

$$\chi^2 = \sum_k \sum_l \frac{(n'(k,l) - n(k,l))^2}{n(k,l)}, \tag{4.3}$$

where $n(k,l)$ and $n'(k,l)$ denote the distribution before and after rotation. Only the part of the distribution with $p \leq 10.5$ mrad is used. The centre of the distribution is estimated by minimising χ^2. The distribution is moved so that the centre is at the point (128,128) of the two-dimensional distribution of 256 × 256 channels. To this end a quadratic interpolation scheme is used.

The centring is necessary to correct for small shifts in the central peak position and to obtain a well defined centre for further analysis. Figure 4.5a shows the centre position as a function of time during one series of measurements (total duration two weeks). The changes in the x and y direction are correlated. This is most likely caused by temperature effects on the electronics. The shift in the position of the centre is less than 0.2 channel (0.1 mrad) between two measurements. Figure 4.5b shows that the count rate is very stable, apart from the decrease caused by the nuclear decay of the source.

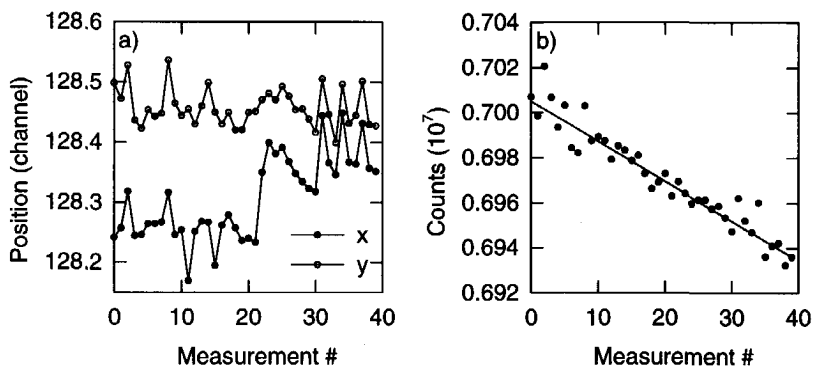

Figure 4.5: *Series of 40 measurements of 30,000 s each. For each measurement the centre of the distribution is calculated. Figure a) shows the centre position in channels for each measurement (the lines are guides to the eye). Figure b) shows the total number of counts. The line represents an exponential decay with* $T_{1/2}$ = 2.6 y *(the nuclear decay time of* ^{22}Na*).*

4.4 Symmetry

The point-symmetry of a single crystal is reflected in its momentum distribution. The symmetry in the distribution can be used to increase statistics by folding the distribution with respect to the symmetry axes. The symmetry axes in the momentum distribution can be found by copying the angular distribution, rotating this distribution between $0° \leq \theta \leq 180°$ and calculated the χ^2 difference with the original distribution [3]. The positions of the minima in the χ^2 versus angle curve indicate the symmetry axes. Since our resolution function is different in the p_x and p_y direction we cannot apply this method directly to our data sets. The difference in resolution will severely distort the χ^2 versus angle curve.

4.5 Background

The background in the 2D-ACAR measurements is mainly caused by accidental coincidences. The background during a measurement is 2 c/s (both experimental and calculated with equation 3.19). When the source is stored in the container a coincident count rate of only 0.002 c/s is measured. The distribution of accidental coincidences is measured by delaying one of the coincidence signals, resulting in uncorrelated events (due to accidental coincidences) being processed. The background resembles the momentum sampling function. The count rate is very low and the spectrum in figure 4.6 took one week to acquire. To reduce the statistical fluctuations the data was smoothed with a gaussian (FWHM = $2 \times 10^{-3}\ m_0c$). After division by the momentum sampling function the background is a flat distribution as the solid curve in figure 4.6 shows. As was explained in section 4.2 it is important to use the single detector efficiency for annihilation gamma-rays emitted from the sample. If one would measure this distribution in coincidence mode (using a second detector close to the sample to measure the other annihilation photon) the measured distribution becomes slightly different. The correction of the background with the momentum sampling function based on these measurements with a coincidence condition yields the dotted curve in figure 4.6. The data is overcorrected on the top side and the corrected background is not a flat distribution anymore. Although the effect is small, especially in the central region of the distribution, the overcorrection has consequences when one compares the bottom and top part of a spectrum.

4.6 Anisotropy

The 2D-ACAR distribution will in general show an angle-dependent structure, but this structure is often not easily visible in the 2D-ACAR distribution. To bring out this anisotropy an isotropic function is subtracted from the distribution. The isotropic function is defined as the set of minimum (or average) values in $n(p_x, p_y)$ found on circles $p_x^2 + p_y^2 = p^2$ followed by an

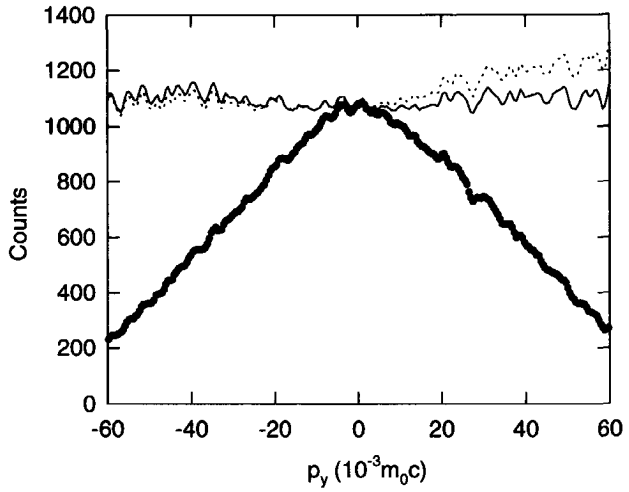

Figure 4.6: *Cross-sections of a background measurement at $p_x = 0$ for $-12 < p_y < 12 \times 10^{-3}$ m_0c after smoothing by a gaussian with a FWHM of 2×10^{-3} m_0c (black dots). The solid line is the background after correction for the momentum sampling function obtained by using the single detector efficiencies. The dotted line is the background after correction for the momentum sampling function obtained with single detector efficiencies acquired while applying a coincidence condition.*

optional radial smoothing. The anisotropy will always be positive if the minimum value is used. Shoulders in the original distribution will become peaks in the anisotropy plot.

In many quartz samples positronium (Ps) is formed. The momentum distribution of positronium is very narrow and thus the centre of the ACAR distribution will be dominated by this positronium peak. Besides a sharp peak at $\mathbf{p} = 0$ also satellite peaks appear at momenta corresponding to projections of the reciprocal lattice vectors of quartz [4]. Positronium in quartz can be described by a delocalised Bloch state. The small peaks are the "Umklapp peaks" and appear at momenta corresponding to the projected reciprocal lattice. The measured distribution and the anisotropy plot of quartz are shown in figure 4.7. The contour lines are plotted at intervals of $1/10^{th}$ of the maximum value except for the first contour line. The first interval is split in four and instead of a thin solid line a thin dashed line is used. The interval between the dashed lines is therefore $1/40^{th}$ of the maximum value. Lines denoting zero are marked with a thick solid line (not present in this figure). The positronium peak has an elliptical shape due to the different resolution in the x and y direction. This non-isotropic resolution function causes the two peaks

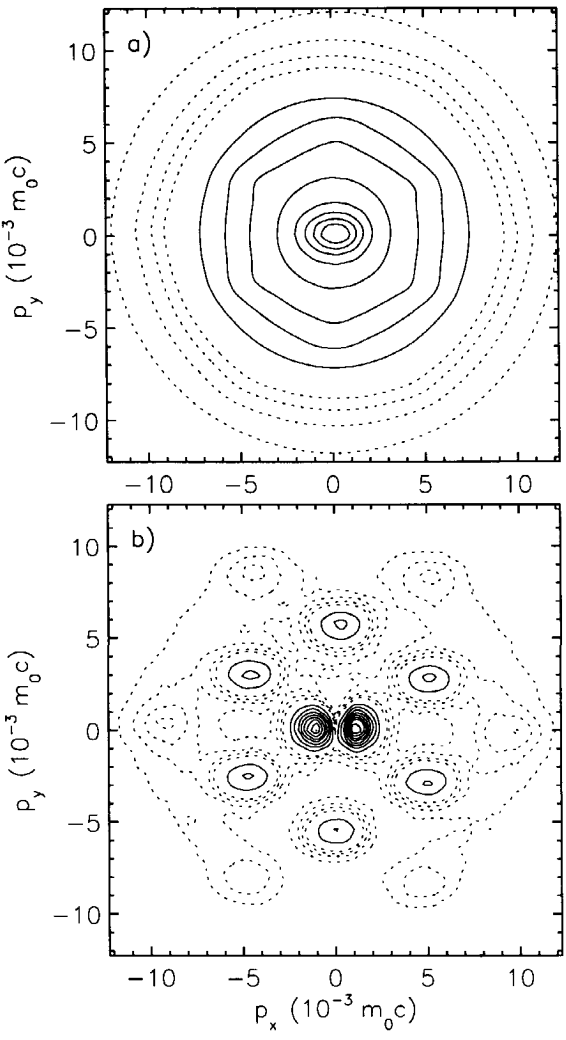

Figure 4.7: *a) Original ACAR distribution of quartz and b) the anisotropy plot showing the satellite peaks. The direction of integration was the c-axis.*

which are visible on either side of the centre of the anisotropy plot; these peaks emerge because a circular distribution is subtracted from the elliptically shaped positronium peak. Besides the central peaks two circles of six small peaks can be observed in the anisotropy plot which reflect

the hexagonal structure of quartz (the direction of integration was along the c-axis). Also the Umklapp peaks have an elliptical shape in the anisotropy plot due to the resolution function.

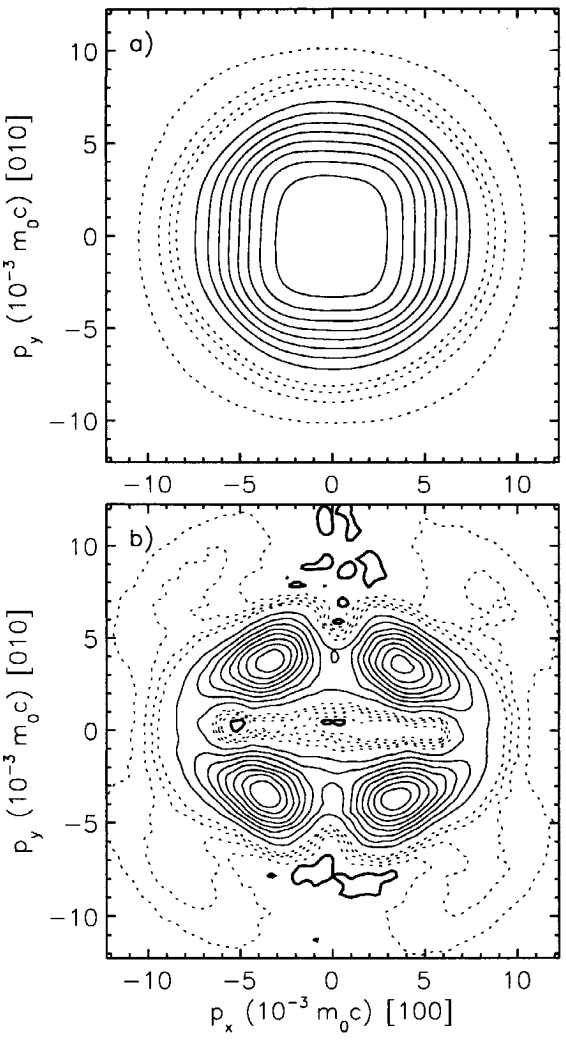

Figure 4.8: *a) ACAR measurement of silicon and b) the anisotropy plot. The direction of integration was along the [001] direction.*

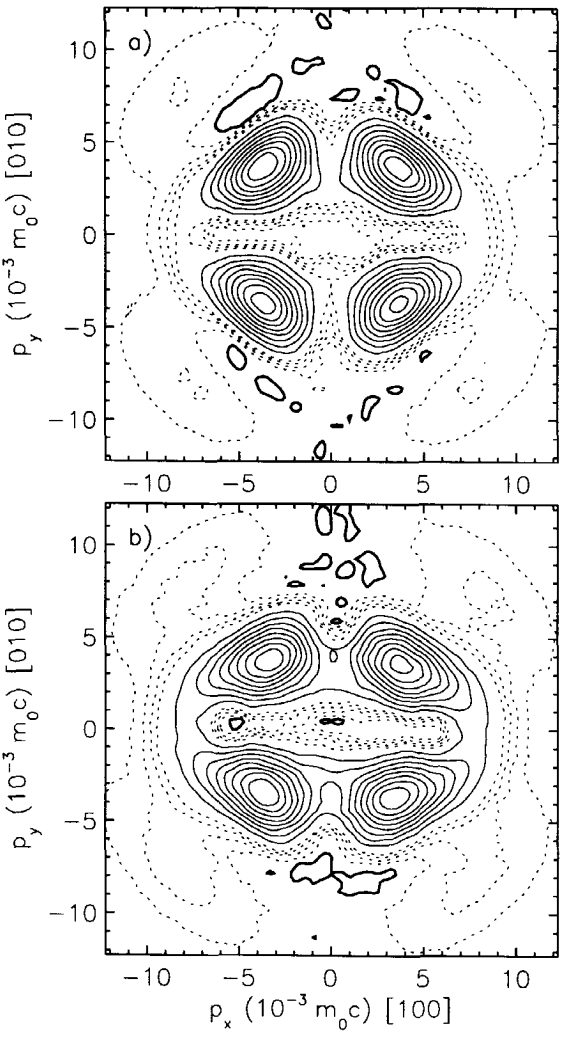

Figure 4.9: *The anisotropy plots of two silicon measurements with the direction of integration along the [001] direction. The widths of the samples were a) 5 mm and b) 10 mm, respectively.*

In figure 4.7 it can be seen that the non-circular resolution function disturbs the anisotropy plot but that the hexagonal symmetry of the distribution can still be recognised. Often however the distortion will make it hard to recognise the symmetry. In figure 4.8b the anisotropy plot of Si

is shown. Although the angular distribution is measured along the [100] and [010]- directions it is not clear that actually a four-fold symmetry is present. Furthermore, the resolution in the plane of the sample depends on the size of the positron spot on the sample. The area irradiated by the positrons has a circular shape with a radius of $\sim$ 13 mm. In our setup the sample size is usually the limiting factor for the effective beam spot. Figure 4.9 shows the anisotropy plot of Si for two samples with widths of 5 mm and 10 mm, respectively. Although the main features in the structure are identical there are also differences. Since it is not always possible to obtain samples of identical size this makes it harder to compare two measurements if no further measures are taken.

4.7 Resolution function correction

The use of the anisotropy plots is, like that of the symmetry plot, limited by the elliptical resolution function. Two corrections are possible:

- Deconvolute the distribution.
- Convolute the distribution to worsen the resolution in the direction with the best resolution.

Either method will result in a distribution with identical resolution in both directions which enables the use of symmetry plots and anisotropy plots in the analysis of the data.

Let us first look at the deconvolution. The momentum distribution $p(x,y)$ is blurred by the resolution function or point-spread function, $s(x,y)$. The measured distribution, $n(x,y)$, can be described as a simple convolution operation:

$$n(x,y) = \int\int dx'dy's(x-x',y-y')p(x',y'), \tag{4.4}$$

or, using the $\otimes$ symbol to denote the convolution,

$$n(x,y) = s(x,y) \otimes p(x,y). \tag{4.5}$$

The convolution theorem tells us that convolution is identical to multiplication of the Fourier transforms:

$$N(u,v) = S(u,v) \cdot P(u,v), \tag{4.6}$$

in which $N(u,v)$, $S(u,v)$ and $P(u,v)$ are the Fourier transforms of $n(x,y)$, $s(x,y)$ and $p(x,y)$, respectively. The inverse operation can be used to deconvolute the measured distribution to obtain the true distribution. For this operation it is necessary to know the resolution function.

Furthermore, this approach is known to introduce artificial effects like ringing [5](the appearance of spurious high-frequency structures in a restored image). These effects can be reduced by filtering the data but still their presence can not be excluded.

Another method to deconvolute the data is to use an iterative deconvolution method. Van Cittert [6] recognised that the measured data $n(x,y)$ could be considered as a first approximation $\hat{p}^{(0)}(x,y)$ of the true distribution $p(x,y)$. When convoluting this first approximation with the resolution function an approximation of the measured data $\hat{n}^{(0)}(x,y)$ is obtained. The difference between the measured data and the approximation can be used to produce a new approximation for the real distribution,

$$\hat{p}^{(1)}(x,y) = \hat{p}^{(0)}(x,y) + [n(x,y) - s(x,y) \otimes \hat{p}^{(0)}(x,y)]. \tag{4.7}$$

This process can be continued to obtain better estimates:

$$\hat{p}^{(k+1)}(x,y) = \hat{p}^{(k)}(x,y) + [n(x,y) - s(x,y) \otimes \hat{p}^{(k)}(x,y)]. \tag{4.8}$$

In this expression, $\hat{p}^{(k)}$ and $\hat{p}^{(k+1)}$ are the kth and $(k+1)$th approximation of the true distribution, respectively.

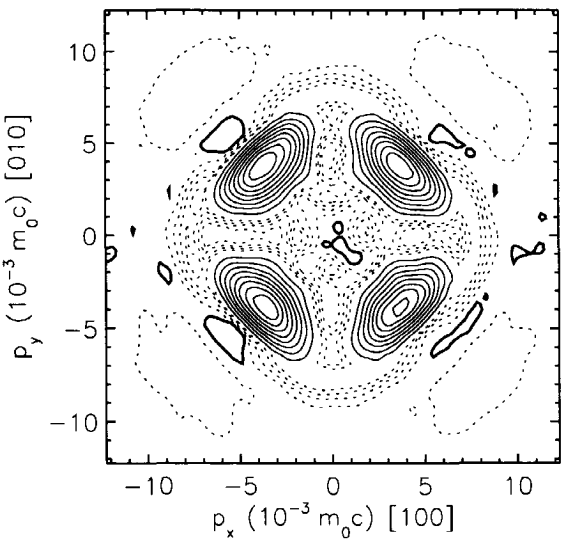

Figure 4.10: *Anisotropy plot of a deconvoluted ACAR distribution of Si using Gold's method.*

Based on this method other methods have been developed. In Gold's method [7] for example the ratio between the measured distribution $n(x,y)$ and the approximation after convolution with the resolution function is used to update the approximation. The first approximation is obtained by using the measured distribution, and the consecutive improvements are obtained with:

$$\hat{p}^{(k+1)}(x,y) = \hat{p}^{(k)}(x,y)\frac{n(x,y)}{s(x,y)\otimes\hat{p}^{(k)}(x,y)}. \tag{4.9}$$

For data without negative values, such as in counting experiments this method will not introduce unphysical negative values in the deconvoluted distribution. Figure 4.10 shows the results of the deconvolution with Gold's method. One can see that the peaks in the distribution are narrower than those of figure 4.9 and that a four-fold symmetry is present. Jansson [8] modified the van Cittert method by introducing a relaxation function, $r(\hat{p}^{(k)}(x,y))$, in equation 4.8:

$$\hat{p}^{(k+1)}(x,y) = \hat{p}^{(k)}(x,y) + r(\hat{p}^{(k)})[n(x,y) - s(x,y)\otimes\hat{p}^{(k)}(x,y)]. \tag{4.10}$$

The relaxation function is used to constrain the data to physically realisable solutions. A recent modification of the Van Cittert method is made by Coggins *et al.* [9]. They noticed that the residual image, $n(x,y) - \hat{n}^{(k)}(x,y)$ (with $\hat{n}^{(k)}(x,y) = s(x,y)\otimes\hat{p}^{(k)}(x,y)$), used to correct $\hat{p}^{(k)}(x,y)$ is the difference between blurred images, therefore it is a blurred image itself. The correction that should be used is the deconvolution of $n(x,y) - \hat{n}^{(k)}(x,y)$. Their method consists of a recursive deconvolution in which the blurred correction is first deblurred before applying it to the data. All these methods have the same drawback as the deconvolution by using the Fourier theorem: they can introduce artificial structures.

Deconvolution is successfully used in medical, technical and scientific applications. It is usually used to sharpen features in an image or to separate peaks in spectroscopic data. Dugdale *et al.* [10] applied a deconvolution method to ACAR distributions to enhance Fermi-surface related features in the ACAR distribution. We, on the other hand, are interested in all structure. To avoid the possible introduction of artificial structure we prefer the approach of worsening the resolution in one direction to obtain a circular resolution function. By using this method no artificial structure is introduced.

A circular resolution function is obtained by convoluting with a gaussian. The resolution in the x-direction is worse than that in the y-direction. The necessary width of the gaussian depends on the difference in resolution between the x- and the y-direction. This difference is determined by the spot size and the size of the sample. Figures 4.11 and 4.12 show anisotropy plots of quartz after convoluting the y-direction with progressively wider gaussians of the form $exp(-p_y^2/2\sigma_y^2)/\sqrt{2\pi}\sigma_y$. The anisotropy plot of the original distribution is shown in figure 4.7b. On either side of the centre there is a peak. The distribution as measured contained an elliptical peak at the centre with the long axis in the x-direction. When the data is convoluted with a gaussian which is too broad, the y-direction becomes worse than the x-direction (see figure 4.12b).

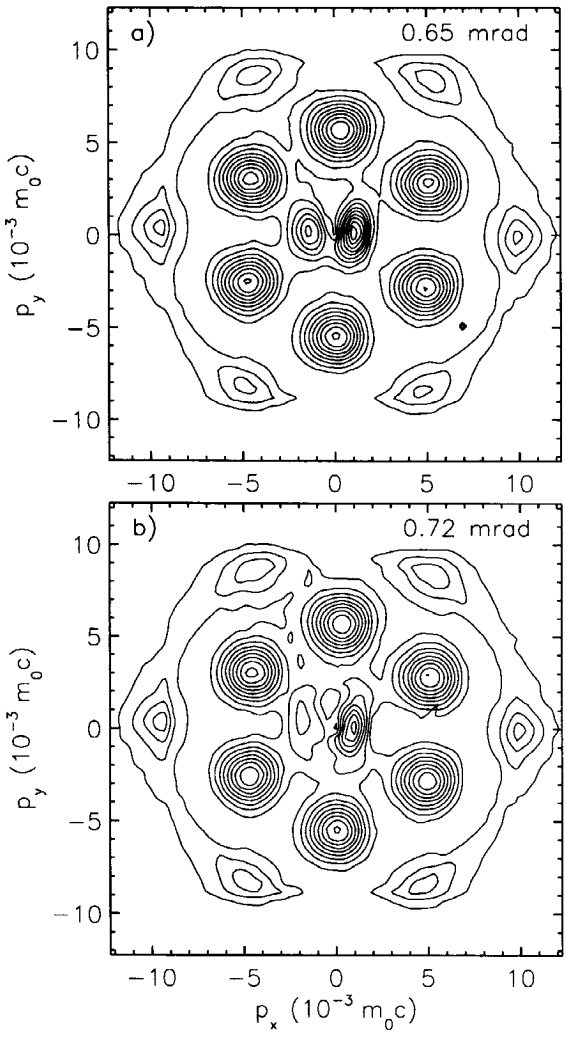

Figure 4.11: *Anisotropy plots of quartz after convoluting the measured distribution: a)* σ_y = *0.65 mrad and, b)* σ_y = *0.72 mrad (see also figure 4.12).*

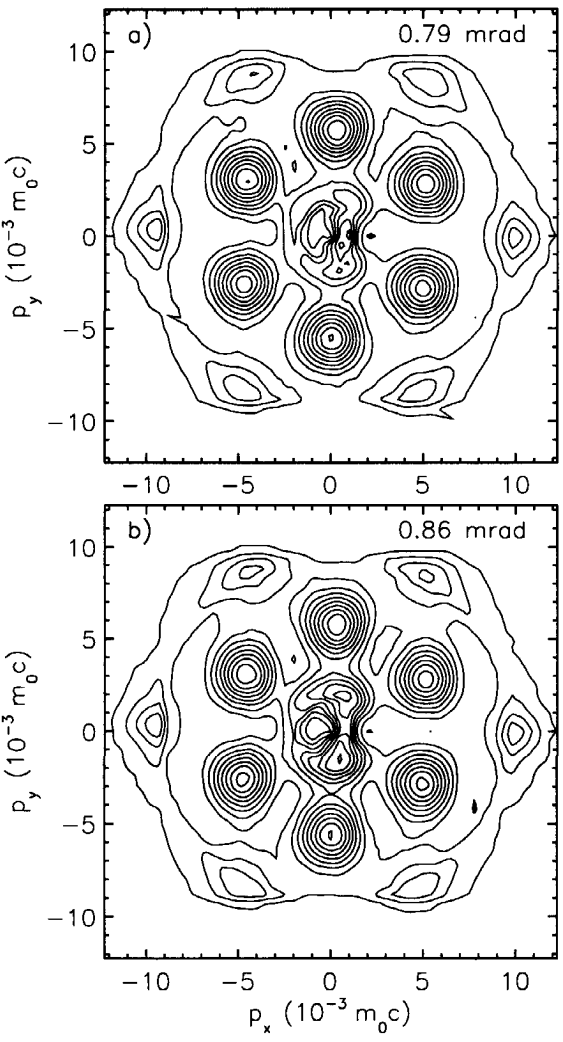

Figure 4.12: *Anisotropy plots of quartz after convoluting the measured distribution: a)* σ_y = *0.79 mrad and b)* σ_y = *0.86 mrad (see also figure 4.11).*

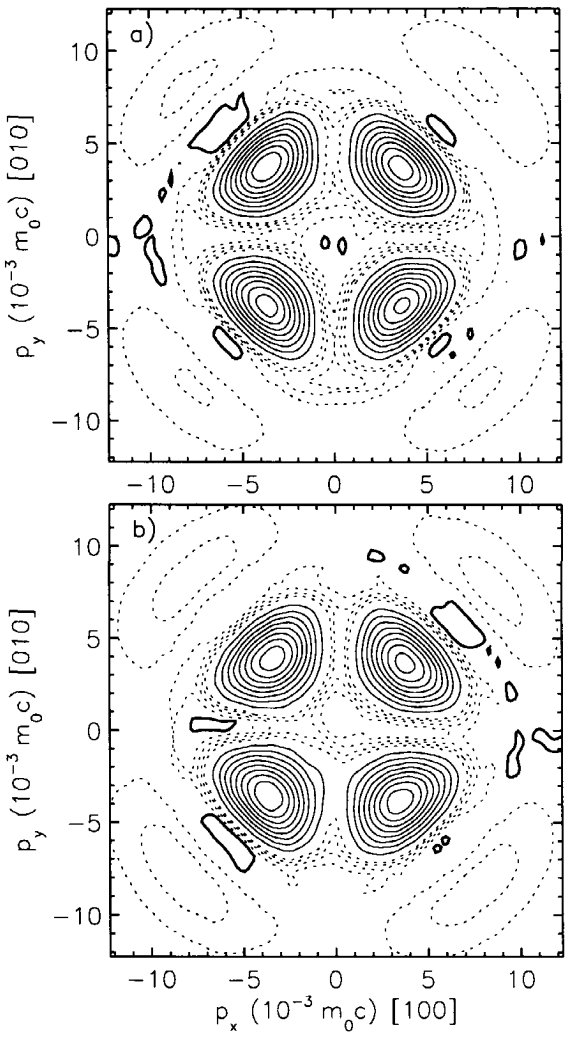

Figure 4.13: *Anisotropy plots of Si after convoluting the measured distribution: a) Sample of width 5mm convoluted with a gaussian with* σ_y = *0.67 mrad and b) Sample of width 10 mm convoluted with a gaussian with* σ_y = *0.86 mrad.*

The central peak has again an elliptical shape but now with the long axis in the y-direction. In the anisotropy plot this results in two peaks above and below the centre of the distribution. In figure 4.12a the distribution is convoluted with a gaussian with $\sigma_y = 0.79$ mrad, which results in circular satellite peaks with almost no remains of the central peak. This is therefore the amount of extra convolution which is needed to make the resolution in the x- and y-directions equal. The remaining features are caused by small differences in the centring of the distribution.

The same approach applied to the Si measurements of figure 4.9 reveals the four-fold symmetry. The resolution in the x-direction is better for the narrow sample than for the wide one. To obtain a circular resolution function the distribution is convoluted with a gaussian width $\sigma_y = 0.67$ mrad (fig. 4.13a) while for the wide sample $\sigma_y = 0.86$ mrad was used (fig. 4.13b). Thus, before in this thesis ACAR spectra are compared, they are convoluted with a gaussian to obtain an effective resolution function with a circular shape.

References

[1] S. Berko, in *Positron Spectroscopy of Solids* , Proc. of the International School of Physics "Enrico Fermi", Course LXXXIII, eds. W. Brandt and A. Dupasquier (North-Holland, Amsterdam, 1983) p. 105.

[2] R.N. West, J. Mayers and P.A. Walters, *J. Phys. E* **14** (1981) 478.

[3] L.C. Smedskjaer and D.G. Legnini, *Nuc. Inst. Meth. A* **292** (1990) 487.

[4] W. Brandt, G. Coussot and R. Paulin, *Phys. Rev. Lett.* **23** (1969) 522.

[5] R.J. Hanisch, R.L. White and R.L. Gilliand, in *Deconvolution of Images and Spectra*, ed. P.A. Jansson (Academic Press, San Diego, 1997) p. 333.

[6] P.H. Van Cittert, *Z. Phys.* **69** (1931) 298.

[7] R. Gold, *An Iterative Unfolding Method for Response Matrices*, AEC Research and Development Report ANL-6984, Argonne National Laboratory, (Argonne, 1964).

[8] P.A. Jansson, *J. Opt. Soc. Am.* **60** (1970) 184.

[9] J.M. Coggins, L.K. Fullton and B.W. Carney, *Iterative/Recursive Deconvolution with Application to HST Data*, in *The Restoration of HST Images and Spectra II*, eds. R.J. Hanisch and R.L. White, (Space Telescope Science Institute, 1994) p. 24.

[10] S.B. Dugdale, M.A. Alam, H.M. Fretwell, M. Biasini and D.A. Wilson, *Mater. Sci. Forum* **175-178** (1995) 895.

Chapter 5

Metals

5.1 Introduction

In the previous chapters two new setups were described. These setups provide additional information compared to more common techniques such as single-detector Doppler broadening and lifetime measurements. The two-detector Doppler broadening setup allows us to measure accurately the high-momentum part of the Doppler distribution. This high-momentum part stems mainly from annihilations with core electrons and provides information about the atoms around the annihilation site. The two-dimensional angular correlation of annihilation radiation technique provides a two-dimensional distribution instead of the one-dimensional spectrum obtained using DBAR.

Starting with this chapter both techniques are applied to obtain information about materials. Materials without defects and materials with vacancies were investigated. In this chapter the results of measurements of several metals are collected with the following objectives:

- to compare the measurements with calculations
- to compare the results of the two-detector Doppler broadening setup with those of the 2D-ACAR setup
- to show that the new setups indeed provide additional information.

Al and Cu were thoroughly investigated with Doppler broadening and ACAR measurements. Be, Ni, Mo and W on the other hand were only measured with the Doppler broadening technique and the results are primarily used to investigate the high-momentum region. This provides us with a data set to compare with the results of the AS calculations.

5.2 Aluminium

5.2.1 Introduction

Aluminium has been extensively investigated with various positron annihilation techniques. Lifetime [1, 2], ACAR [3–6] and Doppler broadening measurements [7] have been performed. Because of this amount of available experimental data and the fact that Al is a simple metal several calculations have been performed [3, 7–9]. The existing literature makes it a well suited material for testing our equipment and computer codes.

5.2.2 Experimental

A well annealed Al(110) single crystal was used. The crystallographic orientation was determined with the aid of reflection Laue diffraction measurements. The positron lifetime was determined with one of the positron lifetime setups at the Delft Interfaculty Reactor Institute. The time resolution of the fast-fast coincidence system was 240 ps (FWHM) and the data was analysed with the aid of PATFIT [10]. The lifetime measurement showed a single lifetime component of 164 ± 2 ps. This is in good agreement with previously reported experimental values of 163-166 ps [1, 2, 11]. Single and two-detector Doppler broadening measurements were performed with the aid of the VEP beam at Delft, whereas the 2D-ACAR measurements were performed using unmoderated positrons.

5.2.3 Results for defect-free aluminium

Figure 5.1 shows the angular distribution obtained with the 2D-ACAR setup. The central part is almost isotropic but small differences can be observed between the <100> and the <110> directions. These differences are caused by the so-called higher momentum components (HMC) of the conduction electrons. The HMC are caused by the fact that the annihilation of an electron with wavevector $\mathbf{k}$ not only gives rise to photon-pair momenta $\mathbf{p} = \hbar\,\mathbf{k}$ but also to pairs $\mathbf{p} = \hbar\,\mathbf{k} + \hbar\,\mathbf{G}_i$; were $\mathbf{G}_i$ is an reciprocal lattice vector. This second process is called Umklapp-process. The effect is that the band electrons not only contribute at $|\mathbf{p}| < |\hbar k_F|$, with k_F the Fermi-momentum, but also at higher momenta. The intensity of these HMC generally decreases for larger momenta. As a simple three-dimensional model for the contribution of the conduction electrons to the 2D-ACAR distribution in Al, one can imagine a set of Fermi spheres in momentum space with radii equal to the Fermi momentum and each displaced by a reciprocal lattice factor (Al can be described as a nearly free electron gas). Figure 5.2 shows this simple model with a central sphere and spheres displaced along a <111> or a <200> vector. The 2D-ACAR distribution consists of the projections of the spheres in figure 5.2 superimposed on a broad contribution stemming from the core electrons. For the spheres close to the central sphere the

contribution to the 2D-ACAR distribution becomes smaller as the displacement increases. The main contribution stems from the central sphere at $p = 0$. The contribution along the <110> direction stems from the projections of two <111> spheres. The contribution of one <111> sphere has 1.0 % of intensity of the central sphere. This is about three times larger than one single <200> sphere which has 0.3 % of the intensity of the central sphere [3]. The HMC's along the <110> stemming from the two <111> spheres have six times the intensity of the contribution of the <200> sphere projected along the <100> direction. This difference in intensity of the HMC's explains the the observed differences in the 2D-ACAR distribution between the <100> and <110> directions.

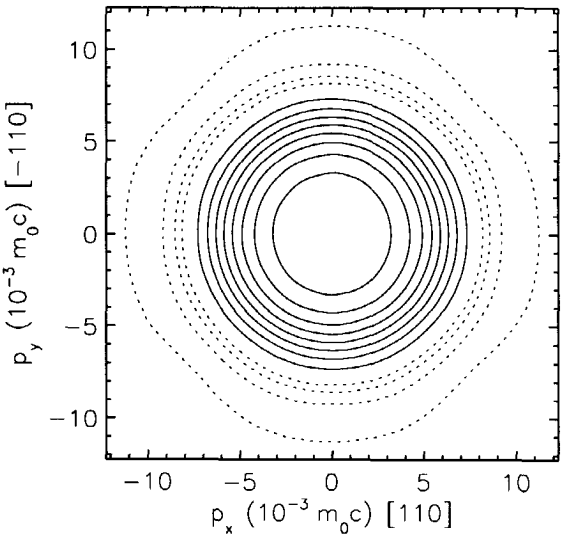

Figure 5.1: *Two-dimensional angular correlation distribution for defect-free Al*

By integrating the 2D-ACAR distribution in one direction a 1D-ACAR curve is obtained. Integration of the distribution of figure 5.1 in the x or y direction results in two 1D-ACAR curves, both along a <110> direction. Other directions can be obtained by integrating the 2D-ACAR distribution in an appropriate direction or by measuring the sample with a different orientation. Thus, a second 2D-ACAR distribution was measured in which the x direction corresponds to a <100> direction and the y direction to a <110> direction. The integration of this distribution along the x or y direction results in 1D-ACAR curves along a <110> and <100> direction, respectively. The 1D-ACAR curves for the <100> and <110> directions are almost identical as we can see in figure 5.3a. The integration obscures the effects caused by the crystallographic

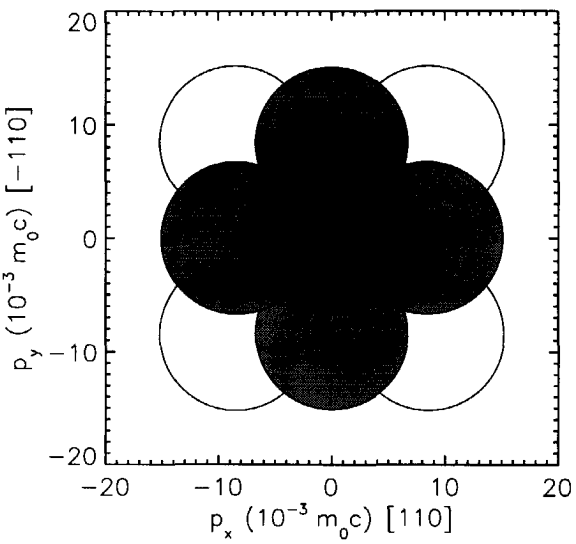

Figure 5.2: *Model for the central contribution (dark grey) of the conduction electrons and the first two sets of HMC contributions of the <111> spheres (light grey) and the <200> spheres (based on Mader et al. [3]).*

structure but small differences still exist, as is shown in figure 5.3b. The symbols represent the results of the second ACAR measurement. The filled squares show a different behaviour from the open diamonds. To check if this is a real effect and not some kind of artifact one of the 1D-ACAR curves of the first measurement is shown as a solid line in this figure. The line and the open diamonds coincide nearly perfectly which is proof that the difference between the <100> and the <110> directions is indeed a real effect.

In a Doppler broadening experiment a twice integrated momentum distribution is measured. This curve can be compared with a 1D-ACAR curve if one keeps in mind that generally the resolution of an ACAR measurement is (much) better than that of a DBAR setup. Also, in a DBAR setup, the direction of integration is less well determined than in an ACAR setup. The integration direction in an ACAR setup is almost identical to the line that connects the centre of the detectors owing to the large sample-detector distance of more than 5 m. On the other hand, in a DBAR setup the detectors are placed very close to the sample and each detector spans a large solid angle. This introduces an uncertainty in the integration direction and obscures the direction dependency of the momentum distribution.

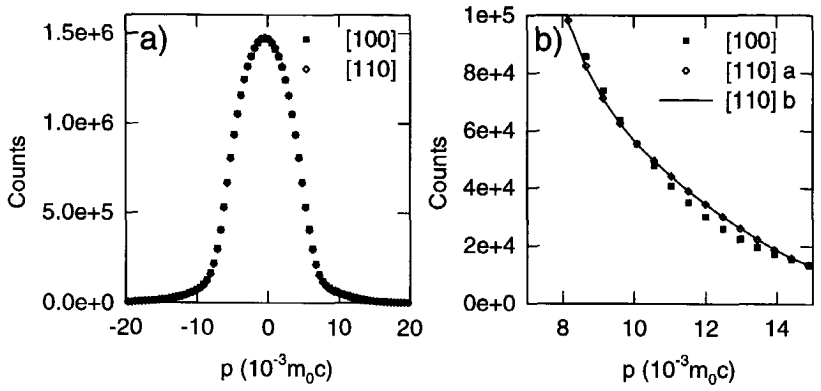

Figure 5.3: *1D-ACAR curves along the <100> and <110> direction obtained from projections of the 2D-ACAR distribution. a) Complete distribution, and b) enlargement of the region between 7 and* 15×10^{-3} m_0c *where the solid line represents the result of the projection of a second 2D-ACAR distribution (see text).*

Doppler broadening curves were measured with the two-detector setup for three different orientations of the Al single crystal. The <110> surface was orientated perpendicular to the beam but the crystallographic axis along the line connecting the centres of the detectors was different for each measurement. Figure 5.4 shows the curves for the [110], [114] and [100] directions. In figures 5.4a and b the data points lie practically on top of one another. This is not surprising since also the 1D-ACAR curves for the <100> and <110> direction were almost identical.

It is interesting to compare the results of the ACAR setup with those of the two-detector DBAR setup. Figure 5.5a shows that the low momentum distributions of the ACAR and the two-detector DBAR are in reasonable agreement. The small differences are probably caused by the different resolution of the systems and by the effect of the uncertainty in the integration direction in the DBAR setup. Although the resolution of the DBAR setup is worse than that of an ACAR setup and the integration direction is less well determined, the two-detector DBAR setup has one big advantage: the ability to measure the high-momentum part of the distribution almost background-free. Figure 5.5b shows the results for a two-detector DBAR and a once integrated 2D-ACAR measurement on a logarithmic scale after correction for the momentum sampling function. In the ACAR curve a large background is present compared to the low background of a two-detector DBAR measurement. The background as measured by the ACAR system resembles that of the momentum sampling function. After correction for the momentum sampling function the background is an almost flat contribution to the ACAR spectrum and thus the spectrum can be corrected by subtracting a background contribution determined at large angles. The

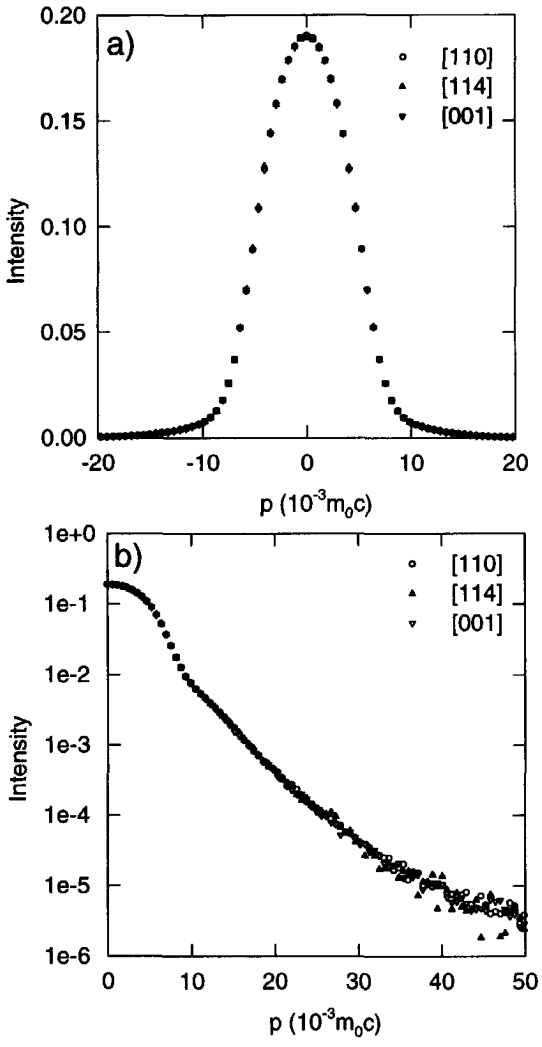

Figure 5.4: *Two-detector Doppler broadening measurements along the* [114], [110] *and* [100] *directions. Plotted on a) linear scale and b) semi-logarithmic scale.*

filled triangles in figure 5.5b are the result of this background correction. They lie still above the result of the two-detector measurement in the high-momentum region. Apparently, the simple background subtraction method is not good enough. Part of the problem is the shape of the

momentum sampling function which resembles a truncated pyramid with a circular base. The correction in the central part of the distribution is small whereas the correction is large at large angles where the count rate is low. For example, at 40×10^{-3} m_0c the background component is $\sim 0.2\%$ of the peak height while the true signal is only 0.01 % of the peak height. Another reason for the difference can be the shape of the ACAR resolution function. In section 3.2.4 it was shown that the resolution function of the ACAR setup contains a very broad component (although with a small intensity). At high momenta resolution differences have usually only a small effect on the distribution since the distribution there does not contain sharp features (on the scale of the FWHM of the resolution function). A gaussian shaped resolution function with a FWHM of 4×10^{-3} m_0c results only in a small broadening of the distribution at for example 40×10^{-3} m_0c. A broad component on the other hand has an influence on the entire distribution. The necessity to subtract a significant background component, together with the long tail of the resolution function, make the integrated 2D-ACAR curves in general not suited to extract information about the contribution of the core electrons. A cross-section through the centre of the 2D-ACAR distribution however can be helpful to obtain information about the core electrons: the peak to background ratio is better than that of a 1D-ACAR curve and one obtains information that is only once integrated. Such a cross-section could therefore give useful information for improving the calculations.

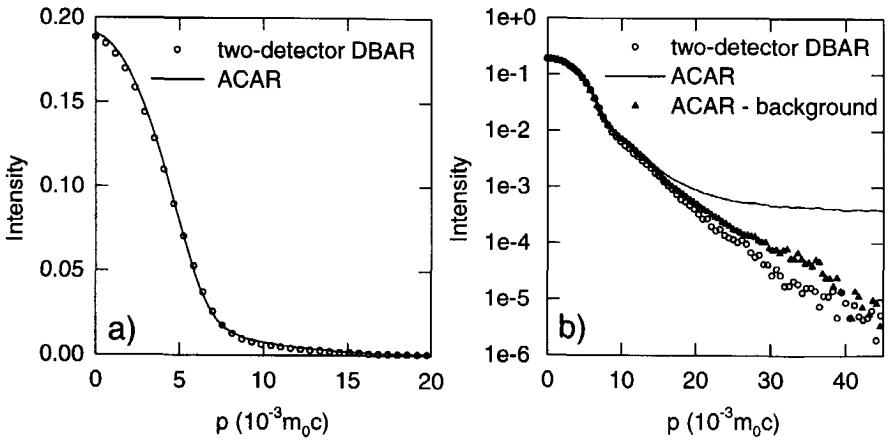

Figure 5.5: *a) comparison of the once integrated 2D-ACAR distribution and the two-detector Doppler broadening distribution b) the same on a logarithmic scale, together with the 1D-ACAR data after correction for the background.*

5.2.4 Calculation of Doppler broadening curves for defect-free aluminium

One of the purposes of measuring Al was to use the results to validate different computer codes for calculating the momentum distribution. The calculation of positron-electron observables is complicated by the fact that the correlation effects between the positron and the electrons, which result in an enhancement of the independent particle annihilation rate, are not known exactly. An approximation is therefore necessary. In momentum density calculations the Local Density Approximation (LDA) is often used. In this approximation the enhancement is assumed to be a function of the electron and positron local densities. In a vacancy-free crystal in which the positron is in a delocalised state, the enhancement factor is assumed to depend only on the local electron density, characterised by the quantity $r_s = (3/4\pi n_-)^{1/3}$. In section 2.2 three LDA parametrisations were described: the interpolation of Boroński and Nieminen [12]

$$\gamma(r_s) = 1 + 1.23r_s + 0.8295r_s^{3/2} - 1.26r_s^2 + 0.3286r_s^{5/2} + \frac{1}{6}r_s^3, \tag{5.1}$$

the new interpolation of Puska *et al.* [13]

$$\gamma(r_s) = 1 + 1.23r_s + 0.9889r_s^{3/2} - 1.482r_s^2 + 0.3956r_s^{5/2} + \frac{1}{6}r_s^3, \tag{5.2}$$

and the LDA as proposed by Barbiellini *et al.* [14]

$$\gamma(r_s) = 1 + 1.23r_s - 0.0742r_s^2 + \frac{1}{6}r_s^3. \tag{5.3}$$

To obtain the GGA enhancement of Barbiellini *et al.* this last function is modified according to:

$$\gamma_{GGA} = 1 + (\gamma_{LDA} - 1)e^{-\alpha\varepsilon}. \tag{5.4}$$

Here α is an adjustable parameter and ε is a measure of the gradient of the electron density given by:

$$\varepsilon = |\nabla n(\mathbf{r})|^2/(n(\mathbf{r})q_{TF})^2, \tag{5.5}$$

where $\nabla n(\mathbf{r})$ is the gradient of the charge density and q_{TF} is the Thomas Fermi screening length (in atomic units $q_{TF} = \sqrt{(4/\pi)p_F}$). Barbiellini *et al.* [14] found that $\alpha = 0.22$ gives lifetimes which for a large number of materials are in good agreement with experimental results. In our GGA calculations we have used the same value for α.

Mijnarends *et al.* [16] have performed KKR calculations. The momentum distribution calculated was twice integrated to obtain a one-dimensional distribution which was convoluted with the experimental resolution of 0.90 keV. The results were compared with the experimental data as obtained in a two-detector Doppler broadening experiment. Figure 5.6 shows that the LDA of Puska *et al.* and the state dependent GGA result in a Doppler broadening curve that is in good

Table 5.1: Annihilation rates in Al as calculated by the KKR and AS methods employing the LDA enhancement of Boroński and Nieminen [12] (LDA-BN), the LDA enhancement of Puska *et al.* [13] (LDA-P) or the GGA enhancement of Barbiellini *et al.* [14] (GGA).

	KKR		AS		
	LDA-P	GGA	LDA-BN	LDA-P	GGA
1s (ns^{-1})	0.0015	0.0010	0.0014	0.0014	0.0010
2s (ns^{-1})	0.1410	0.0813	0.1451	0.1452	0.0839
2p (ns^{-1})	0.4550	0.2859	0.4680	0.4670	0.2921
band (ns^{-1})	5.4271	6.1736	5.3448	5.2670	5.8880
total (ns^{-1})	6.0246	6.5418	5.9630	5.8806	6.2649
lifetime (ps)	166	153	168	170	160

agreement with the experimental data. The second observable which can be compared with theory is the lifetime. The experimental lifetime was found to be 164 ± 2, in good agreement with literature [1, 2, 11]. Table 5.1 shows the calculated partial annihilation rates as calculated with the KKR and the AS methods for different enhancement functions. When using the same enhancement function the KKR and the AS method result in very similar partial annihilation rates for the core electrons. The largest differences between the KKR and the AS calculations exist between the annihilation rates for the band electrons. Since the band electrons dominate the total annihilation rate this results in differences in the calculated lifetimes of 7 ps for the GGA and of 10 ps for the LDA of Puska *et al.* When we compare the experimental lifetime of 164 ps with the KKR calculations we observe that the lifetime of 153 ps for the GGA enhancement is too short, while the lifetime of 166 ps for the LDA of Puska *et al.* is in good agreement with the experimental result. This leads to the conclusion that for Al the best results are obtained with the LDA enhancement function of Puska *et al.*

The two-dimensional histogram of a two-detector Doppler broadening measurement contains more information than just an improved Doppler broadening curve. The histogram also contains information related to the resolution of the setup and the binding energy of the annihilating electron-positron pair in a solid. By taking a cross section along the line $E_1 = E_2$ one obtains a peak which is a good representation of the resolution function of the setup. In reality this peak consists of a sum of peaks, each displaced by the binding energy of the annihilating positron-electron pair and broadened by the resolution function. The events along the line $E_1 = E_2$ consist mainly of positrons annihilating with valence electrons. The binding energy of the band electrons is small (several eV) compared to the resolution of the setup ($\sim$ 1 keV) and the peak therefore represents a good approximation of the resolution of the setup. Instead of taking a cross-section at $p = 0$ one can also take a cross-section parallel to the line $E_1 = E_2$

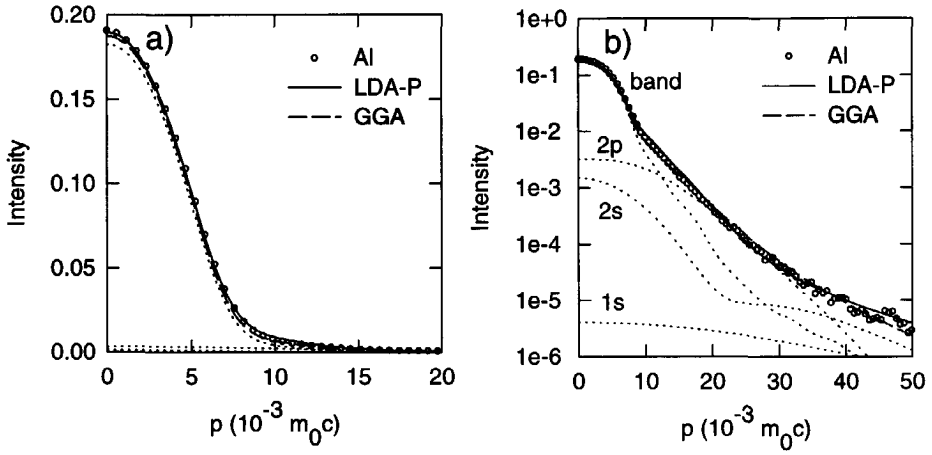

Figure 5.6: *Doppler broadening curves in Al calculated with the KKR methodology employing the LDA of Puska et al. (solid line) and the GGA of Barbiellini et al.(dashed line) and the experimental data obtained with the two-detector DBAR setup on a linear (a) and logarithmic scale (b). The curves are normalised to unit area.*

at higher momenta. This cross-section is no longer a gaussian shaped peak since at higher momenta a substantial fraction of the positrons annihilate with core electrons. Figure 5.7 shows a cross-section through the two-detector Doppler broadening distribution at $\Delta E = 9$ keV. One observes a shift in the peak position and a deviation from the gaussian shape. The form of this distribution contributes, besides the lifetime and the Doppler broadening profile, a third aspect which can be used to compare the experimental results with the calculations. KKR calculations provide the relative contributions for each electron shell. Each contribution is displaced by $\sim E_b/2$ and after convolution with the resolution function and summation of all contributions one obtains the profile shown as the solid curve in figure 5.7. The dashed curves in this figure represent the contributions of each electron shell. The largest contributions stem from the 2p and 2s electrons while there are smaller contributions from the 1s and the band electrons. The 2p and 2s peaks are marginally shifted with respect to the centre of the peak, the binding energies for these shells being 57 and 94 eV, respectively. The binding energy of the 1s electrons is 1488 eV which results in the contribution centred at -744 eV. A small background component was added. The background was determined in the experimental data between 2 and 3 keV.

The contribution of the 1s electrons strongly influences the shape of the curve. The curve has no longer a gaussian shape but contains a tail on the negative energy side. This deviation from

a gaussian is also observable in the experimental data. Figure 5.8 shows the effect of the annihilation rate of the 1s electrons on the profile. Besides the experimental data points and the profile of figure 5.7 also the profile for a three times smaller and a three times larger annihilation rate for the 1s shell are shown. The experimental data agree best with the profile containing the originally calculated 1s contribution. Although a smaller contribution of the 1s shell is possible, it is clear that a considerably larger fraction can be excluded since the profile with a three times larger 1s contribution does not agree with the experimental data.

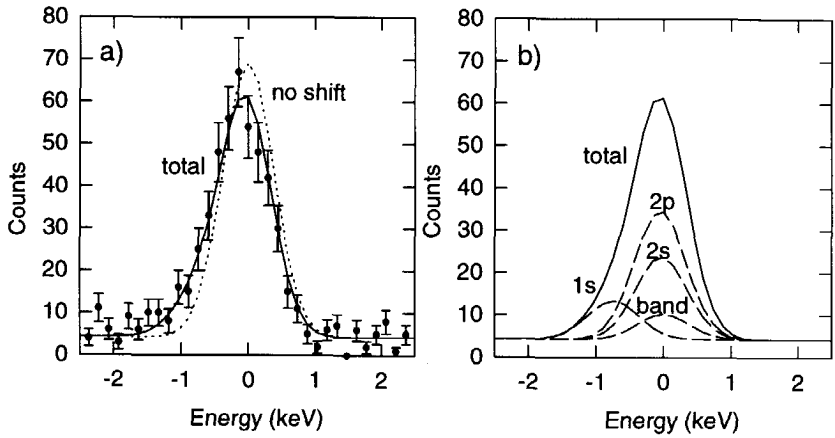

Figure 5.7: *a) Cross-section through the two-dimensional DBAR distribution at an energy shift of 9 keV. The symbols represent the experimental data while the solid line is the profile calculated using the KKR method employing the LDA of Puska et al. b) The contribution of each electron shell (on top of the background contribution). The energy scale along the x axis is determined from* $(E_{total}$ *- 1022 keV)/2.*

The shape and the shift in the cross-section profiles are interesting since they provide a method to check the calculated relative intensities for the core electrons. This information cannot be obtained from the total annihilation rate since that is dominated by the contribution of the band electrons. It is also very hard to extract this information from the high-momentum part of the Doppler broadening curve since in that curve the partial contributions are directly added together. In the cross-section profile on the other hand the contributions are added together with the binding energy as an offset which enables us to distinguish the contributions between tightly bound core electrons ($E_b > 1$ keV) and the other electrons.

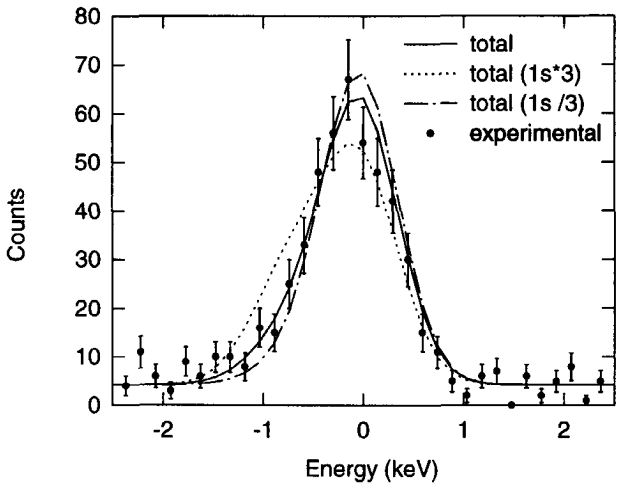

Figure 5.8: *Calculated profiles for an energy shift of 9 keV. The contribution of the 1s electrons is decreased (chain curve) and increased (dotted curve) by a factor of three. The symbols represent the experimental data.*

5.2.5 Thermal vacancies in Al.

Positron annihilation techniques are well suited for the investigation of open-volume defects in materials. Owing to the low melting point of Al (932 K) it is experimentally easy to create thermal vacancies in Al. By varying the temperature between 300 K and 870 K the effects of low and high concentrations of vacancies can be investigated. Our results are limited to slow positron beam experiments since this setup has a heating facility.

In figure 5.9 two-detector Doppler broadening curves obtained at 300 K, 430 K and 670 K are compared. For all three measurements the sample was mounted with the line connecting the centres of the two detectors along a <100> direction of the Al sample. In the sample measured at 670 K thermal vacancies are present. A positron can trap at the vacancy and the overlap between the positron and electron wavefunctions is reduced. The result is a smaller annihilation rate (longer lifetime). The overlap between the positron and the core electron wavefunctions is reduced more than the overlap with the valence electrons, and so the Doppler broadening curve becomes sharper. In DBAR experiments two parameters are commonly used to reflect those changes: the S parameter, which represents the central part of the distribution, and the W parameter, which is determined by the wings of the 511 keV photo peak. Figure 5.9 shows the integration intervals for the determination of the S and W parameters. The interval for W

determines what kind of information the W parameter can provide. Our W interval is between 9 and $24 \times 10^{-3}\ m_0c$ and provides information about the contribution of the core electrons. A W window situated close to the centre of the 511 keV annihilation peak, on the other hand, is still dominated by the contribution of the band electrons and does not provide additional information compared to the S parameter. In our setup the W parameter **does** provide additional information and the combination of S and W is used to characterise annihilation sites [17].

The Al sample was heated from 300 K to 870 K and at selected temperatures the single-detector Doppler broadening curve was measured to determine the S and W parameters [18]. To avoid the influence of the surface of the Al sample a positron implantation energy of 22 keV was used. The effects of the annealing become very clear in the S-W plot of figure 5.10. Between 300 K and 450 K the S and W parameters slightly increase. The increase of S as a function of temperature is well known and is related to the thermal expansion of the lattice. No thermal vacancies are formed yet. Starting at 450 K the W parameter decreases rapidly as a function of temperature. At this temperature thermal vacancies are created. Between 450 and 740 K the points are more or less on a straight line indicating that two characteristic annihilation sites play a role: bulk Al and one type of defect, i.e., monovacancies. Above 740 K the curve begins to deviate which indicates the presence of another type of defect, i.e., divacancies.

In the previous section it was shown that the KKR calculations employing the state-dependent GGA enhancement are in good agreement with the experimental Doppler profile of defect-free aluminium. It is possible to perform this type of calculation also for aluminium with a vacancy but a greater computational effort is necessary. Furthermore, important factors for these calculations such as the relaxation of the atoms around the vacancy are not exactly known. Instead of using the KKR methodology we can use the AS method for the high-momentum region. The AS method has one important advantage over more sophisticated methods like the KKR methodology: it is computationally less demanding. As we could see in section 2.3 the results for the AS and KKR methods are comparable for the core electrons and the first method was applied to calculate the high-momentum part of a DBAR distribution for monovacancies in Al. In this calculation a supercell with 107 Al atoms and 1 vacancy was used. No relaxation was taken into account. The calculated distribution was convoluted with a gaussian with a FWHM of 0.90 keV to include the resolution function of the setup. The GGA enhancement was used. The calculated lifetime of a monovacancy is 228 ps. This is too short compared to the experimental lifetime of 240-250 ps [19,20]. Figure 5.11 shows the experimental results of the DBAR measurements at 300 K and 670 K. The curves are calculations performed with the AS method. The dotted curve represents the result of the calculation for a monovacancy. When this curve is compared with the experimental data points measured at 670 K (filled triangles) it is clear that those data points lie above the calculated curve in the region between 20 to $50 \times 10^{-3}\ m_0c$ which is the region were the AS method should provide reliable results. Apparently, the effect

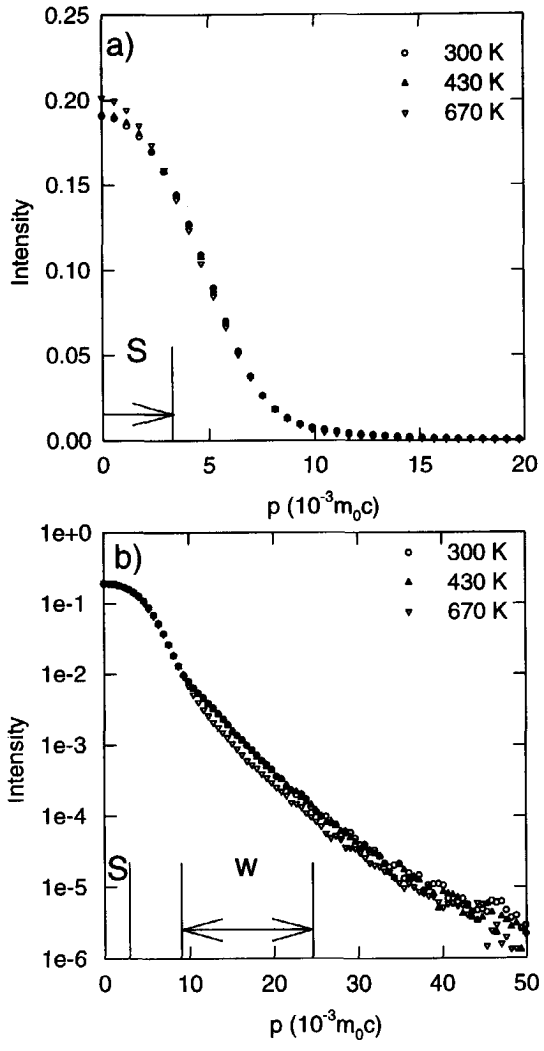

Figure 5.9: *Two-detector DBAR distribution for aluminium measured at 300 K and 430 K (both defect-free), and at 670 K (monovacancies). S and W mark the intervals used in the determination of the S and W parameters.*

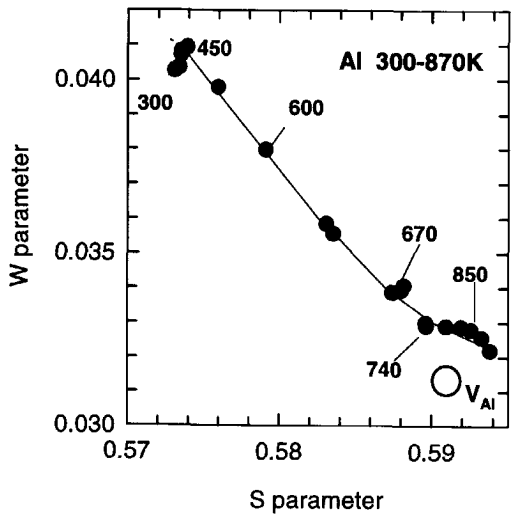

Figure 5.10: *S-W plot for Al with the annealing temperature as a running parameter. The solid line is to guide the eye. The circle marks the S-W point for a monovacancy.*

of the vacancies is overestimated in the calculation. This overestimation is most likely caused by the very high vacancy concentration in the calculation (1%) while for the experiment a value of 10^{-5} at 670 K is more realistic [5]. At 670 K only a fraction of the positrons annihilates at or near the vacancy. To determine this fraction the S-W point for annihilations in monovacancies should be known. The S and W parameters are linear combinations of characteristic contributions. When annihilations occur only at two types of annihilation sites (but with different intensities) the data points in an S-W plot will lie on a straight line. This situation is the case between 450 and 650 K. Above this temperature other defects begin to play a role and a deviation from the straight line occurs. This deviation makes it harder to determine the exact point of the characteristic contribution for monovacancies. Lifetime measurements are in this case more suited to determine the trapped fractions as a function of temperature. Fluss *et al.* [5] performed these measurements and determined that at 670 K 75 % of the annihilations occur in mono- and/or divacancies. A new DBAR distribution can be constructed, for comparison with the experimental results measured at 670 K, consisting of 0.75 times the calculation for Al with a monovacancy and 0.25 times the calculation for defect-free Al. This curve is drawn in figure 5.11 as a solid line. The agreement with the data points (filled triangles) for the 670 K measurement is very good between 20 and $50 \times 10^{-3}\ m_0c$. This shows that with the AS method it is possible to calculate the DBAR distribution for defect-free materials as well as for materials with defects.

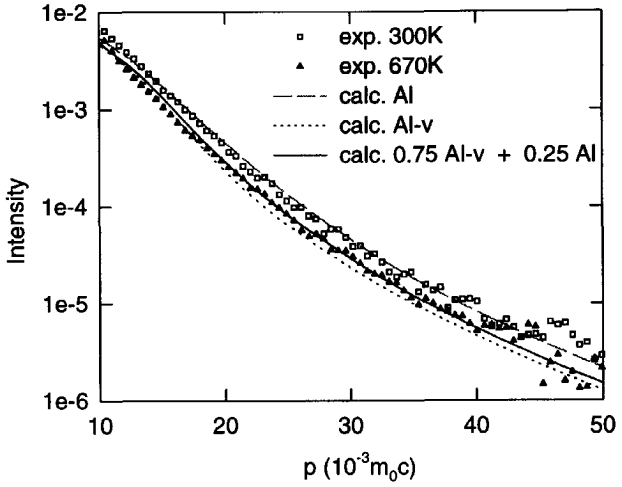

Figure 5.11: *Two-detector DBAR distribution for aluminium measured at 300 K (defect-free) and at 670 K (containing monovacancies). The lines represent AS calculations for defect-free Al (dashed line), a monovacancy (dotted line) and a linear combination of 0.75 times the distribution of a monovacancy and 0.25 times that of defect-free Al.*

5.3 Copper

5.3.1 Introduction

A second well investigated material is Cu. Also for Cu a vast amount of literature exists [8, 21–23]. For our two-detector Doppler broadening and 2D-ACAR experiments a well annealed Cu (100) single crystal was used. The crystallographic orientation was determined with the aid of reflection Laue diffraction measurements.

5.3.2 Results

Figure 5.12 shows the angular distribution obtained with the 2D-ACAR setup. Again differences can be observed between the <100> and <110> direction. These differences become even more noticeable after the subtraction of an isotropic component as described in section 4.6. The result of this subtraction is the anisotropy plot in figure 5.13a. The contour lines are plotted

at intervals of $1/10^{th}$ of the maximum value except for the first contour line. The first interval is split in four and instead of a thin solid line a thin dashed line is used. The interval between the dashed lines is therefore $1/40^{th}$ of the maximum value. The line denoting zero is marked with a thick solid line. The anisotropies are mostly caused by the HMC. The simple model of figure 5.1b is more complicated in Cu since the Fermi spheres are connected along the <111> direction (the so-called "necks"). It is possible to calculate this anisotropy with computer codes which properly include the crystal symmetry of the material, such as the KKR method. Mijnarends calculated the two-dimensional ACAR distribution for Cu using the KKR method. After convolution with the resolution function of the experimental setup, the isotropic component was determined and subtracted from the calculated distribution. The result is the anisotropy plot of figure 5.13b. This figure shows the same features as the experimental anisotropy plot in figure 5.13a, such as a peak at $[4 \times 10^{-3}\ m_0c, 4 \times 10^{-3}\ m_0c]$ and a smaller peak at $[0, 15 \times 10^{-3}\ m_0c]$.

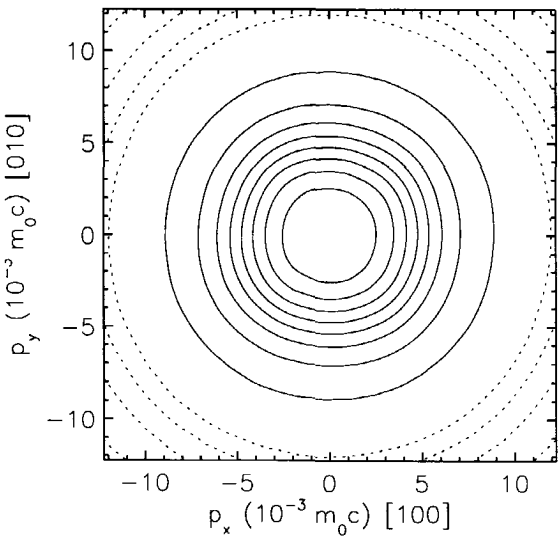

Figure 5.12: *Angular correlation distribution for defect-free Cu.*

Besides ACAR measurements, also two-detector DBAR measurements were performed. Figure 5.14 shows the experimental data points together with the results of the KKR calculations employing the LDA of Puska *et al.* and the GGA. If we look at the high-momentum part we can see that there is a large deviation between the experimental data points and the GGA result. In the region between 20 and $40 \times 10^{-3}\ m_0c$ the GGA results are significantly higher than the

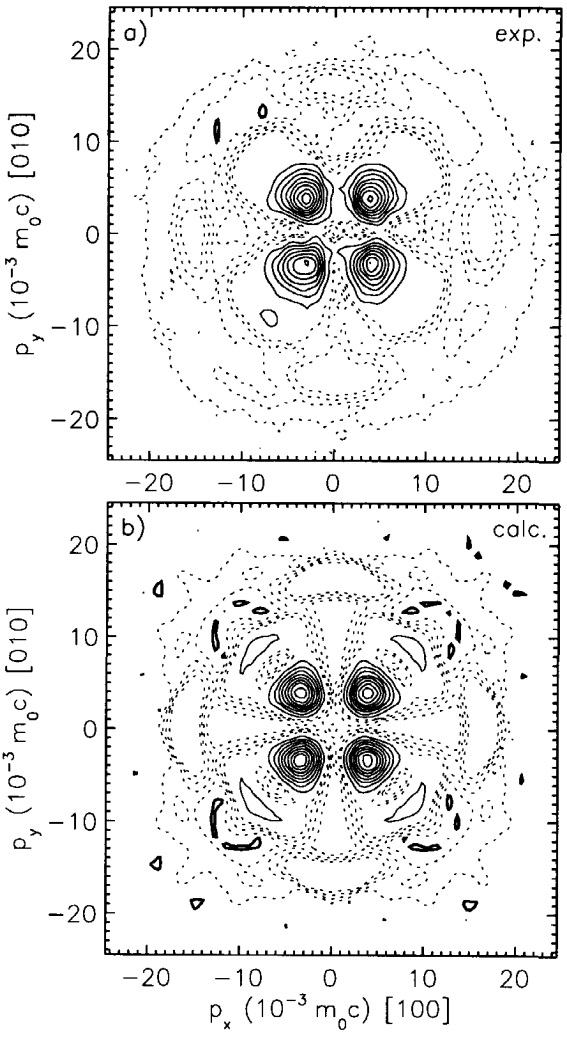

Figure 5.13: *a) Measured anisotropy plot for Cu b) Calculated anisotropy plot.*

experimental data points. The results for the LDA calculation are close to the experimental data points between 20 and 50×10^{-3} m_0c. The first impression is that a reasonable agreement between the KKR calculation employing the LDA of Puska *et al.* and the experimental results exists, but if we look at the central part of the distribution we see important differences and it

becomes clear that the GGA nor the LDA enhancement result in a calculated curve that matches the experimental distribution. Both calculated distributions are not peaked enough compared to the experimental data. Apparently, the approximation used for the enhancement is not correct for Cu. This is somewhat puzzling since Barbiellini *et al.* [15] obtained a good agreement with the LMTO method employing the GGA enhancement. Their experimental data for the high-momentum region and their AS calculations [24] are in agreement with ours. The central part depends strongly on the resolution of the setup and could not be compared. In the KKR calculations the same electron state dependent enhancement was used as was used by Barbiellini *et al.* and at this moment we are not able to explain the differences in the results.

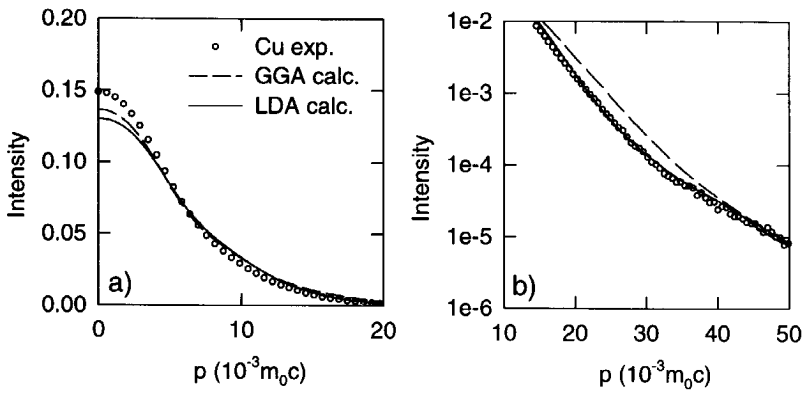

Figure 5.14: *Two-detector measurement for Cu and calculated DBAR curves plotted on a) linear scale and b) semi-logarithmic scale.*

The high-momentum part of the DBAR distribution can also be calculated with the AS method. The lifetimes calculated are in reasonable agreement with the experimental values of 110-120 ps [11,25] only the 130 ps as calculated by the AS method employing the GGA is definitely too long. The core annihilation rates calculated by the AS method are systematically higher than those calculated by the KKR method but the differences in the calculated lifetimes are, as in Al, caused by the smaller annihilation rate for the band electrons. The agreement between the KKR and the AS method for the high momentum region of the DBAR distributions is good for both types of enhancement as can be seen in figure 5.15. Both methods provide a distribution which is too broad compared to the experimental data between 10 and 40×10^{-3} m_0c when the GGA enhancement is used. Alatalo *et al.* [24] already observed that in AS calculations employing the GGA enhancement the addition of the contribution of the $3d$ electrons to the calculated distribution resulted in curves which are too wide in the high-momentum region compared to the

Table 5.2: Annihilation rates in Cu as calculated by the KKR and AS methods employing the LDA enhancement of Puska *et al.* [13] (LDA-P) or the GGA enhancement of Barbiellini *et al.* [14] (GGA).

	KKR		AS	
	LDA-P	GGA	LDA-P	GGA
1s (ns^{-1})	0.0000	0.0000	0.0000	0.0000
2s (ns^{-1})	0.0025	0.0018	0.0027	0.0020
2p (ns^{-1})	0.0055	0.0040	0.0061	0.0045
3s (ns^{-1})	0.2307	0.1469	0.2475	0.1567
3p (ns^{-1})	0.9116	0.5886	0.9791	0.6271
band (ns^{-1})	8.1766	7.5988	7.8488	6.8555
total (ns^{-1})	9.3283	8.3403	9.0844	7.6462
lifetime (ps)	107	120	110	130

experimental data. According to these authors this is possibly caused by the *3d* electrons being treated as core electrons in the AS calculation. Since the 3*d* electrons in fact form a band, one can expect discrepancies between the experimental results and the calculations. However, that explanation does not hold anymore since the KKR calculations in which the 3*d* electrons are calculated as band electrons show the same behaviour. This directs the suspicion as to the cause of the discrepancy toward the GGA enhancement. Although the use of the LDA enhancement does improve the calculated distribution in the high-momentum region the overall fit is not very good compared to the quality of the fit that was obtained for Al. Apparently an enhancement that only depends on the local electron density (LDA) or on the local electron density and its gradient (GGA) can not perfectly describe the positron-electron correlation effects in Cu. Other types of enhancement can improve this. Kahana [26] for example proposed an enhancement which depends on the momentum, while Mijnarends and Singru [27] showed that an excellent agreement for Cu could be obtained for the central part of 1D-ACAR distributions (0 to $20 \times 10^{-3}\ m_0 c$) by using a modified Kahana-type enhancement.

Although the Cu results show that no perfect match with the LDA or GGA is obtained, the next section will show that with the GGA enhancement it is at least possible to calculate the correct trends in the high-momentum part of the DBAR curves in a range of other metals.

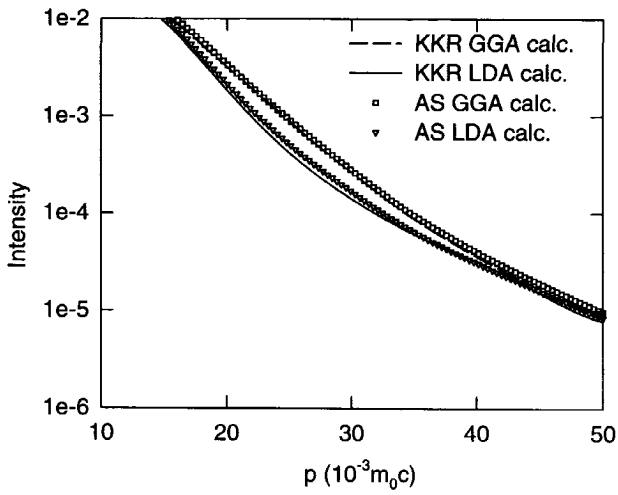

Figure 5.15: *Comparison of KKR and AS calculations employing the LDA of Puska et al. or the GGA enhancement.*

5.4 Other metals

The previous sections show the results of measurements on defect-free, carefully orientated, single crystals of Al and Cu. Asoka-Kumar *et al.* [28] and Myler and Simpson [29] already showed that the high momentum part contains information that can be used to identify the atoms surrounding the annihilation site. In section 2.3 it was shown that the results for the high-momentum part of the momentum distribution for the AS and KKR methods are comparable. Alatalo *et al.* [24] and Asoka-Kumar *et al.* [28] have demonstrated that the AS method employing the GGA enhancement provides a useful tool in predicting the shape of the high-momentum part of the DBAR distribution. To underline the usefulness of the AS method and the "element" specificity of the high-momentum part of the DBAR distribution, examples are shown for beryllium, nickel, molybdenum and tungsten. No KKR calculations were performed for these metals and the experimental results are only compared to the AS calculations.

All samples except Mo showed a long diffusion length indicating that the samples were defect-free. The Mo sample was annealed at 1900 K but the melting point of Mo is very high (2890 K). The short diffusion length can indicate the presence of defects or the existence of a thin surface layer. This last explanation is more likely since the diffusion length became even shorter after the annealing at 1900 K. None of the samples was aligned according to a specific crystallographic axis; this has only a small effect on the high-momentum part of the distribution. The

calculations were performed using the AS model for $90 \times 90 \times 90$ node points and employing the GGA enhancement. The experimental data were collected during a period of two years using different setups, each with its own resolution. The calculated distributions are convoluted with the appropriate resolution function to include this effect. Table 5.3 shows the calculated lifetimes. They are in reasonable agreement with the experimental results. The lifetime of Be quoted by MacKenzie is based on old measurements of Weisberg and Berko [30]. The sensitivity of positrons to defects was at that moment not well recognised and the sample could have contained defects. This can explain the large difference between both experimental lifetimes. Figure 5.16a shows the high momentum part of the experimental data. When we compare these data with the calculated curves in figure 5.16b one can see that although the agreement for separate curves is not very good the behaviour of the curves with respect to each other is in good agreement with the experiment. To compare a few curves:

- Mo and Be are well separated at $10 \times 10^{-3}\ m_0c$, come close to each other at $20 \times 10^{-3}\ m_0c$ and diverge again. The experimental points and the calculated curves both show this behaviour although the calculation overestimates the separation between the curves at high momenta;
- Ni and W are well separated at $10 \times 10^{-3}\ m_0c$, come close at $30 \times 10^{-3}\ m_0c$ and diverge again;
- W and Mo are close to each other at $12 \times 10^{-3}\ m_0c$, then begin to diverge and come together again around $50 \times 10^{-3}\ m_0c$.

This example shows that the high-momentum part of experimental data can be used to distinguish between different elements. The AS method is capable of predicting the correct trends in the shape of the curves although the absolute agreement between the experimental data and the calculated curves is not always very good. These differences are probably related to the LDA/GGA enhancement and not to the approximations (free-atomic electron wavefunctions, spherical symmetry) inherent to the AS method, since in Cu the KKR method employing the GGA enhancement did not agree with the experimental data either.

5.5 Conclusions

The results of the KKR calculations with an enhancement according to the GGA or the LDA of Puska *et al.* are in good agreement with the experimental data for Al. The shift in the annihilation energy due to the binding energy of the electron could be observed and calculated. This provides a method for estimating the fraction of positrons that annihilate with tightly bound core electrons. Besides the KKR calculations also AS calculations were performed. If the same enhancement is employed the results for the high-momentum region are nearly identical for

Table 5.3: Calculated and experimental lifetimes.

Element	Experimental (ps)		Calculated (ps)
	Ref. [25]	Ref. [11]	
Be	142	213	129
Ni	110	110	109
Mo	103	121	118
W	105	120	108

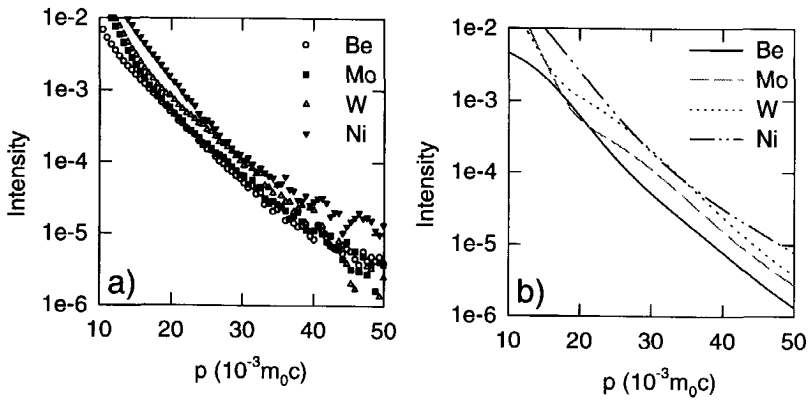

Figure 5.16: *a) experimental results for Be, Ni, Mo and W acquired with a two-detector DBAR setup, b) calculated DBAR curves with the AS method employing the GGA enhancement.*

both methods. The enhancement used has a larger influence on the high-momentum part of the DBAR distribution than the choice between the KKR and AS method. For Cu the agreement between the measured and calculated DBAR distribution is not good. Although a good match is obtained with the LDA of Puska *et al.* for the high-momentum part of the distribution, important differences exist in the central part. Apparently, neither the LDA nor the GGA enhancement provides a good approximate description of the positron-electron interaction. Nevertheless, qualitatively good results were previously obtained with the GGA enhancement for several materials [24, 28]. The usefulness of the AS method in combination with the GGA enhancement is again confirmed by the results for a selection of metals. The high-momentum part of the experimental distributions for Be, Ni, Mo and W show the same trends as the calculated distributions. Furthermore, the AS method is also suited to calculate the high-momentum part of the

DBAR distribution for materials with defects such as a monovacancy in Al. The two-detector measurements for Be, Ni, Mo and W show that the high-momentum region provides elemental specific information. This information can not be accessed with a single detector DBAR setup or an ACAR setup due to the high background.

The 2D-ACAR measurements of Al and Cu show that this setup provides additional information compared to a DBAR setup. The two-dimensional distribution shows the contribution of the HMC. Although effects of the HMC can be observed in 1D-ACAR curves it is hard to recognise them and even harder to determine their origin. The anisotropy of the 2D-ACAR distributions can be reproduced by calculations using the KKR-based methodology. The 2D-ACAR curves can be integrated to create 1D-ACAR curves which can then be compared with the DBAR results. This comparison of 1D-ACAR curves and two-detector DBAR curves showed that the central parts are almost identical. The high-momentum regions can not be compared since the background in the 1D-ACAR curve is too high.

References

[1] S. Tanigawa, K.Hinode and M. Doyama, *Phys. Stat. sol. B* **82** (1977) 369.

[2] H-E. Schaefer, R. Gugelmeier, M. Schmolz and A. Seeger *Mater. Sci. Forum* **15-18** (1987) 111.

[3] J. Mader, S. Berko, H. Krakauer and A. Bansil, *Phys. Rev. Lett.* **37** (1976) 1232.

[4] W. Triftshäuser, *Phys. Rev. B* **12** (1975) 4634.

[5] M.J. Fluss, S. Berko, B. Chakraborty, K.R. Hoffman, P. Lippel and R.W. Siegel, *J. Phys. F: Met. Phys.* **14** (1984) 2831.

[6] M.J. Fluss, S. Berko, B. Chakraborty, P. Lippel and R.W. Siegel, *J. Phys. F: Metal Phys.* **14** (1984) 2855.

[7] K.G. Lynn, J.R. MacDonald, R.A. Boie, L.C. Feldman, J.D. Gabbe, M.F. Robbins, E. Bonderup and J. Golovchenko, *Phys. Rev. Lett.* **38** (1977) 241.

[8] S. Berko and J.S. Plaskett, *Phys. Rev.* **112** (1958) 1877.

[9] B. Chakraborty, *Phys. Rev. B* **24** (1981) 5445; B. Chakraborty and R.W. Siegel, *Phys. Rev. B* **24** (1981) 7423; R.P. Gupta and R.W. Siegel, *Phys. Rev. B* **27** (1983) 4535.

[10] P. Kirkegaard, M. Eldrup, E. Morgensen and O. Pedersen, *Phys. Comm.* **23** (1981) 307.

[11] I.K. MacKenzie, in *Positron Spectroscopy of Solids* , Proc. of the International School of Physics "Enrico Fermi", Course LXXXIII, eds. W. Brandt and A. Dupasquier (North-Holland, Amsterdam, 1983) p. 196.

[12] E. Boroński and R.M. Nieminen, *Phys. Rev. B* **34** (1986) 3820.

[13] M.J. Puska, A.P. Seitsonen and R.M. Nieminen, *Phys. Rev. B* **52** (1995) 10947.

[14] B. Barbiellini, M.J. Puska, T. Kornhonen, A. Harju, T. Torsti and R.M. Nieminen, *Phys. Rev. B* **53** (1996) 16201.

[15] B. Barbiellini, M. Hakala, M.J. Puska, R.M. Nieminen and A.A. Manuel, *Phys. Rev. B* **56** 7136.

[16] P.E. Mijnarends, A.C. Kruseman, A. van Veen, H. Schut and A. Bansil, *J. Phys.: Cond. Mat.* **10** (1998) 10383.

[17] M. Clement, J.M.M. de Nijs, H. Schut, A. van Veen and P. Balk, *J. Appl. Phys* **79** (1996) 9029.

[18] A. van Veen, A.C. Kruseman, H. Schut, P.E. Mijnarends, B.J. Kooi and J.Th.M. de Hosson, *Mater. Sci. Forum* **255-257** (1997) 76.

[19] R.M.J. Cotterill, K. Petersen, G. Trumpy and J. Träff, *J. Phys. F: Metal Phys.* **2** (1972) 459.

[20] M.J. Fluss, L.C. Smedskjaer, M.K. Chason, D.G. Legnini and R.W. Siegel, *Phys. Rev. B* **17** (1978) 3444.

[21] R.N. West, *Adv. Phys.* **22** (1973) 263.

[22] R.M. Singru, *Phys. Stat. sol. A* **30** (1975) 11.

[23] S. Berko, M. Haghgooie and J.J. Mader, *Phys. Lett. A* **63** (1977) 355.

[24] M. Alatalo, B. Barbiellini, M. Hakala, H. Kauppinen, T. Korhonen, M.J. Puska, K. Saarinen, P. Hautojärvi and R.M. Nieminen, *Phys. Rev. B* **54** (1996) 2397.

[25] A. Seeger, F. Banhart and W. Bauer, in *Positron annihilation*, Proceedings of the 8th International Conference on Positron Annihilation, eds. L. Dorikens-Vanpraet, M. Dorikens and D. Segers (World Scientific, Singapore, 1987) p. 275.

[26] S. Kahana, *Phys. Rev.* **129** (1963) 1622; J.P. Carbotte and S. Kahana *ibid.* **139** (1965) A213; J.P. Carbotte, *ibid.*, **155** (1967) 197.

[27] P.E. Mijnarends and R.M. Singru, *Phys. Rev. B* **19** (1975) 6038.

[28] P. Asoka-Kumar, M. Alatalo, V.J. Ghosh, A.C. Kruseman, B. Nielsen and K.G. Lynn, *Phys. Rev. Lett.* **77** (1996) 2097.

[29] U. Myler and P.J. Simpson, *Phys. Rev. B* **56** (1997) 14303.

[30] H. Weisberg and S. Berko, *Phys. Rev.* **154** 249.

Chapter 6

Semiconductors

6.1 Electron irradiated silicon

6.1.1 Introduction

Point defects play an important role in the electrical properties of semiconducting materials, and there has been a significant effort to characterise them. The group of point defects includes: impurities, vacancies, interstitials and antisites (in compound materials). Positron annihilation techniques are very suited for the detection of vacancy-like defects in concentrations between 1 and 1000 ppm and the technique is extensively used to characterise semiconductors [1–4].

The ability to distinguish between vacancies associated with different impurities helps the analysis of the measurements and provides useful information for achieving a better understanding of the behaviour of defects in semiconductors. Our two new setups have the potential to obtain more information about defects than the more conventional lifetime and Doppler broadening techniques. The two setups provide complimentary information. The two-detector Doppler broadening setup measures the high momentum part of the distribution almost background-free, which is not possible with the ACAR system, while the 2D-ACAR experiment provides more information about the low-momentum region (two-dimensional, better resolution) than the two-detector DBAR setup.

To survey the possibilities of the new systems we investigated point defects in silicon. Silicon is widely used and is by far the most applied semiconductor in electronic devices. A way to artificially introduce point defects is by electron irradiation [5–7]. The samples in this study were irradiated with 2 MeV electrons. This energy is high enough to displace Si atoms and create Frenkel (vacancy-interstitial) pairs. Monovacancies are mobile in silicon at room temperature, and the Frenkel pairs recombine except when a vacancy is trapped near another vacancy or an impurity such as a doping atom. In the present study the effects of the doping (Sb or As) and

the defect concentration (by irradiating with three different doses of electrons) are investigated.

In semiconductors, vacancies give rise to several localised electron levels in the energy gap. The charge state of a vacancy depends on the position of the Fermi level with respect to the electron levels. The charge state of a defect has a profound effect on positron trapping and the specific trapping rate may vary orders of magnitude. Furthermore, Puska *et al.* [8] predict a strong temperature dependence of the trapping coefficient. To investigate these effects measurements were performed with the slow positron beam at low temperatures.

6.1.2 Experimental

Three different silicon samples were investigated: float zone (FZ) silicon with very low impurity concentrations and Czochralski (CZ) silicon doped with As and Sb. Secondary ion mass spectroscopy measurements performed at DIMES determined concentrations of 1.4×10^{19} As/cm^3 and 1.1×10^{18} O/cm^3 in the As doped sample, and 2×10^{18} Sb/cm^3 and 1.0×10^{18} O/cm^3 in the Sb doped sample. To check the presence of defects positron lifetime measurements were performed. The positron lifetimes in the As, Sb and undoped sample were equal to the lifetime in defect-free silicon ($\sim$ 220 ps). The samples were irradiated with 2 MeV electrons at the University of Ghent with doses of 1, 2 and 3×10^{18} e$^-$/cm^2. The sample size was $10 \times 10 \times 0.5$ mm^3 and the beamspot $\sim 17 \times 17$ mm^2. The sample was mounted on a water-cooled copper block to keep the temperature during the irradiation below 60°C.

Electrons with an energy of 2 MeV transfer a maximum energy, E_m, of 4.6×10^2 eV to a Si atom in the case of a head-on collision. The threshold energy for displacement, E_d, of a Si atom is 11-22 eV [9]. The displaced Si atom can create a small displacement cascade of other atoms since $E_m > E_d$. Only a fraction of the defects remain since most of the Frenkel pairs recombine at room temperature. Divacancies created in the collision cascades may survive since these defects are stable at room temperature. The presence of impurities leads to the survival of vacancies since these prevent the recombination of Frenkel pairs. The vacancy is trapped near an impurity and a vacancy-impurity complex is formed. In highly doped samples this is one of the defects that we may expect.

The range of 2 MeV electrons is comparable to the thickness of the samples (0.5 mm) and the defects are therefore distributed throughout the sample. Since the defects are not limited to a surface layer the samples are also suited for measurements with the two-dimensional angular correlation setup.

6.1.3 Results

Angular correlation of annihilation radiation measurements

Semiconductor materials like Si, Ge and GaAs show a significant anisotropy along different crystal directions [2] as can be seen in figure 6.1. The structure is described as a valley and ridge structure and is caused by the anisotropy of the electron wavefunctions. The origin of the valley and ridge structure can be understood on the basis of group theory [10]. The positron is essentially in the ground state and, therefore, has a totally symmetric wavefunction; i.e., this function is invariant under any operation belonging to the point group of the crystal. Only electron wavefunctions whose representation themselves is totally symmetric will contribute to the annihilation rate. The upper two valence bands in Si do not belong to the totally symmetric representation [11, 12]. This suppression of annihilations with valence electrons causes the dip at zero momentum. The anisotropy is also visible in the projections. Figure 6.2 shows projections of 2D-ACAR distributions to form 1D-ACAR curves along the [100], [110] and the [111] direction. The distribution in the [100] direction has a plateau while along the [110] direction the distribution is peaked.

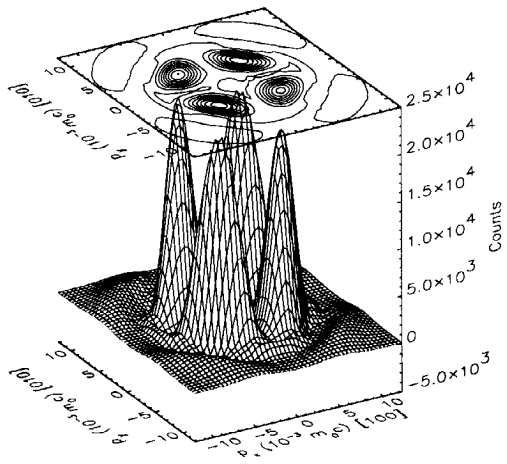

Figure 6.1: *Anisotropy plot of defect-free Si.*

Twelve Si samples were measured with the ACAR setup: three types of silicon (undoped, As doped and Sb doped) before and after irradiation with 1, 2 or 3×10^{18} e^-/cm^2. All samples had a (100) surface. The samples irradiated with 2×10^{18} e^-/cm^2 were split in three parts. Two

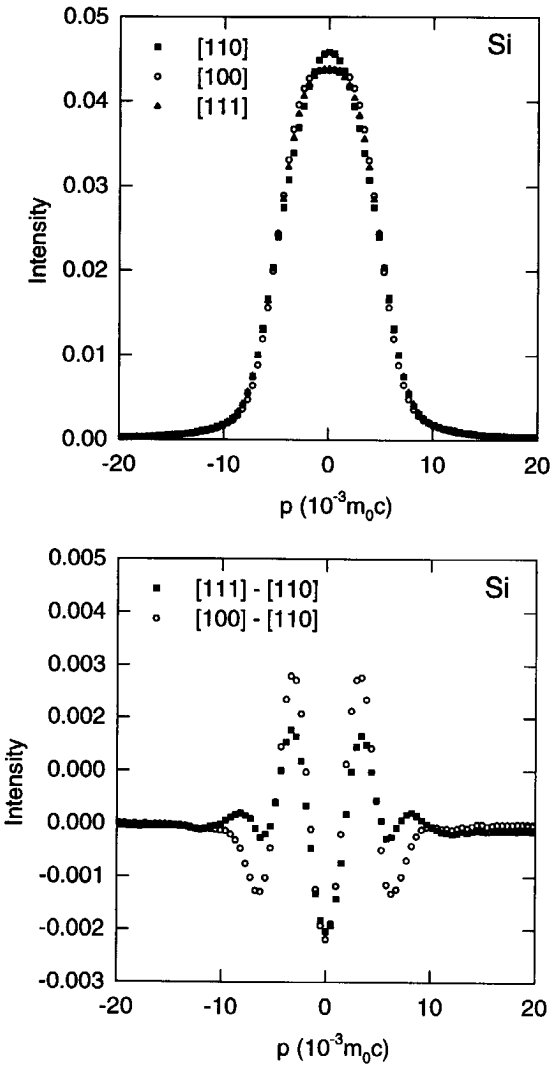

Figure 6.2: *Projections of 2D-ACAR distribution to obtain 1D-ACAR curves along the [100], [110] and [111] direction.*

small parts of 5×5 mm^2 were used for lifetime measurements and the longer part of 10×5 mm^2 was used in the ACAR experiments. The samples irradiated with 1 and 3×10^{18} e$^-$/cm^2 were not split and the sample size remained 10×10 mm^2. In section 4.7 it was shown that

the sample size influences the resolution of the setup. The general behaviour of the 2×10^{18} e^-/cm^2 irradiated samples is in agreement with the 1 and 3×10^{18} e^-/cm^2 irradiated samples but, in order to avoid introducing effects related to the different resolutions, the 2×10^{18} e^-/cm^2 irradiated samples were not used in the data analysis. All angular distributions are convoluted with a gaussian to obtain identical resolution functions in the x - and y-direction. The acquisition time of each data set was 300,000 s and the total number of accumulated counts varied between $43 \cdot 10^6$ and $50 \cdot 10^6$ counts. The distributions were normalised to the same contents of $50 \cdot 10^6$ counts to make it easier to compare the data sets.

Figures 6.3 to 6.8 show the ACAR measurement for the 3×10^{18} e^-/cm^2 irradiated sample and the anisotropy plots for all measurements. For the calculation of the anisotropy an isotropic function is subtracted from the distribution. The isotropic function is defined as the set of minimum values found on circles around the centre of the distribution. A complete description of the procedure can be found in section 4.6. Besides the anisotropy plot one can also calculate the anisotropy percentage. This percentage is the number of counts contained in the anisotropy plot compared to that of the original distribution. Table 6.1 shows the anisotropy percentage together with some other data for nine of the measured ACAR distributions. The contour lines are plotted at intervals of $1/10^{th}$ of the maximum value except for the first contour line. The first interval is split in four and instead of a thin solid line a thin dashed line is used. The interval between the dashed lines is $1/40^{th}$ of the maximum value. The line denoting zero is marked with a thick solid line. Since the anisotropy plots are scaled to the maximum value, differences in the anisotropy become more clear but at the cost of information about the intensity of the anisotropy. Information about the intensity of the anisotropy can be obtained by comparing the anisotropy percentage.

The anisotropy plots still have a structure that closely resembles that of defect-free material. This is not surprising since only a fraction of the positrons annihilate at defect sites. Furthermore, even if the positron annihilates at the defect site the atoms around the defect consist mainly of Si (even the highly As doped sample contains only 0.02 at% As).

The anisotropy plot for the undoped and the As and Sb doped samples before the irradiation all show the valley and ridge structure well known in semiconductors. Figure 6.9 shows cross-sections along the [100]-direction. The cross-sections and the anisotropy plots for the three samples are almost identical which indicates that the samples were defect-free. Lifetime measurements confirmed this and only one (bulk Si) lifetime component of 220 ps could be determined.

The 2D-ACAR measurements for the 1 and 3×10^{18} e^-/cm^2 irradiated undoped samples did not show any signature of a defect contribution. Figure 6.3 and 6.4 show that the anisotropy plot of

1 and 3×10^{18} e^-/cm^2 irradiated silicon can not be distinguished from the defect-free material. Also the cross-sections in figure 6.9 are almost identical. Almost all Frenkel pairs created during the irradiation have recombined, since no impurities were present to trap the vacancies. The small difference between the curve for the unirradiated sample and the 1 and 3×10^{18} e^-/cm^2 irradiated samples can be caused by a small contribution of divacancies. For example, Masher *et al.* [13] reported the creation of divacancies in 1×10^{18} e^-/cm^2, 3 MeV, irradiated CZ-Si and Hasegawa *et al.* [14] observed the creation of divacancies in FZ-Si after 8×10^{17} e^-/cm^2, 15 MeV, irradiation of FZ-Si. In the highly doped samples the presence of impurities prevents a fraction of the Frenkel pairs from recombining and the ACAR distribution for Si:Sb and Si:As after irradiation with electrons is more peaked than that of undoped Si (compare figure 6.3 with figures 6.5 and 6.7). The disappearance of the plateau and the appearance of a peak are even more clear in the cross-sections in figure 6.9. Also, the lifetime measurements for the 2×10^{18} e^-/cm^2 irradiated Si:Sb and Si:As samples revealed a longer average lifetime of 236 and 253 ps, respectively compared to the unradiated samples.

The change in the shape of the distribution is also clearly visible in the anisotropy percentage. A lower anisotropy percentage indicates a larger fraction of annihilations near defects. In the measurements for the unirradiated samples and the undoped Si about 5.6 % of the counts remains in the anisotropic part. The anisotropy for the doped silicon is clearly lower after irradiation, with anisotropies of 2.9 to 3.7 %. For the Si:Sb sample the anisotropy decreases for higher irradiation doses, which indicates that more defects were created and that the defect concentration is not high enough to trap all positrons. In the Si:As samples the effect of the higher dose is less obvious. There is only a small decrease in the anisotropy when the irradiation dose was increased from 1 to 3×10^{18} e^-/cm^2. This can indicate that only a small number of additional defects was created by the three times higher irradiation dose, or that the number of defects was already so large in the 1×10^{18} e^-/cm^2 irradiated sample that almost all positrons trap. The anisotropy in the measurement of the 1×10^{18} e^-/cm^2 irradiated Si:As is higher than that of the 3×10^{18} e^-/cm^2 irradiated Si:Sb. This indicates that the 1×10^{18} e^-/cm^2 irradiated Si:As sample contains more traps. When we compare the doping concentration this can be understood. The Si:As sample contains 200 ppm of As impurities while the Si:Sb sample only contains 40 ppm of Sb impurities (both samples have 20 ppm O atoms). In the Si:As sample the chance that a vacancy is trapped at an impurity is much higher during the irradiation then in Si:Sb sample.

To decompose the ACAR distribution into separate contributions for bulk Si and the defect, additional information is necessary. In principle, lifetime measurements could provide this information. Ambigapathy *et al.* [3], for example, used this method in their determination of the ACAR contributions for defects in GaAs. Our present lifetime measurements are not suited to provide this extra information since only one lifetime can be extracted. This is caused by the

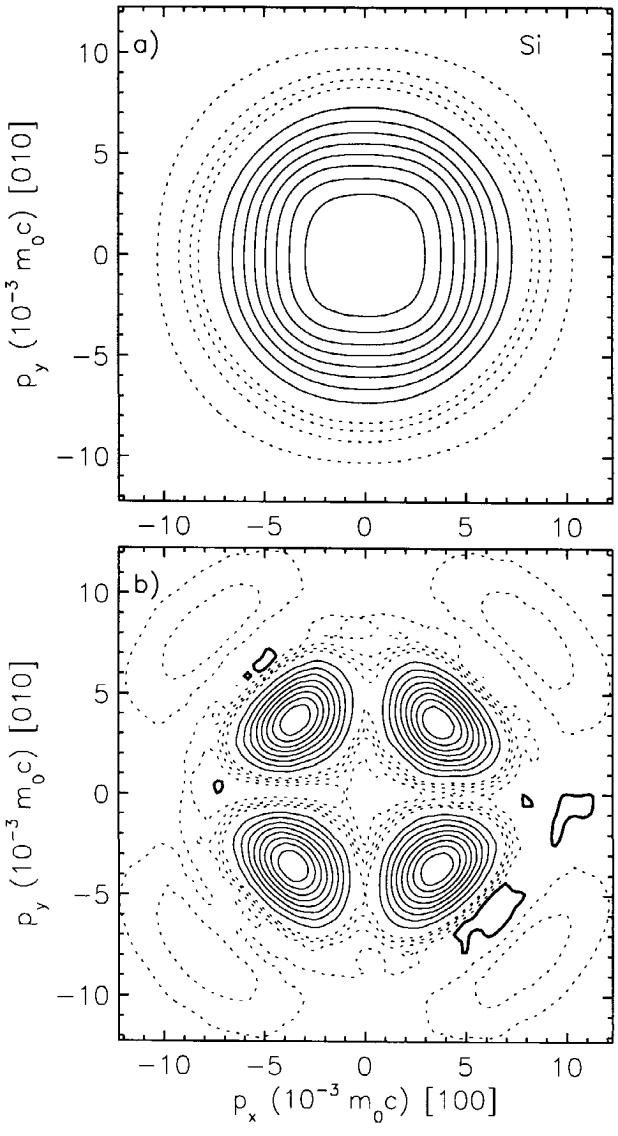

Figure 6.3: *a) ACAR distribution for the* 3×10^{18} e^-/cm^2 *irradiated undoped Si sample and b) the anisotropy plot for undoped Si before the irradiation with electrons.*

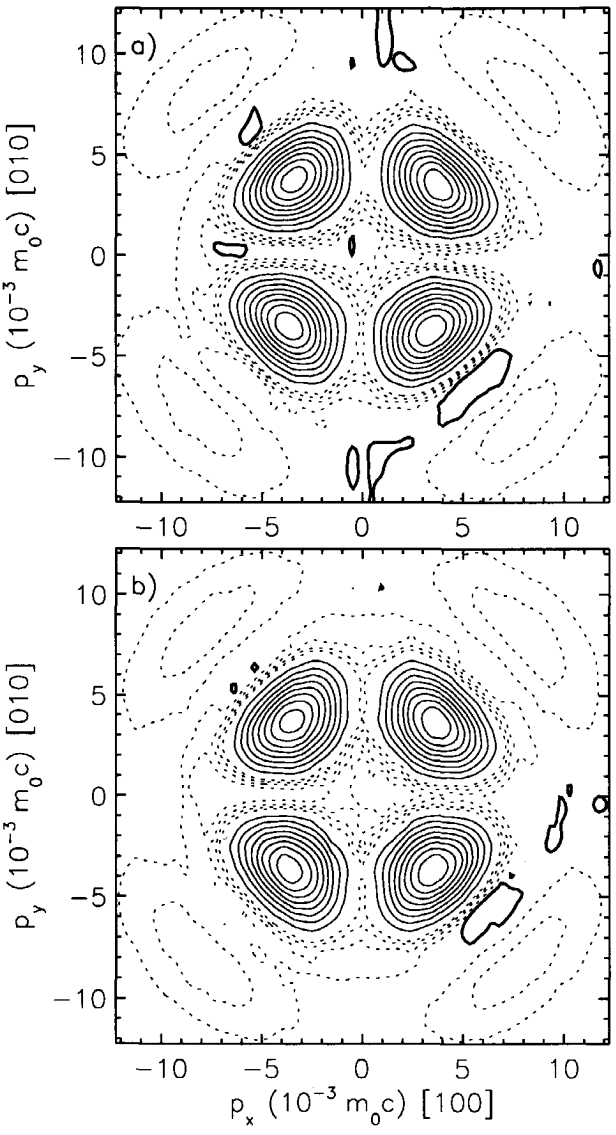

Figure 6.4: *Anisotropy plots for undoped Si after irradiation with a)* 1×10^{18} e^-/cm^2 *and b)* 3×10^{18} e^-/cm^2.

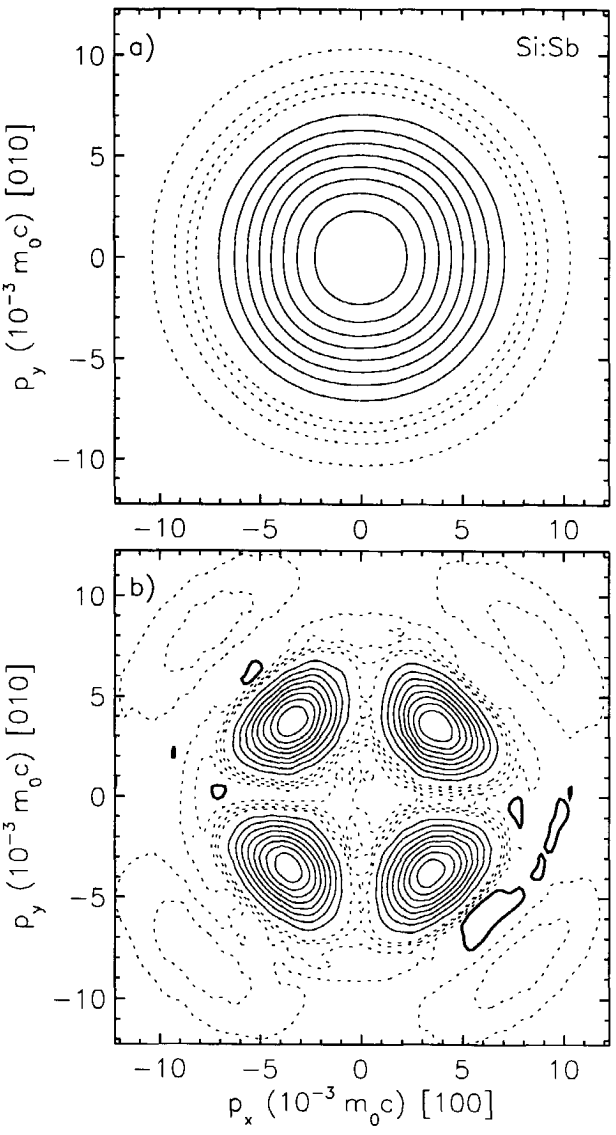

Figure 6.5: *a) ACAR distribution for the* 3×10^{18} e^-/cm^2 *irradiated Si:Sb sample and b) the anisotropy plot for Si:Sb before the irradiation with electrons.*

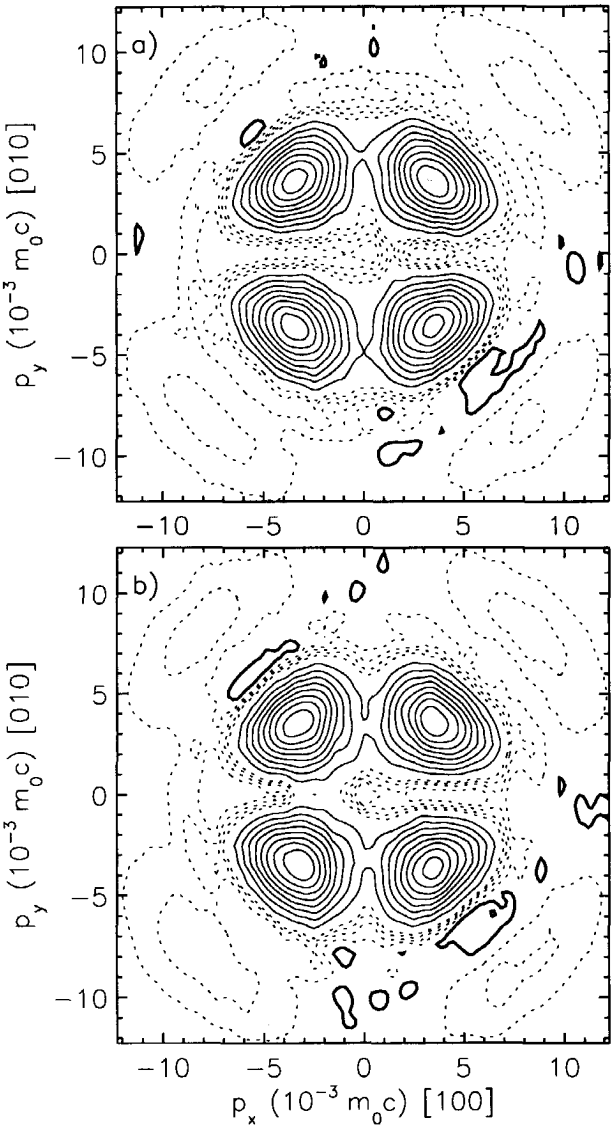

Figure 6.6: *Anisotropy plots for Sb doped Si after irradiation with a)* 1×10^{18} e^-/cm^2 *and b)* 3×10^{18} e^-/cm^2.

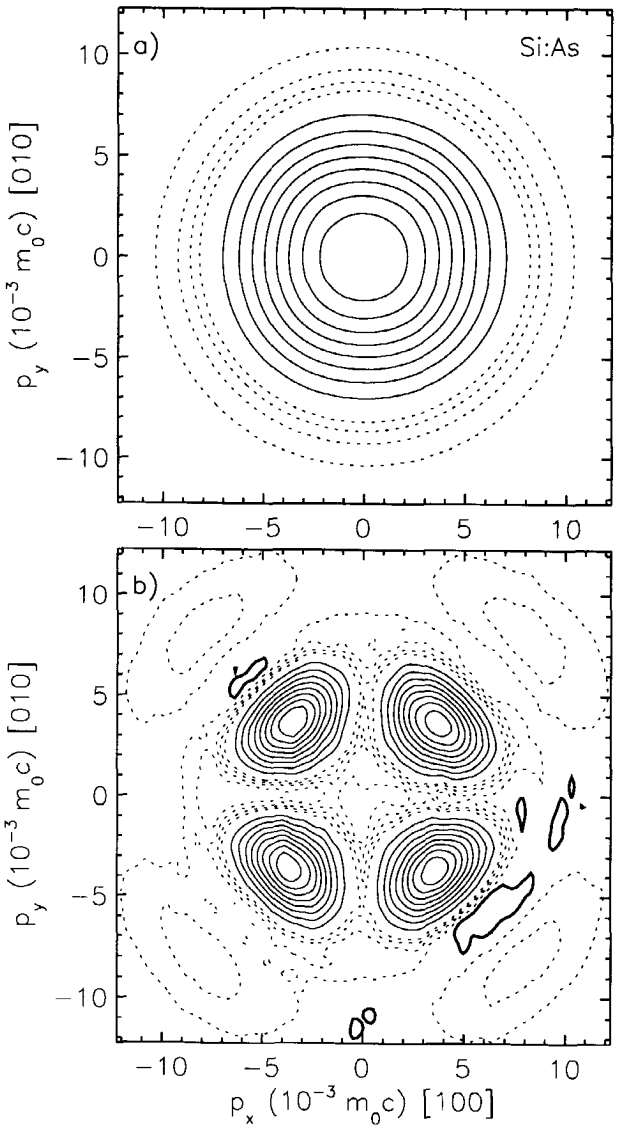

Figure 6.7: *a) ACAR distribution for the* 3×10^{18} e^-/cm^2 *irradiated Si:As sample and b) the anisotropy plot for Si:As before the irradiation with electrons.*

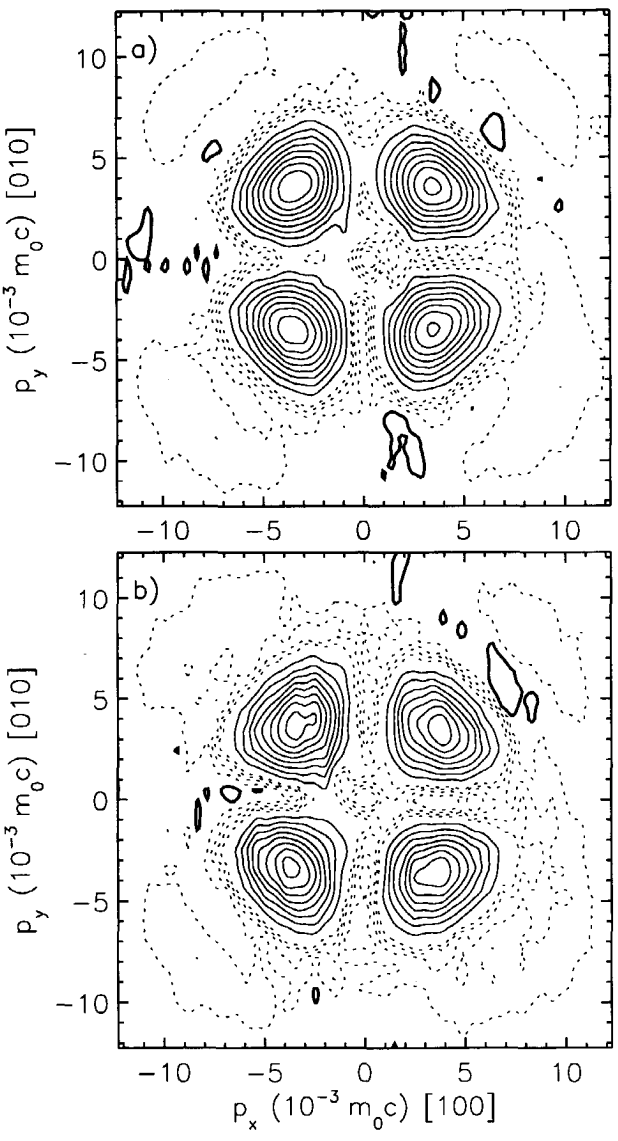

Figure 6.8: *Anisotropy plots for As doped Si after irradiation with a)* 1×10^{18} e^-/cm^2 *and b)* 3×10^{18} e^-/cm^2.

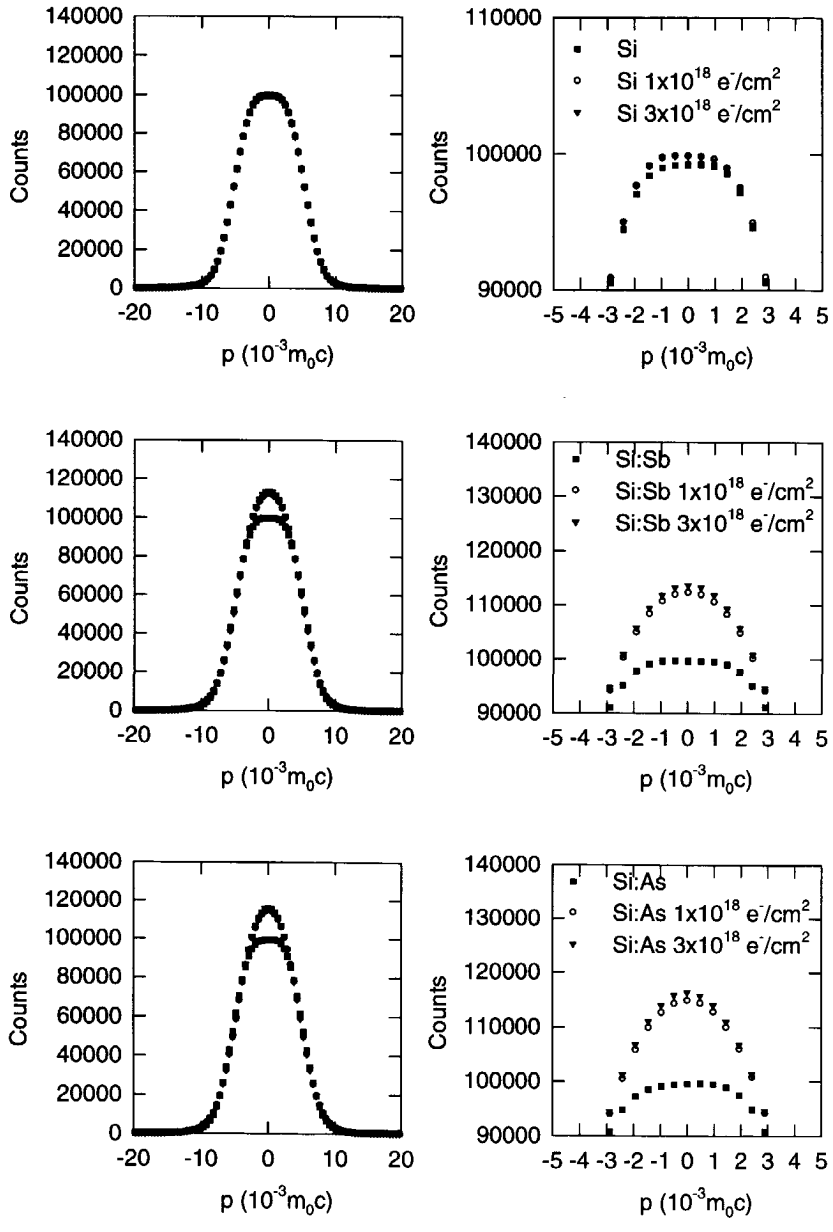

Figure 6.9: *Cross-sections through ACAR distributions along the [100] direction for defect-free Si, Si:Sb and Si:As and after irradiation with* 1 *and* 3×10^{18} e^-/cm^2. *The figures on the right contain the enlarged central parts of those on the left and show the differences more clearly.*

Table 6.1: Key data for the ACAR measurements for silicon before the normalisation to the same total number of counts.

Sample	Irradiation	Counts	Top	Anisotropy
Si		$47.56 \cdot 10^6$	95494	5.5 %
Si	1×10^{18} e$^-$/cm^2	$48.47 \cdot 10^6$	98251	5.5 %
Si	3×10^{18} e$^-$/cm^2	$48.12 \cdot 10^6$	97037	5.6 %
Si:Sb		$43.19 \cdot 10^6$	86862	5.7 %
Si:Sb	1×10^{18} e$^-$/cm^2	$46.81 \cdot 10^6$	106552	3.7 %
Si:Sb	3×10^{18} e$^-$/cm^2	$48.71 \cdot 10^6$	112427	3.3 %
Si:As		$46.04 \cdot 10^6$	89869	5.7 %
Si:As	1×10^{18} e$^-$/cm^2	$49.51 \cdot 10^6$	115537	3.1 %
Si:As	3×10^{18} e$^-$/cm^2	$49.13 \cdot 10^6$	116629	2.9 %

large source contribution of 20% and the small difference between the lifetime of defect-free silicon (220 ps) and vacancy-impurity defects ($\sim$ 260 ps).

As mentioned earlier, the isotropic function substracted from the distribution in order to obtain the anisotropy, is defined as the set of minimum values found on circles around the centre of the distribution. Instead of the minimum value one can also use the average value. By using the minimum value one obtains an anisotropy plot with only positive values. The use of the average value results in an anisotropy plot with positive and negative parts which is sometimes harder to interpret. On the other hand, the use of the average value results in an isotropic component which is a good description of the general shape of the distribution. Figure 6.10 shows these isotropic functions for electron irradiated Si:As and Si:Sb when the average value is used. The difference between the curve for defect-free silicon and the curves for silicon with defects is clear. The curves for silicon with defects resemble each other, the largest differences occur around $p = 0$. But these differences are strongly related to the fraction of positrons that trap at defects and cannot be used to identify the atoms around the defect site. Close inspection of the curves shows an interesting difference between the curves for Si:Sb and Si:As. At $8 \times 10^{-3}\, m_0c$ the curves for 1 and 3×10^{18} e$^-$/cm^2 irradiated Si:Sb samples are on top of each other. This is also the case for the 1 and 3×10^{18} e$^-$/cm^2 irradiated Si:As samples. But the curves for Si:As and Si:Sb are well separated (see figure 6.10b). This small difference also affects the anisotropy plots for electron irradiated Si:As. Figure 6.5 shows the anisotropy plots for the measurements of the Sb doped samples. The top in these figures is scaled to unity. The anisotropy plot for the measurement of the unirradiated sample is almost identical to the anisotropy plots of those that were irradiated. In the anisotropy plots for the measurements of the As doped samples in figure 6.7 we can see a difference. Although also these anisotropy plots show the same structure as those of defect-free silicon, with a large peak at $(\pm 3, \pm 3) \cdot 10^{-3} m_0c$ and a smaller peak at

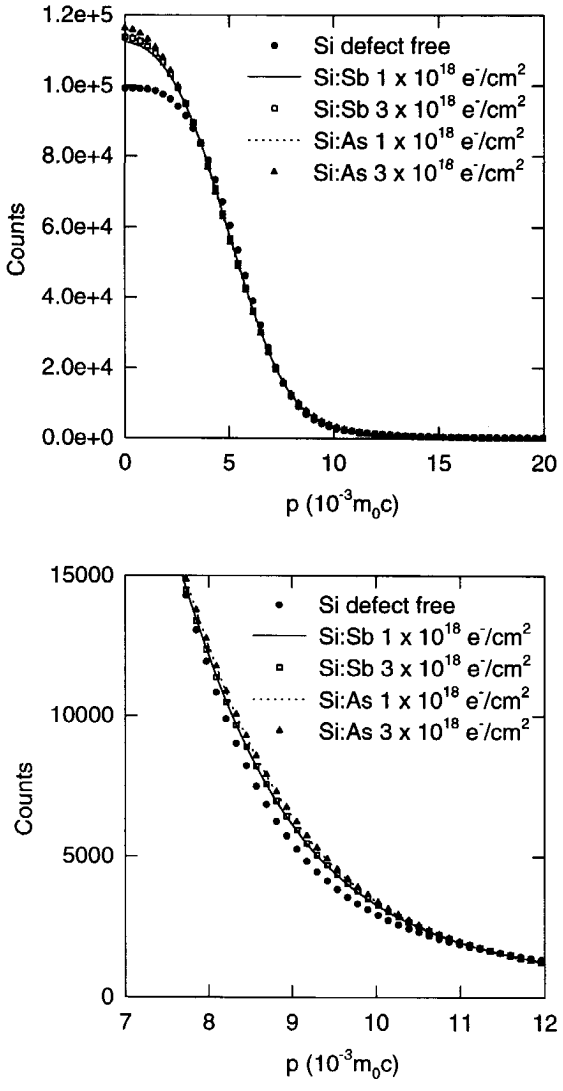

Figure 6.10: *Average isotropic component for the ACAR distributions for defect-free Si and Si:Sb and Si:As after irradiation with* 1 *and* 3×10^{18} e^-/cm^2.

$(\pm 8, \pm 8) \cdot 10^{-3} m_0 c$, the ratio between the peak heights is different. The difference is small but significant.

Based on the ACAR measurements we come to the following conclusions:

- For positrons, the distributions for the doped samples before irradiation are identical to those for defect-free silicon.
- The irradiation with electrons creates defects in the doped samples. The main defects are vacancy-impurity complexes. The distributions for the undoped samples after the electron irradiation are almost identical to those for defect-free silicon. The undoped silicon samples after the irradiation can still be considered as almost defect-free.
- For the Sb doped Si we still observe a relation between the irradiation dose and the anisotropy. This indicates that more defects are created, when the irradiation dose is increased. For the As doped Si the relation between the number of traps and the irradiation dose is less obvious.
- The defects created by the irradiation of Si:Sb and Si:As have a similar signature, but a small difference is present at 8×10^{-3} $m_0 c$. This difference is visible in the anisotropy plot and the isotropic part.

Single detector Doppler broadening measurements

The single detector Doppler broadening measurements were performed with the VEP beamline at the Delft University of Technology. All S and W values are normalised to those of defect-free Si. The defects are created throughout the sample and we can expect an S-E curve that starts at a surface value (in these sample at ~ 0.94 S_{bulk}) and increases to the defect or bulk value (in the case of the defect-free samples). An example of such a curve can be seen in figure 6.11. The steepness of the curve is determined by the positron diffusion length, L_+. In defect-free material the diffusion length is related to the positron diffusion coefficient by [15]:

$$L_+ = \sqrt{D_+ \tau_b} = \sqrt{\frac{D_+}{\lambda_b}}, \tag{6.1}$$

with $\tau_b = \lambda_b^{-1}$, the positron bulk lifetime. In materials with defects L_+ is reduced to an effective diffusion length, $L_{+,eff}$, given by:

$$L_{+,eff} = \sqrt{\frac{D_+}{\lambda_b + \kappa_t}}, \tag{6.2}$$

where κ_t is the positron trapping rate into defects. The positron trapping rate itself is given by

$$\kappa_t = \nu_t c_t \tag{6.3}$$

with ν_t the specific trapping rate or trapping coefficient and c_t the concentration of defects. The trapping rate can be calculated from L_+, since both the bulk lifetime of 218-222 ps [1, 16] and the diffusion coefficient of 2.8 cm^2/s are known for silicon. But it is not the trapping rate itself that we are interested in but the concentration of defects. To calculate the concentration of defects, the specific trapping rate for the defect should be known. In metals the trapping process is reasonably well understood, and the specific trapping rate for a monovacancy is of the order of 10^{15} s^{-1} for all metals and at all temperatures. In semiconductors, vacancies give rise to several localised electron levels in the energy gap. The charge state of a vacancy depends on the position of the Fermi level with respect to the electron levels. The charge state of a defect has a profound effect on positron trapping and the specific trapping rate may vary by orders of magnitude. Puska *et al.* [8] calculated the temperature dependence of the specific trapping coefficient for differently charged vacancy defects in silicon. A positively charged vacancy has a very low trapping coefficient ($\sim 10^{13}s^{-1}$) that becomes even smaller at low temperatures. Neutral vacancies have a trapping coefficient comparable to that of metals and the trapping coefficient is temperature independent. Negatively charged defects have a trapping coefficient larger than $10^{15}s^{-1}$. The more negatively charged the defect, the higher is the trapping coefficient. Furthermore, the trapping coefficient increases for lower temperatures. In lifetime measurements one can directly calculate the trapping rate κ. In our experiment we can only determine the effective diffusion length. This makes it harder to determine the temperature relation of κ (and thus ν_t) since also the diffusion coefficient is temperature dependent. Theoretically, a $T^{-1/2}$ dependence is predicted [17] for D_+ if acoustic-phonon scattering is the motion limiting factor. Measurements for metals and semiconductors in an extended temperature range [18–21] have confirmed this dependence. This temperature dependence is used to calculate the D_+ values below 300K in table 6.2.

To perform the measurements at low temperatures the sample holder in the VEP is replaced by a cooled sample holder which is connected to a closed-cycle refrigeration system. The sample holder is continuously cooled to 10 K by expanding helium gas. When higher temperatures are preferred the sample holder is simultaneously heated and cooled. A controller measures the temperature, compares it with the desired temperature and adjusts the current through the heating section. To reduce the heating due to radiation of the walls of the vacuum system the holder is surrounded with a radiation shield (see figure 6.12). The radiation shield has a hole with a diameter of 15 mm as entrance for the positrons. The positron beam size and centre change slightly as a function of the acceleration voltage [22]. In the setup with the cold finger the position of the sample with respect to the beam is fixed. Depending on the positron energy, the beam will partially miss the sample and hit the sample holder. This resulted in large fluctuations in the S parameter as a function of the positron energy for the first set of measurements. These effects are avoided by mounting the sample in such a way that only the sample is irradiated by the positrons, or by using bigger samples. Both options are not possible in the present

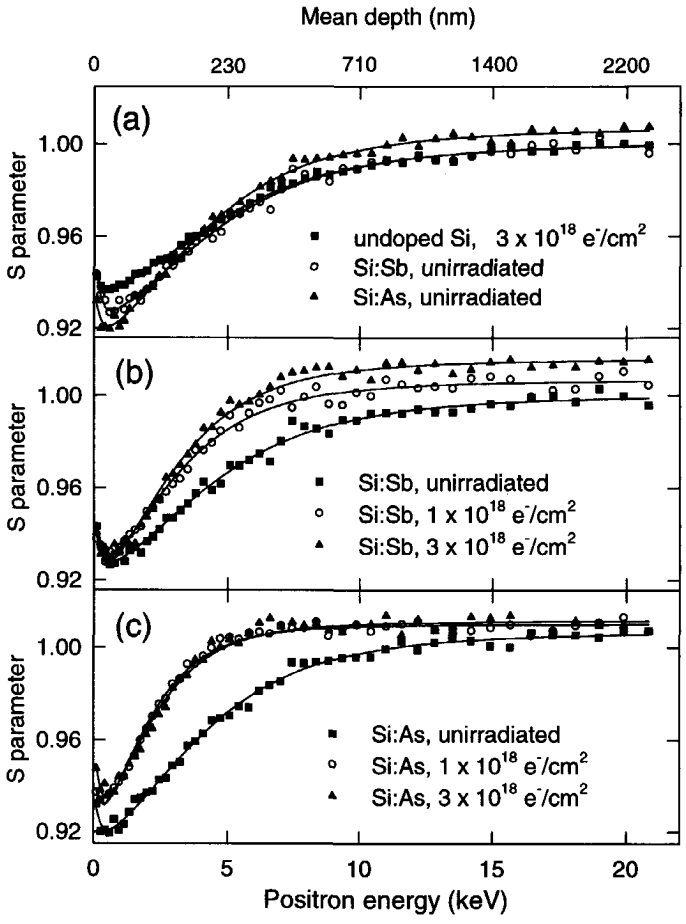

Figure 6.11: *Doppler broadening measurements at room temperature for doped and undoped silicon before and after electron irradiation. The solid lines are fits obtained with VEPFIT.*

setup. The beam size and position can be adjusted by changing the current through the coils used for the beam guidance. The problem is that for each acceleration voltage different settings will give the best result; i.e., for each energy a new setting has to be determined. To accomplish this, the radiation shield and the central part of the cold finger were removed. This leaves a hole with a diameter of 15 mm in the sample holder. Of course this cannot be done for a real measurement since it makes cooling of the sample impossible. The best settings are obtained

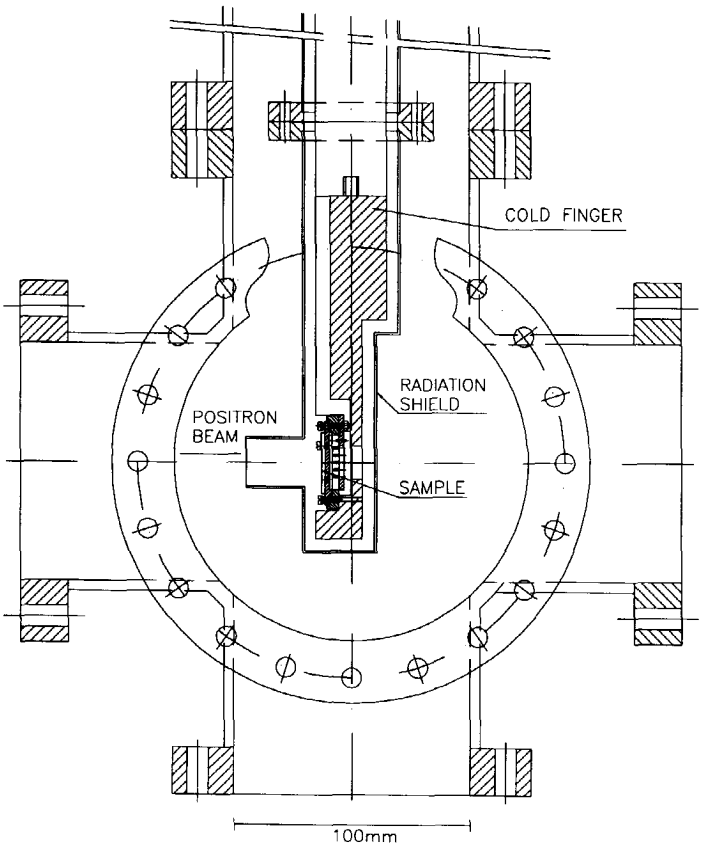

Figure 6.12: *Cross-cut of the cooled sample holder.*

when all positrons go through the hole and do not annihilate with the cold finger. To accomplish this the current through the coil was adjusted (between certain limits) and the setting with the lowest count rate was determined. This was done for each energy and the settings were stored in a data file. During the real measurements these data were used to adjust the beam so that the positrons only hit the centre of the cold finger where the sample is mounted. This method gave an improvement in the data.

A selection was made of the electron irradiated samples and the non-irradiated starting material. The S-E curves are fitted with VEPFIT (model 5 with two surface and one defect contribution) to determine the effective diffusion length. According to the fitting program, the error in the diffusion length is smaller than 5 nm. However, some data sets had a large scattering in the data

points due to the problems already mentioned with the positioning of the sample with respect to the beam. This can introduce a systematic error in the diffusion length, but the trends in the change of the diffusion length as a function of the temperature are still correct.

Figure 6.11a shows the results of the Doppler broadening measurements for the non-irradiated Si:As and Si:Sb samples and for the undoped sample irradiated with 3×10^{18} e^-/cm^2. All curves increase to an S value close to that for defect-free material, in agreement with the ACAR measurements which also did not give any indication of defects. The fit with VEPFIT gave a long diffusion length for all three curves. The diffusion length of 256 nm for the undoped sample is in good agreement with the expected value of 250 nm based on the values of the diffusion coefficient and the lifetime in the literature. The values for unirradiated Si:As (195 nm) and unirradiated Si:Sb (230 nm) are slightly shorter than those for defect-free undoped silicon. This is in agreement with the results of Bauer-Kugelmann *et al.* [23]. They determined a diffusion coefficient of 1.57 cm^2/s for highly As doped Si and 2.48 cm^2/s for highly Sb doped Si. Using their diffusion coefficients we expect a diffusion length of 186 nm in Si:As and 234 nm in Si:Sb. Both values are in good agreement with the measured diffusion lengths of 195 nm and 230 nm. Figures 6.11b and c show the S-E curves measured at room temperature for the Sb and As doped samples before and after the electron irradiation. The irradiation introduces defects and the diffusion length becomes considerably shorter. The calculated diffusion lengths for the 1 and 3×10^{18} e^-/cm^2 irradiated Si:Sb samples are only slightly different, 128 and 123 nm, respectively, and the calculated trapping rates of $\sim 10^{10}s^{-1}$ are almost identical in both samples. This is surprising since differences in the ACAR measurements and the difference in the final S values, 1.006 and 1.02 respectively, indicate a larger difference in defect concentration. In 1 and 3×10^{18} e^-/cm^2 irradiated Si:As samples the irradiation with the lowest dose gave an even shorter diffusion length than the 3×10^{18} e^-/cm^2 irradiation. In these samples we expect an almost identical trapping rate based on the nearly identical ACAR distributions and S values at high implantation energies. This is also reflected in the S-E curves for the 1 and 3×10^{18} e^-/cm^2 irradiated Si:As samples in figure 6.11c which are almost identical. The trapping rate in the electron irradiated Si:As is about three times larger than that in the electron irradiated Si:Sb, but as one can see in table 6.2, the trapping rate is very sensitive to small differences in the calculated diffusion length. The observed S values of ~ 1.01 indicate defects with only one vacancy-dopant complex, since for vacancy clusters higher S values are reported [4,34], and are in agreement with the S value of 1.00 observed by Jackman *et al.* [25] in As doped Si epilayers grown by MBE.

The resemblance between the S-E curves for 1 and 3×10^{18} e^-/cm^2 irradiated Si:Sb makes one cautious as to other effects which may influence the diffusion length. For instance, the presence of electrical fields in the semiconductor can strongly affect the diffusion length. The native oxide layer on the surface causes an unknown electric field in the near surface region. The oxide

Table 6.2: Effective diffusion length and trapping rate calculated with VEPFIT. The temperature marked with a star are measured with the cooled sample holder. The diffusion coefficients at room temperature are determined by Bauer-Kugelmann *et al.* [23] and those below room temperature are calculated with a $T^{-1/2}$ dependence described in the text.

Sample	Irradiation (e^-/cm^2)	Temperature (K)	$L_{+,eff}$ (nm)	D_+ [23] (cm^2/s)	κ_t (s^{-1})
Si	3×10^{18}	300	256	2.8	
Si:Sb		300	230	2.48	
Si:As		300	195	1.57	
Si:Sb		300	230	2.48	
Si:Sb	1×10^{18}	300	128	2.48	$1.1 \cdot 10^{10}$
Si:Sb	3×10^{18}	300	123	2.48	$1.2 \cdot 10^{10}$
Si:Sb	1×10^{18}	300*	105	2.48	$1.7 \cdot 10^{10}$
Si:Sb	1×10^{18}	100*	88	4.3	$5.9 \cdot 10^{10}$
Si:Sb	1×10^{18}	10*	62	13.6	$35 \cdot 10^{10}$
Si:As		300	195	1.57	
Si:As	1×10^{18}	300	65	1.57	$3.3 \cdot 10^{10}$
Si:As	3×10^{18}	300	74	1.57	$2.4 \cdot 10^{10}$
Si:As	1×10^{18}	300*	57	1.57	$4.3 \cdot 10^{10}$
Si:As	1×10^{18}	200*	51	1.9	$6.9 \cdot 10^{10}$
Si:As	1×10^{18}	100*	42	2.7	$14 \cdot 10^{10}$
Si:As	1×10^{18}	10*	35	8.6	$60 \cdot 10^{10}$

layer can be removed by an HF-etch but this leaves us with another problem: the surface S value becomes almost identical to that of bulk Si. The difference between the surface and bulk S is necessary to determine the diffusion length. One can create an artificial difference between the bulk and the surface by evaporating a thin Au layer on top of the silicon. The Au layer should be so thin that it only influences the S-E curve below 1 keV. This method was used by Mäkinen *et al.* [19, 20] to determine the diffusion coefficient in Si. The diffusion lengths for the defect-free Si:As and Si:Sb samples were in good agreement with diffusion coefficients determined by Bauer-Kugelmann *et al.* [23]. This indicates that, at least for the non-irradiated samples, the influence of the oxide layer is small but does not mean that the effect can be excluded for the other samples.

Two samples were measured at low temperatures. Figure 6.13 shows the results for the 1×10^{18} e^-/cm^2 irradiated Si:Sb sample. The large scattering in the data points is caused by alignment problems of the sample with respect to the beam. For the measurement of the 1×10^{18} e^-/cm^2

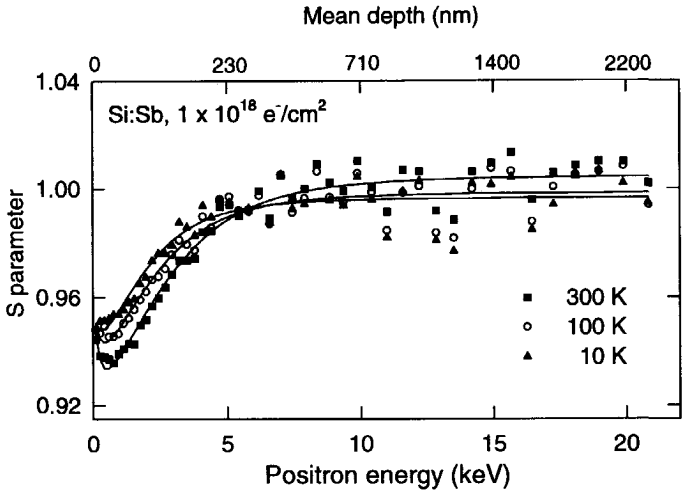

Figure 6.13: *Doppler broadening measurements for* 1×10^{18} e^-/cm^2 *irradiated Si:Sb as a function of temperature. The solid lines are fits obtained with VEPFIT.*

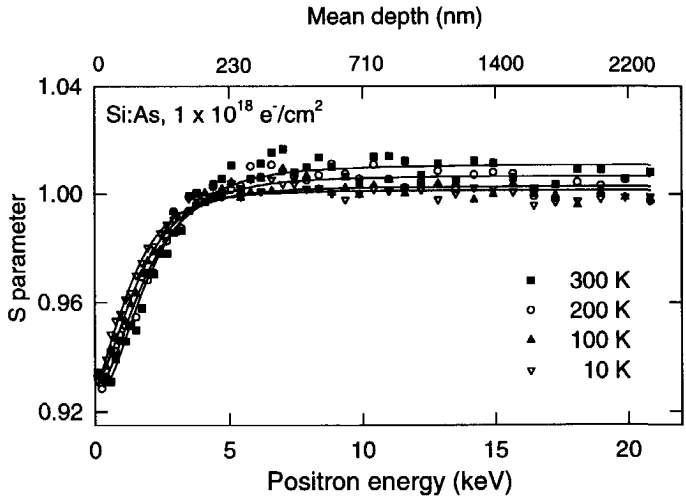

Figure 6.14: *Doppler broadening measurements for* 1×10^{18} e^-/cm^2 *irradiated Si:As as a function of temperature. The solid lines are fits obtained with VEPFIT.*

irradiated Si:As sample the beam was adjusted for each energy by using predetermined settings. This removed most of the scattering in the data points as can be seen in figure 6.14. Measurements were also performed at room temperature for both samples to investigate the effects of the mounting on the cold finger. The measurements for Si:Sb and Si:As resulted in shorter diffusion lengths than those determined when the samples where mounted in the default sample holder. This indicates that some systematic error is introduced. The trend in the diffusion length as a function of temperature is clear however. In table 6.2 one can see that the diffusion length decreases as a function of temperature even when the diffusion coefficient increases as a function of temperature. This means that κ_t increases dramatically for low temperatures. Only negatively charged defects show this behaviour and we conclude therefore that the defects in the electron irradiated Si:Sb and Si:As samples are negatively charged.

Since we have now determined the sign of the charge of the defects we can approximate the defect concentration. Mäkinen *et al.* [26] measured a trapping coefficient of $2.0 \times 10^{15} s^{-1}$ at room temperature for negatively charged phosphorus-vacancy (P-V) centres in Si. In an earlier study of Mascher *et al.* [13] the trapping coefficient for negatively charged divacancies was estimated at $3.5 \times 10^{15} s^{-1}$. We expect a comparable trapping coefficient and assume a value of $3.0 \times 10^{15} s^{-1}$ at room temperature for the trapping coefficients of As-V and Sb-V defects. For electron irradiated Si:Sb we determined a κ_t of $1 \times 10^{10} s^{-1}$; with $\nu_t = 3.0 \times 10^{15}$ this corresponds to a defect concentration of 3 ppm. For the electron irradiated Si:As the concentration of defects is determined as 10 ppm. The concentration of As in the Si:As samples is 7 times larger than the concentration of Sb in the Si:Sb samples and a larger fraction of the created vacancies are trapped at an impurity in the Si:As sample than in the Si:Sb sample.

Based on the one-detector Doppler-broadening measurements we come to the following conclusions:

- The diffusion lengths in the unirradiated starting material are in good agreement with those of defect-free material.
- The electron irradiated undoped silicon has a diffusion length identical to that of defect-free material.
- The S value of the defects indicates defects with only one vacancy.
- The electron irradiation in Si:As and Si:Sb creates negatively charged defects.
- Assuming a trapping coefficient of $3 \times 10^{15} s^{-1}$ the defect concentration in electron irradiated Si:Sb is 3 ppm and in Si:As 10 ppm.

Two-detector Doppler broadening measurements

To investigate the contribution of the core electrons to the momentum distribution, measurements were performed with the two-detector setup described in section 3.3. This setup has a peak to background ratio of $10^5 : 1$ which allows an accurate measurement of the high-momentum region. To avoid any surface contribution we used a positron implantation energy of 25 keV. Conventional Doppler measurements of the S-parameter versus the energy showed no change in the S-parameter above 8 keV for the irradiated Si and above 14 keV in the unirradiated Si.

We constructed the diagonal cross-sections of the two-dimensional spectra for Si, Si doped with As irradiated with 3×10^{18} e^-/cm^2 and Si doped with Sb irradiated with 3×10^{18} e^-/cm^2. The obtained low-background Doppler broadening curves are shown in figure 6.15. The distributions for the unirradiated and irradiated Si(not shown) are quite different at small momenta but our particular interest lies in the high-momentum tail where we hope to observe the contributions of core electrons.
We obtained ratio curves by dividing the momentum distributions of the irradiated Si samples by that of unirradiated Si (see figure 6.16). The characteristics of the ratio curves are a peak at $\pm 9 \times 10^{-3} m_0 c$ and a ratio below 1 at high momenta. The high-momentum tail of the distribution is clearly different from that of Si, but it is not possible to distinguish the differently doped samples by the shapes of the curves. We do however see a small difference in the amplitudes of the peaks and valley's. The As-doped Si sample shows the larger amplitude as we would expect in view of the 10 times higher doping concentration. The difference at 9×10^{-3} $m_0 c$ can also be related to the small difference we noticed in the ACAR distributions at 8×10^{-3} $m_0 c$. But it is not a signature that is useful to characterise Si:As defects since the effect in the Doppler broadening curve is too small to distinguish Sb and As related defects. Although the samples are heavily doped, a large fraction of the annihilations will still occur in the vicinity of Si atoms. This will obscure the influence of the doping atoms and may explain why we do not see a clear difference in the shapes of the ratio curves. Another possibility is that the high-momentum tails of As and Sb resemble one another.

6.1.4 Conclusions

Vacancy-impurity complexes in silicon were investigated. Both the doping (undoped, As and Sb) and the doses (0, 1, 2 and 3×10^{18} e^-/cm^2) were varied. The irradiation of undoped material did not reveal the creation of defects. This can be expected since the Frenkel pairs can recombine and the concentration of impurities (10^{16} O/cm^3) is so low that even when the vacancies trap at these impurities the concentration is below our detection limit of $\sim$ 1 ppm. In the highly doped samples with impurity concentrations above 10^{18} $/cm^3$, vacancy creation is confirmed

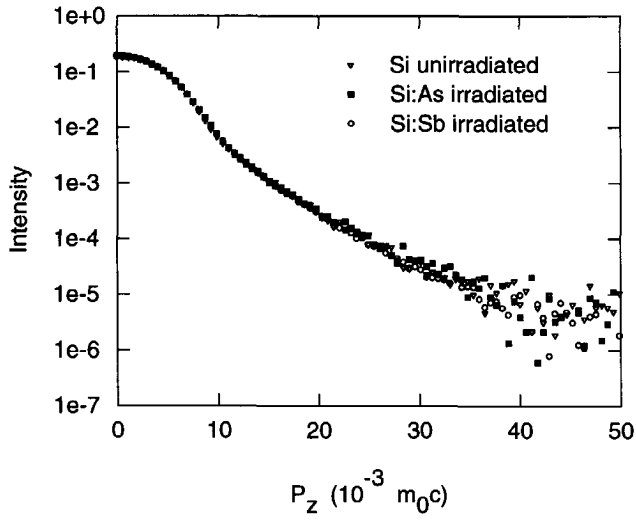

Figure 6.15: *Two-detector Doppler broadening measurements for defect-free silicon and* 3×10^{18} e^-/cm^2 *irradiated Si:Sb and Si:As.*

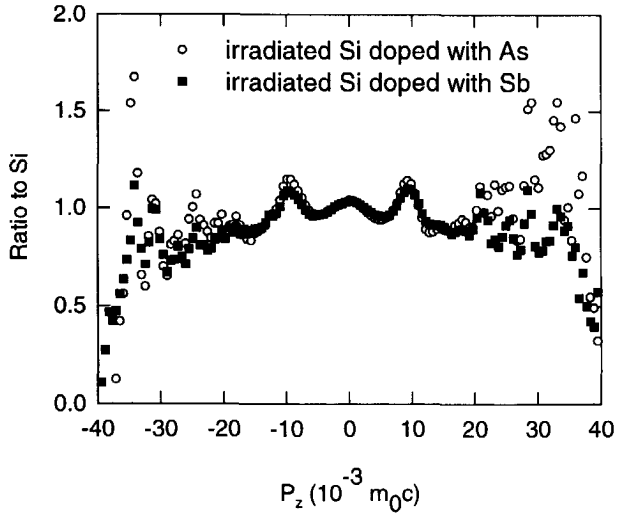

Figure 6.16: *Ratio curves of* 3×10^{18} e^-/cm^2 *irradiated Si:Sb and Si:As to defect-free silicon.*

by a higher S value, a longer lifetime, a shorter diffusion length and a more isotropic ACAR distribution. The defects are determined to be negatively charged Sb-V and As-V complexes with concentrations of $\sim$ 3 ppm and $\sim$ 10 ppm, respectively. The characteristic contributions for both defects are similar. The high-momentum part of the two-detector Doppler broadening curve did not reveal a characteristic signature that can be used to distinguish between annihilations near As and Sb atoms. However, the ACAR measurement showed a very small difference at $9 \times 10^{-3}\ m_0c$ between the measurements of the electron irradiated Si:Sb and Si:As samples.

6.2 Oxygen implanted silicon

6.2.1 Introduction

An understanding of the behaviour of oxygen-related defects in Si crystals is very important for the manufacture of Si wafers. Oxygen is for example used for the strengthening of Czochralski (CZ)-Si, in which it traps harmful metallic impurities, and in the manufacture of Silicon-On-Insulator (SOI). In SOI a thin top layer of crystalline silicon is separated from the rest of the wafer by an insulating layer. This approach has advantages over the use of Si wafers. In the manufacturing of electronic devices only the top layer $\sim 1\mu$m is actually used for the active elements. The remaining part of the wafer is only needed for mechanical support. The use of an insulator instead of a semiconductor makes it possible to reduce the separation of the active elements.

One of the most promising methods of manufacturing SOI is Separation by IMplantation of OXygen or SIMOX. In the manufacture of SIMOX a Si wafer is implanted with $1.7 \cdot 10^{18}$ cm^{-2}, $\sim$ 180 keV oxygen ions. The sample is kept at 600°C to prevent amorphisation of the top silicon layer. After the implantation the wafer is annealed at 1350°C in a slightly oxidising environment for several hours (6 h in Ar-1%O_2). This process will create a top layer of crystalline silicon, that has almost the qualities of bulk silicon, and an insulating layer of Buried OXide (BOX), that separates the top layer from the Si-wafer. The formation of the buried oxide of SIMOX is a highly sensitive process with regard to the implantation parameters and the high temperature anneal. Minor changes of these parameters may result in unexpected large effects on the BOX properties [27].

The oxygen in both CZ-Si and SIMOX will bind vacancies and form vacancy-oxygen complexes. Positron annihilation techniques are well suited to investigate these defects [6,13,28,29]. The characteristic value of the S parameter for the multivacancy-multioxygen defect (V_xO_y) strongly depends on the ratio of x to y [1, 13, 29, 30]. Recently Fujinami investigated the defect formation as a function of anneal temperature and implantation doses. Since the effect strongly

depends on the ion dose, both low ($\sim 10^{15}$ /cm^2) [31] and high ($\sim 10^{18}$ /cm^2) [32] implantation doses were studied. A selection of Fujinami's samples is used in our present study. To obtain more information about the annihilation site we use the two-detector Doppler broadening setup in the hope of improving the defect identification.

6.2.2 Experimental

Silicon (CZ, p-type) was implanted with 180 keV oxygen ions. The implantation angle was 7° with respect to the (100) surface to avoid channelling effects. The investigated samples can be divided into two groups: one group is implanted with low ion doses of up to 2×10^{15}, the other group is implanted with 1000 times higher doses. The first group consists of samples implanted with four different doses of 2×10^{14}, 5×10^{14}, 1×10^{15} and 2×10^{15} O$^+$/cm^2. After irradiation at room temperature the samples were annealed at temperatures up to 800°C. Each anneal had a duration of 30 minutes and was performed in a nitrogen atmosphere. The second group of samples was implanted with a considerably higher ion dose. Three different doses of 2×10^{17}, 4×10^{17} and 1.7×10^{18} were used. The implantation was performed at 550°C. After the implantation the samples were annealed at 700°C to 1350°C (the melting point of Si is 1410°C). Each anneal had a duration of 1 hour and was performed in a N_2 atmosphere (t < 1050°C) or in an Ar + O_2 atmosphere (t > 1050°C). The native oxide layer on the silicon was removed with an aqueous HF solution prior to the measurement.

6.2.3 Results

Low dose implantation

The implantation of oxygen ions displaces the Si atoms and creates vacancies. Figure 6.17 shows the results of a computer simulation with the computer code TRIM (TRansport of Ions in Matter) [33]. The top layer of the sample has a high concentration of vacancies compared to the oxygen concentration even after the assumption of 99 % recombination (90 % recombination is a more realistic value). Figure 6.18 shows the slow-positron beam measurements with one Ge-detector. The measured S and W values are divided by those of defect-free Si to obtain relative S and W values. The curves are in good agreement with those of Fujinami [31]. After the implantation a high S value is measured. High S values are usually associated with vacancy-type defects [4]. For this implantation we can expect di-vacancies (V_2), vacancy clusters with n vacancies (V_n) and vacancy-oxygen complexes such as VO and V_2O. The relative S value of ~ 1.05 generally indicates a V_n-based defect [4]. Nielsen *et al.* [34] proposed a value of 1.044 S_{bulk} for V_n defects in silicon.

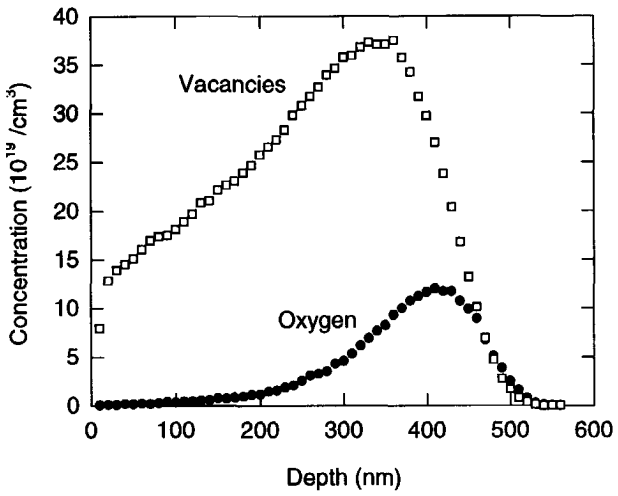

Figure 6.17: *The oxygen and vacancy profile as calculated with TRIM for 180 keV implantation of* 2×10^{15} O^+/cm^2. *For the vacancy profile a recombination fraction of 0.99 is assumed.*

During the annealing simple defects are transformed into more complex defects but up to 500°C the S-E curves are rather similar. After annealing at 600°C the S-E curve begins to change. The S-E curve initially still increases to 1.03 S_{bulk} but then drops very rapidly to reach a minimum at ~ 7 keV (mean implantation depth 400 nm). The positrons with implantation energies of 7 keV probe the region with a high oxygen concentration due to the ion implantation. In this region multivacancy-multioxygen complexes (V_xO_y) are formed with a large oxygen content($x \leq y$); these defects have a low S value of 0.90 S_{bulk} [35]. In the first 200 nm the oxygen concentration is not high enough to form these defects and in this region V_nO ($n \geq 3$) type defects dominate [31]. During the anneal at 800°C the V_nO defects are annealed out and only the multivacancy-multioxygen complexes remain. After the anneal at 800°C, the very low relative S value that is ascribed to this defect, becomes obvious. There is also a clear relation between the implantation dose and the defect concentration, as can be seen in figure 6.19. Except for the lowest dose all S-E curves show a minimum at 6 keV. The measured S value at 6 keV decreases with increasing doses. This indicates a larger fraction of positrons that annihilate at the multivacancy-multioxygen sites.

The measured S and W parameters can both be described as linear combinations of specific contributions of the bulk and trapping sites. Each type of defect can be characterised by a point

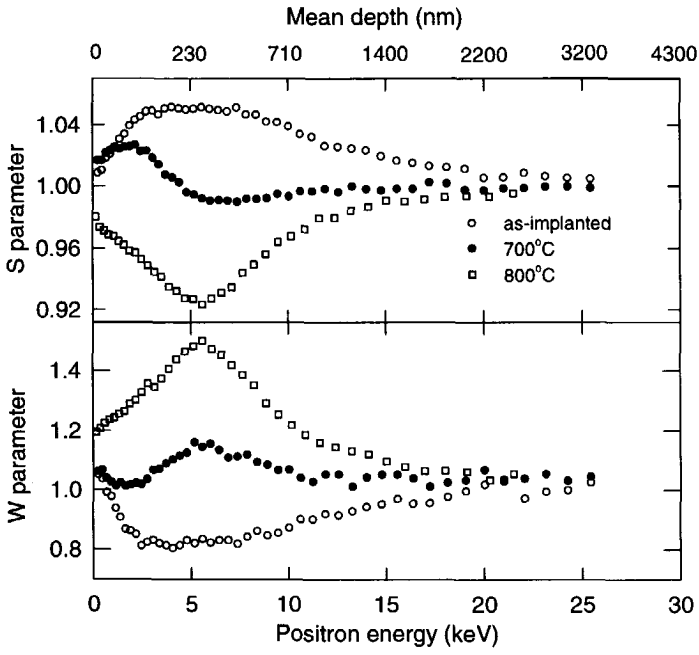

Figure 6.18: *S and W parameter versus positron energy for the* 2×10^{15} O^+/cm^2 *implanted sample as-implantated and after annealing at 700°C and 800°C.*

in the S-W plot. An S-W curve, obtained by varying the energy of the positrons, can roughly be characterised by data points that lie on straight lines between the characteristic S-W points of annihilation sites. The characteristic S-W point is only reached if all positrons, implanted with a specific energy, annihilate at one specific type of site. Except for the bulk and the surface this is seldom the case. Consequently, this means that the S-W curves rarely reach the characteristic S-W point. The S-W curves are a useful aid in determining the kind and the number of different annihilation sites that play a role. In figure 6.20 the S-W curves are shown for the low dose implantations. The curves start at a surface S-W point which is sample dependent, run toward a defect S-W point (which is not reached) and go to the bulk S-W point at (1.0, 1.0) according to its definition. The curve for 2×10^{14} O^+/cm^2 shows no structure but the curves for all other doses exhibit the same behaviour and run toward the point for multivacancy-multioxygen defects at (0.9, 1.7) which was determined with VEPFIT and is in agreement with the proposed S value of 0.9 S_{bulk} by Nielsen *et al.* [34].

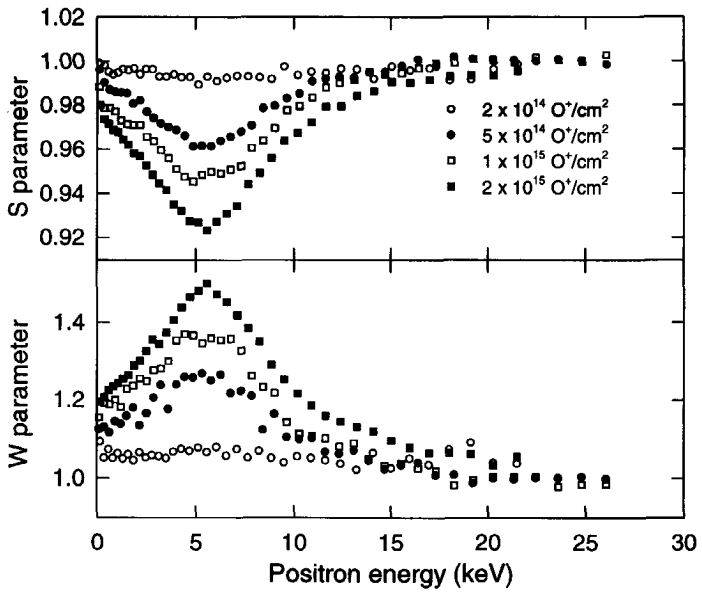

Figure 6.19: *S and W parameter versus positron implantation energy for doses of* 2×10^{14} O^+/cm^2 *to* 2×10^{15} O^+/cm^2 *annealed at 800°C.*

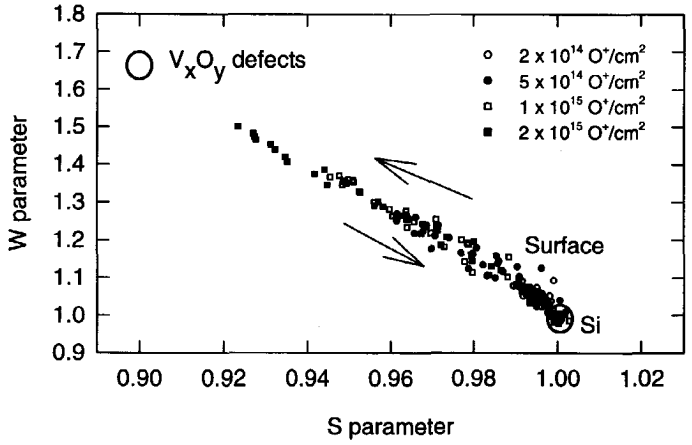

Figure 6.20: *S-W plots for the samples implanted with* 2×10^{14} O^+/cm^2 *to* 2×10^{15} O^+/cm^2 *annealed at 800°C. The running parameter is the implantation energy of the positrons.*

Additional measurements were performed with a two Ge-detector setup. The low background of this setup opens the possibility of performing accurate measurements of the high momentum part of the Doppler broadened annihilation spectra which provide information about the chemical environment of the annihilation site [36, 37]. Since the Doppler broadened spectra extend over several orders of magnitude, each curve is divided by the curve of defect-free Si to emphasise differences. Figure 6.21 and 6.22 show the ratio curves for the low dose implantations. To smooth the curves a three point moving average was used. The main feature in the ratio curves is a peak at $10 \times 10^{-3} m_0 c$. This peak is present in all ratio curves but is itself not characteristic for vacancy-oxygen defects. The DBAR curve for defect-free contains a kink at 10×10^{-3} $m_0 c$ which is caused by the decrease of the contribution to the DBAR curve of the band electrons outside the Jones zone. When the translation symmetry is disturbed due to the presence of defects this kink becomes less pronounced and a peak in the ratio curve is the result. A comparable peak for example was observed in doped Si irradiated with electrons as described in section 6.1. Figure 6.21 shows the ratio curves of the 800°C annealed samples in which large V_xO_y clusters are expected. The peak at 10×10^{-3} $m_0 c$ in the ratio curves has a shoulder on the high momentum side (the ratio curve does not drop below 1). This shoulder is very clear for the 5×10^{14} O^+/cm^2 to 2×10^{15} O^+/cm^2 implanted samples. In the sample implanted with the lowest dose of 2×10^{14} O^+/cm^2 the shoulder is less pronounced and the ratio curve is around one. Figure 6.22 shows the ratio curves for the sample implanted with 2×10^{15} O^+/cm^2. The ratio curve for 2 keV, mean implantation depth 50 nm, drops below 1 at 13×10^{-3} $m_0 c$ while the ratio curve for 7 keV, mean implantation depth 400 nm, shows a shoulder similar to the ratio curves for the samples annealed at 800°C. This indicates that the formation of the vacancy-oxygen clusters in the region around 400 nm begins already at 700°C owing to the high oxygen content in this region [31].

High dose implantation

Figure 6.23 shows the slow positron beam measurements with one Ge-detector. The curves are again in good agreement with those of Fujinami [32]. The results for the samples implanted with 2×10^{17} O^+/cm^2 and 4×10^{17} O^+/cm^2 annealed at 1000°C are almost identical. In the S-W plot (figure 6.24a) the curves show the same behaviour as the low dose implanted samples annealed at 800°C and the ratio curves (figure 6.26a) show a shoulder at 17×10^{-3} $m_0 c$. In these samples the main defects are multivacancy-multioxygen defects, probably in combination with SiO_2 precipitates.

In the manufacture of SIMOX the implantation dose used is very important. The S-E curve in figure 6.23 for the 1.7×10^{18} O^+/cm^2 implanted sample is very different compared to those of the 2 and 4×10^{17} O^+/cm^2 implanted samples. In figure 6.23 the S-E curve has a local max-

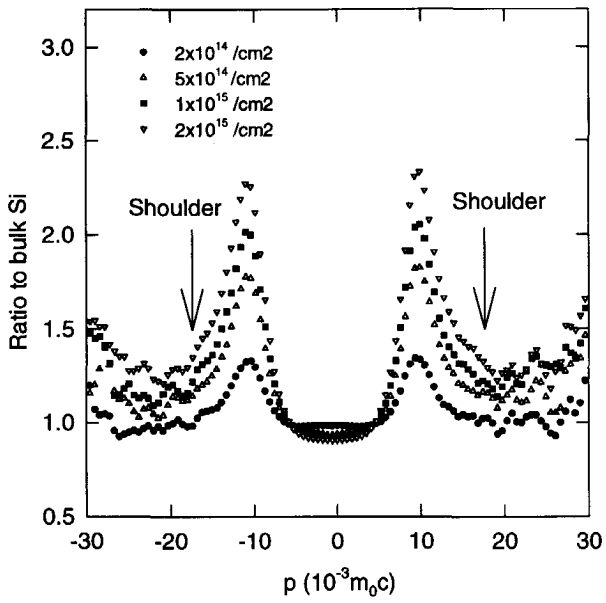

Figure 6.21: *Ratio curves of two-detector measurements for the* 2×10^{14} O^+/cm^2 *to* 2×10^{15} O^+/cm^2 *implanted samples annealed at 800°C. The ratio is calculated by dividing the measured Doppler-broadening curve for the implanted sample by the curve for defect-free silicon.*

imum at 6 keV for the 1.7×10^{18} O^+/cm^2 implanted sample instead of a minimum as for the 2 and 4×10^{17} O^+/cm^2 implanted samples. The S-W plot in figure 6.24b makes it clear that this sample can not be described with a simple model with a surface, a defect and a bulk region. Besides a contribution from the surface and the bulk, at least three additional contributions are necessary. Figure 6.25 shows cross-sectional transmission electron microscopy micrographs before and after annealing at 1100°C, 1200°C and 1350°C for the 1.7×10^{18} O^+/cm^2 implanted sample. In the first 200 nm spheroidal voids are formed aligned in columns parallel to the O^+ beam direction. In the region from 200 to 600 nm an amorphous SiO_2 layer is formed. After annealing at 1350°C the voids in the top layer are annealed out and an almost-bulk-quality silicon layer with a thickness of 170 nm is formed. The amorphous SiO_2 forms a 430 nm thick BOX layer during this anneal with some Si islands located near the interface between BOX and substrate Si. The S-E and W-E curves have been fitted with VEPFIT [15]. For the fit a structure was used with three layers and two interfaces between the layers. The layer thickness was based on the TEM micrographs. The results of the fit are the lines in figures 6.23 and 6.24b. The fitting program determines for each layer and interface an S and a W value to represent

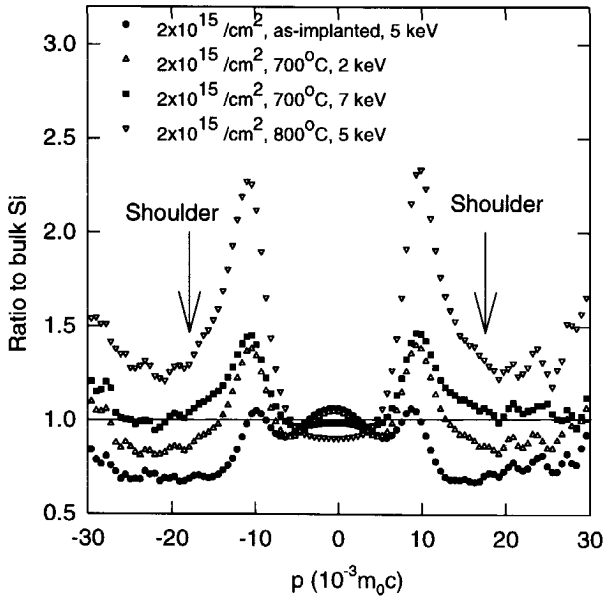

Figure 6.22: *Ratio curves of two-detector measurements for the* 2×10^{15} O^+/cm^2 *implanted samples.*

different annihilation sites. The effect of the different contributions is most easily seen in the S-W plot in figure 6.24b. The curve starts at a surface value ([0.975, 1.3] for this sample), runs toward the V_xO_y point, bends over to a point attributed to SiO_2 [38], runs again in the direction of V_xO_y defects and finally goes to the value of bulk Si. Although the top silicon layer has the electrical properties of defect-free bulk silicon and no precipitates can be observed on the TEM micrographs, the S value is still lower than that of bulk silicon. For the fit it is necessary to assume a top layer with a low S value just like the V_xO_y defects.

Additional two-detector measurements were performed to obtain additional information about the SIMOX sample. To probe different layers, positron energies of 1.5 (Si top layer), 6 (BOX layer) and 11 keV (interface BOX-Si) were used. The ratio curves in figure 6.26b all show a peak at 10×10^{-3} m_0c with a shoulder at 17×10^{-3} m_0c. Based on the ratio curves of the low dose implantations this indicates the presence of oxygen in all layers. The S-W plot already showed that the top layer of the 1.7×10^{18} O^+/cm^2 implanted sample annealed at 1000°C still contains V_xO_y defects. This is confirmed by the ratio curve of the 1.5 keV measurement in figure 6.26a. This ratio curve is comparable with ratio curves of samples with V_xO_y defects

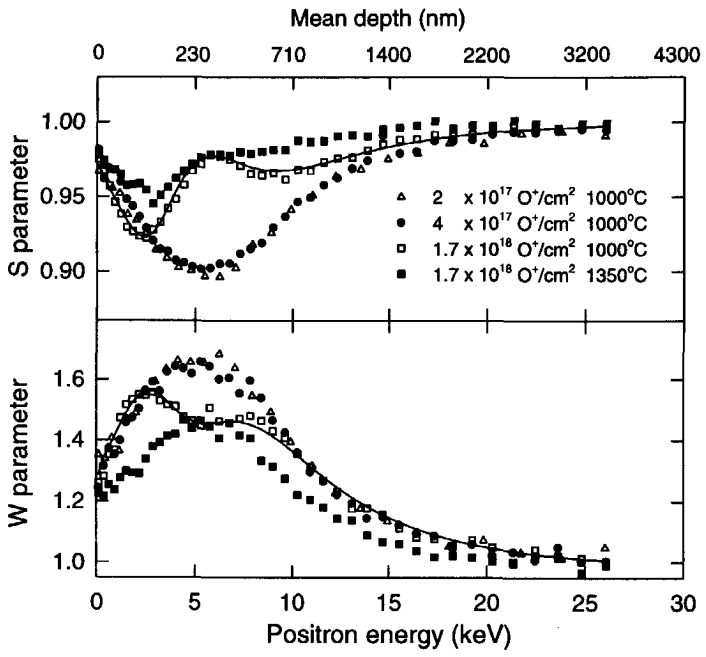

Figure 6.23: *S and W parameter versus positron energy for the samples implanted with 2, 4 and* 17×10^{17} O^+/cm^2. *The solid line is a fit obtained with VEPFIT for the* 1.7×10^{18} O^+/cm^2 *implanted sample annealed at 1000°C.*

(figure 6.21). Although the anneal step from 1000°C to 1350°C does remove a part of the defects in the top layer (in the S-W plot the data points in figure 6.24b come closer to the V_xO_y point than in figure 6.24c), there still remain V_xO_y defects in the sample. The measurement at 6 keV predominantly probes the buried oxide layer of SiO_2. A signature of oxygen can be expected. This is indeed the case. The ratio curve at high momenta ($> 10 \times 10^{-3}$ m_0c) shows the same behaviour as the ratio curves of samples with V_xO_y defects although the ratio above 25×10^{-3} m_0c rises more rapidly for the V_xO_y defects than for the SiO_2. The ratio curve around $p = 0$ on the other hand is quite different as one can expect. The main contribution around $p = 0$ in the Doppler broadening curves stems from the valence electrons and the binding of these electrons in SiO_2 is different from that in Si. A part of the difference can also be caused by the formation of positronium in the SiO_2 layer [39]. The annihilation of para-Ps results in a narrow peak in the Doppler broadening spectrum with the width of the system resolution. The Doppler

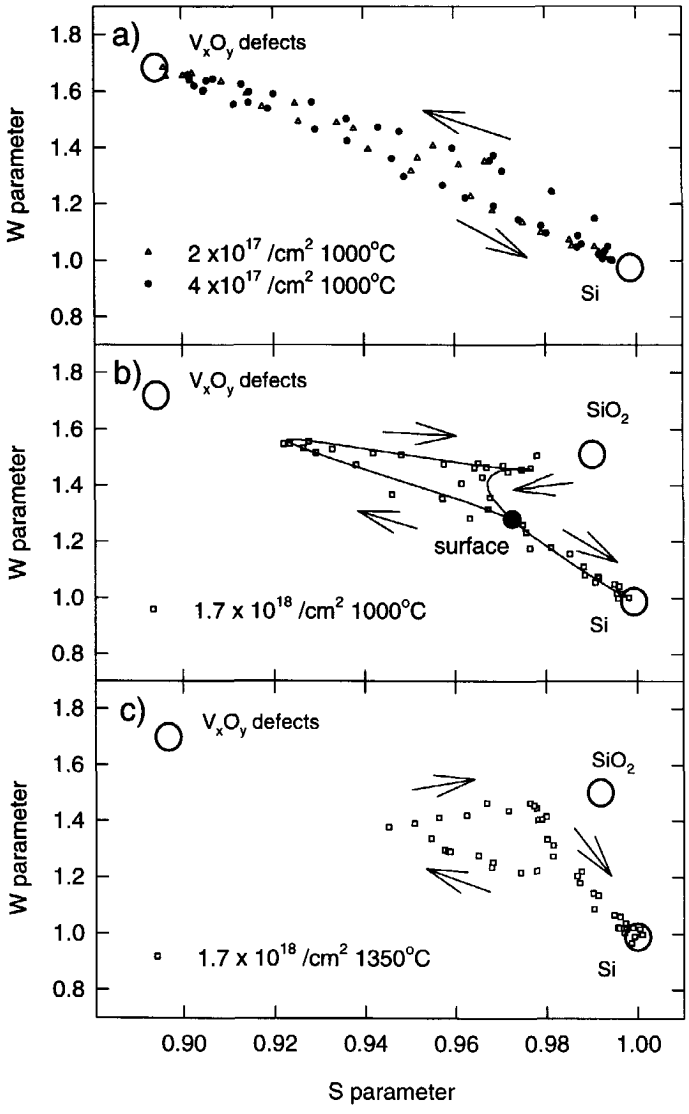

Figure 6.24: *S-W plot for high dose implantations: a) 2 and* 4×10^{17} O^+/cm^2 *annealed at 1000°C, b)* 1.7×10^{18} O^+/cm^2 *annealed at 1000°C (open squares) and c)* 1.7×10^{18} O^+/cm^2 *annealed at 1350°C. The arrows indicate the direction to points with higher positron implantation energy. The large circles mark characteristic contributions. The solid line in b) represents the fit obtained from VEPFIT.*

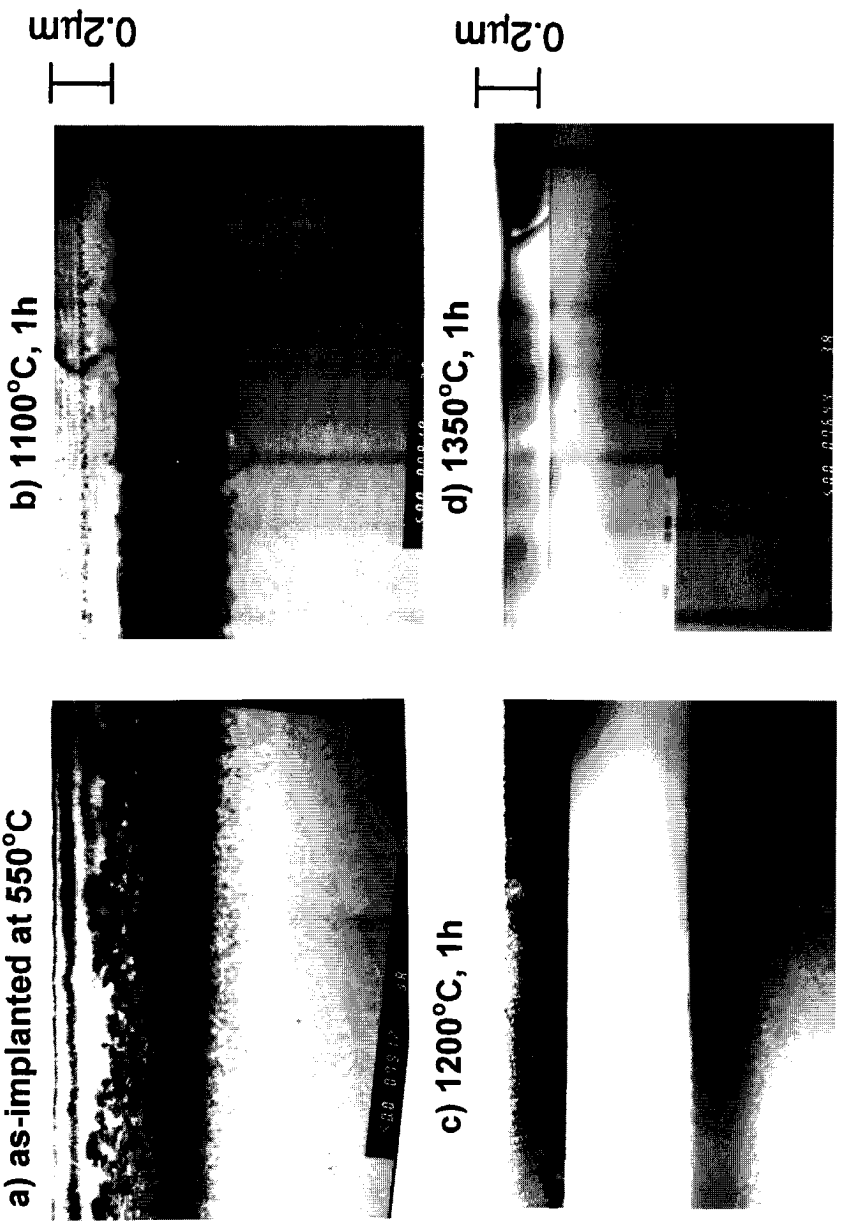

Figure 6.25: *Cross-section transmission electron microscopy micrographs of the* 1.7×10^{18} O^+/cm^2 *sample before(a) and after annealing at 1100°C(b), 1200°C(c) and 1350°C(d).*

broadening curve for the SiO_2 layer is indeed sharper than that of Si as can be derived from the ratio curve in figure 6.24b. The difference in the Doppler broadening curves also underlines the additional information present in these curves. The central parts of their Doppler broadening curves have very different shapes although the S parameter values of 1.00 for Si and 0.99 for SiO_2 are almost identical.

6.2.4 Decomposition

The Doppler broadened spectrum, as the S parameter, is a linear combination of several contributions. The count rate x at channel j in a spectrum can be expressed by:

$$x(j) = \sum_i f^i x^i(j) \tag{6.4}$$

with i labelling all different contributions, f^i representing the fraction of annihilations resulting in a contribution i and $x^i(j)$ the unknown count rate in channel j for contribution i. The fractions f^i can be obtained by using a program such as VEPFIT that solves the positron diffusion equation. Four contributions are included in the VEPFIT analyses: two surface contributions (one for thermal positrons and one for epithermal positrons), one contribution for the defect and one for bulk Si. The VEPFIT program can use different models to describe the sample. The most widely applicable is the so called 'model 5' in which the sample is described by a layered structure. Within the layer a uniform defect profile is assumed and one characteristic S value is assigned to this layer. The use of a uniform defect profile is a simplification, as can be seen from the TRIM calculations (see figure 6.17). Therefore, instead of 'model 5', 'model 3' is used, in which the sample is described by a gaussian defect profile.

To decompose the Doppler broadened spectra into separate contributions a system of equations of the form:

$$x_E(j) = f_E^s x^s(j) + f_E^d x^d(j) + f_E^b x^b(j) \tag{6.5}$$

is solved, with $x_E(j)$ the count rate of the Doppler broadened spectrum in channel j at positron energy E, $f_E^{(s,d,b)}$ the fraction of annihilations resulting in a contribution for the surface, defect and bulk, respectively, and $x^{(s,d,b)}(j)$ the unknown count rate of the surface, defect and bulk in channel j. Since the contribution of epithermal positrons is very small for the positron energies used, this contribution was neglected in the decomposition. Decomposition into these contributions is useful for obtaining fingerprints of defects.

The decomposition method was applied to two of the low dose implanted samples. Two-detector Doppler broadened spectra were acquired for four positron energies for the sample implanted

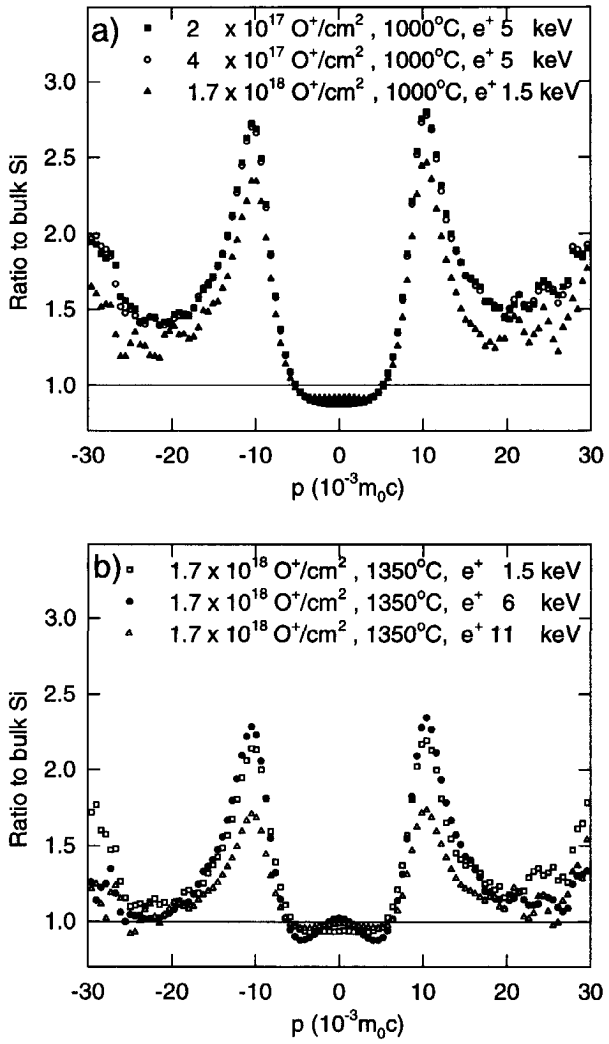

Figure 6.26: *Ratio curves for: a)* 2×10^{17} O^+/cm^2 *and* 4×10^{17} O^+/cm^2 *implanted samples measured with a positron implantation energy of 5 keV, and* 1.7×10^{18} O^+/cm^2 *implanted sample measured with a positron implantation energy of 1.5 keV; all samples were annealed at 1000°C and b)* 1.7×10^{18} O^+/cm^2 *implanted samples annealed at 1350°C and analysed with positrons implanted with energies of 1.5, 6 and 11 keV.*

Table 6.3: Fractions of positrons annihilating at the surface, the defect site and bulk Si, obtained with VEPFIT for the sample implanted with 5×10^{14} O^+/cm^2 and annealed at 800°C.

Positron energy (keV)	surface	defect	bulk
3.0	0.60	0.19	0.20
5.0	0.33	0.32	0.35
8.0	0.14	0.24	0.62
25.0	0.01	0.01	0.98

with 5×10^{14} O^+/cm^2, and for five positron energies for the sample implanted with 2×10^{15} O^+/cm^2. Both samples were annealed at 800°C. The spectrum for the 2×10^{15} O^+/cm^2 sample was fitted with the aid of VEPFIT. For the implantation profile of the positrons the Makovian profile was used. The diffusion coefficient (D_+) in Si was set to 2.8 cm^2/s, the specific trapping rate (ν) to $3 \times 10^{14}/s$ and the free annihilation rate (λ_b) to 4.5×10^9. Both S_{bulk} and S_{defect} were fixed. The result of the fit was a gaussian defect profile with a centroid at 350 nm and a FWHM of 200 nm. The spectrum for the 5×10^{14} O^+/cm^2 sample was fitted with the same parameters and with the same defect profile. The agreement between the fit and the data is slightly worse than for the 2×10^{15} O^+/cm^2 data (see figure 6.27) This is not surprising since the fit was more restricted and we use a relatively simple model of the sample. Table 6.3 and 6.4 show the fractions obtained for the relevant contributions at the positron energies used. Our approach is slightly different from previous work [40] in which we calculated the contribution of the *defect region*(model 5) instead of the *defect*(model 3). The contribution of the defect region is still a combination of annihilation in bulk silicon and at the defect site. In samples with a high trapping rate the differences between the contributions of the defect region and the defect itself are small since almost all positrons will annihilate at defect sites. Consequently, the decomposed contributions were almost identical for the 2×10^{15} O^+/cm^2 sample in the old and the new approach. The 5×10^{14} O^+/cm^2 sample has a smaller trapping rate and the contribution obtained for the *defect region* will therefore be different from that obtained for the 2×10^{15} O^+/cm^2 sample although the *defect type* is identical. By using 'model 3' we are able to compare the results of the decompositions.

Figure 6.28 shows the extracted contributions for the surface, defect and bulk obtained by a decomposition of the two-detector Doppler-broadening spectra of the sample implanted with 2×10^{15} O^+/cm^2 annealed at 800°C. The same procedure is applied to the spectra of the sample implanted with 5×10^{14} O^+/cm^2 and annealed at 800°C. Figures 6.29a-f compare the extracted contributions for both sets of measurements. Figures 6.29b, d and f show the curves on a logarithmic scale and with an expanded range. The scattering in the extracted curves is larger for the 5×10^{14} O^+/cm^2 sample than for the 5×10^{15} O^+/cm^2 sample due to statistics.

Table 6.4: Fractions of positrons annihilating at the surface, the defect site and bulk Si, obtained with VEPFIT for the sample implanted with 2×10^{15} O^+/cm^2 and annealed at 800°C.

Positron energy (keV)	surface	defect	bulk
1.5	0.82	0.13	0.05
3.0	0.51	0.38	0.11
5.0	0.22	0.60	0.18
8.0	0.07	0.45	0.48
21.0	0.00	0.05	0.95

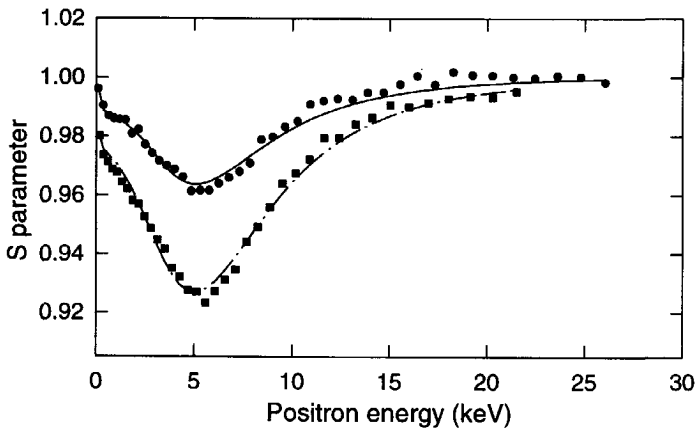

Figure 6.27: *S parameter versus positron energy for the* 5×10^{14} O^+/cm^2 *and* 2×10^{15} O^+/cm^2 *implanted samples after annealing at 800°C. The lines are the results of VEPFIT with 'model 3'.*

The agreement is good for all contributions except for the central part of the contribution of the surface and the bulk. Inspection of the two-detector Doppler broadening measurements which were used in the decomposition showed that the curve obtained with a positron implantation energy of 21 keV for the 2×10^{15} O^+/cm^2 implanted sample is slightly sharper than that of the 5×10^{14} O^+/cm^2 sample. This is surprising since at positron implantation energies of 21 keV one expects a large contribution from bulk Si, and this contribution should be independent of the sample. To avoid effects of the orientation of the samples we measured the samples along a known orientation and used that orientation for all samples. The measurements on oxygen implanted silicon were performed in batches over a one year period. It turned out that at the beginning of the investigations a different sample orientation was used than for the later mea-

surements [(110) versus (100)]. In section 6.1 it was shown that silicon has a large anisotropy and the projection for a (110) direction results in a sharp peak while the (100) direction has a plateau. In Doppler-broadening measurements the effects of the orientation are smaller than in ACAR measurements. The resolution is worse than that of an ACAR system and the Doppler broadened curve is obtained from contributions along all kinds of orientations due to the small sample-detector distance in a two-detector setup. However, a small effect of the orientation always remains. Nilen *et al.* [41] showed this effect for diamond. To maximise the effect, a setup with a sample-detector distance of 0.5 m was used. They found variations in the S value of 1 %. In our setup with a sample-detector distance of 4 cm the effect is much smaller. The expected effect, a sharper distribution for the (110) direction than for the (100) direction, is in agreement with our measurements. The difference in orientation does not affect the high momentum part of the distributions.

In figure 6.30 the ratio curves of the surface and the defect contribution are shown. The ratio curve for the defect contribution shows a peak with a shoulder at $\sim 17 \times 10^{-3}\ m_0c$, while the ratio curve for the surface contribution shows a peak at $10 \times 10^{-3}\ m_0c$ but drops below 1 around $15 \times 10^{-3}\ m_0c$. The decomposition confirms that the shoulder at $17 \times 10^{-3}\ m_0c$ is caused by the defect.

6.2.5 Conclusions

One and two-detector measurements have been performed for Si implanted with oxygen. A previous study [31] reported the formation of large V_xO_y clusters. In the present study two-detector measurements are used to identify the defect. The increased ratio to bulk Si at $17 \cdot 10^{-3}$ m_0c in the form of a shoulder on the peak at $10 \cdot 10^{-3}\ m_0c$ is connected with large V_xO_y clusters. A set of two-detector measurements at a number of positron energies is used to decompose the measured Doppler broadened spectra into separate contributions for the bulk, the surface and the defect. The decomposition confirms the presence of the shoulder. The decomposition technique can be used to obtain the Doppler broadened curves for defects. By using the method on two different samples we showed that the defect contribution is identical for both samples. These curves can be used to fingerprint defects. The ratio curves also show that the formation of large V_xO_y clusters starts already at 700°C in the oxygen-rich implantation region. In the 2 and 4×10^{17} O^+/cm^2 implanted samples annealed at 1350°C the same defects are identified as in the low dose implanted samples annealed at 800°C. The 1.7×10^{18} O^+/cm^2 sample is very different. In this sample a SiO_2 (BOX) layer is formed. After annealing at 1350°C the top layer of crystalline silicon is formed. This layer is characterised by a low S value although the electrical properties are similar to those of bulk Si. The defects in this layer can not be observed by TEM. The S-W plot and the two-detector Doppler broadening measurements indicate that

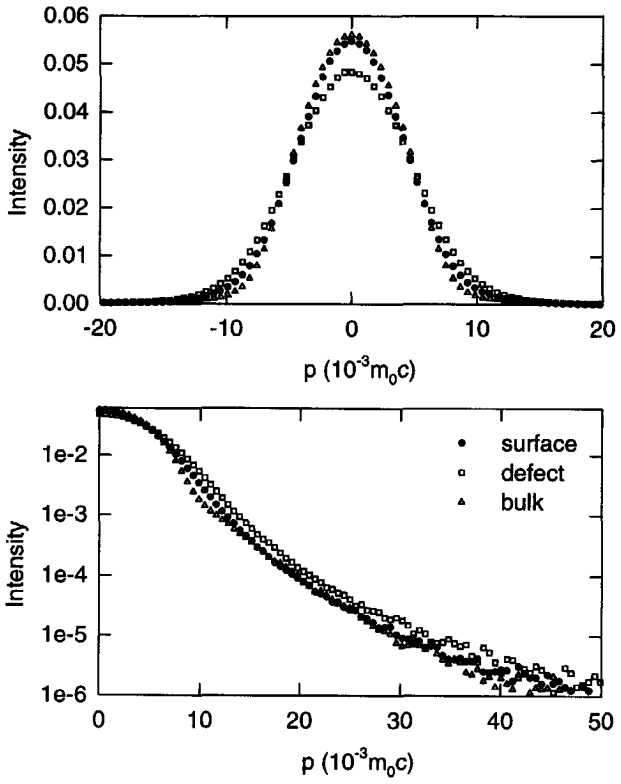

Figure 6.28: *Contributions of the surface, defect and bulk to the Doppler-broadened spectrum of the sample implanted with* $2 \times 10^{15}\ O^+/cm^2$.

also these defects are oxygen related.

6.3 Gallium Nitride

6.3.1 Introduction

GaN has attracted considerable attention in recent years due to its physical and electronic properties and, above all, its recently demonstrated qualities as a high-efficiency material for optical devices operating in the blue and ultraviolet (UV) regions of the optical spectrum [42, 43]. Despite this increased interest little is known about the nature of the intrinsic defects in GaN.

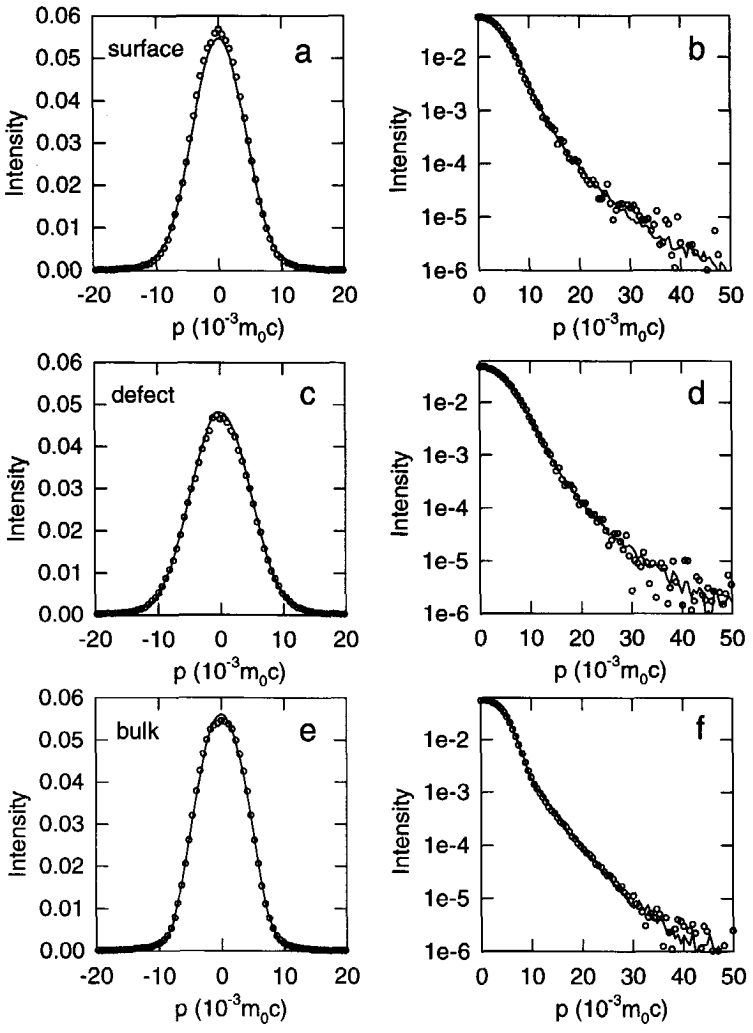

Figure 6.29: *Comparison of the calculated contributions of the surface (a, b), defect (c, d) and bulk (e, f) derived from the Doppler-broadening spectra of the samples implanted with* 5×10^{14} O^+/cm^2 *(open circles) and* 2×10^{15} O^+/cm^2 *(line).*

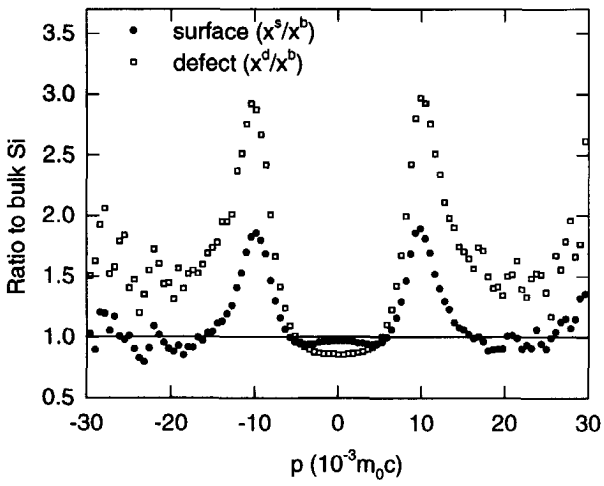

Figure 6.30: *Ratio curves of the defect and the surface contribution to bulk Si.*

As-grown samples of GaN are typically heavily autodoped n-type with carrier concentrations as high as 10^{20} cm^{-3}. This intrinsic autodoping has long been associated with the N-vacancy [44–46]. However, recent ab initio calculations seem to rule out this vacancy as the source of the autodoping [47] and generally predict a much lower formation energy for the Ga-vacancy in the n-type case than for any other point defect, including the N-vacancy [47, 48].

While there have been many theoretical investigations into the nature of the intrinsic defects, little experimental work has been done. However, all the experimental data so far either directly or indirectly point towards autodoping by N-vacancies [49, 50]. It should be noted that none of the experimental studies so far have been able to establish the nature of the autodoping conclusively. We hope to obtain more information about the nature of the defects by performing Doppler broadening measurements. The two-detector Doppler broadening setup was used to obtain information about the chemical surroundings of the annihilation site, while measurements with mono-energetic positrons were used to obtain information on the depth distribution of the defects.

6.3.2 Experimental

The measurements were performed on three different GaN samples, an autodoped n-type, a Mg-doped p-type and a semi-insulating (SI) sample. The samples were grown by the ECR-MBE method on sapphire substrates [51]. The autodoped n-type sample has a thickness of 1.28 μm with a buffer layer of about 30 nm grown at 550°C. The rest of the sample was grown at 800°C. The GaN layer has a carrier concentration of 2×10^{18} cm^{-3} and an electron mobility of 80 cm^{2}V^{-1}s^{-1}. The semi-insulating sample (SI) has a thickness of 1.38 μm with a buffer layer of about 30 nm grown at 600°C. In this case the rest of the film was grown at 900°C. The p-type sample is 1.09 μm thick with a slight Mg doping and a resistivity of 6×10^3 Ωcm. The samples were grown at a slight N_2 overpressure.

6.3.3 Experiments

One-detector measurements

The results of the Doppler broadening measurements are shown in figure 6.31. All reported S and W values are relative to the values of semi-insulating GaN, respectively. The figure displays a striking difference between the results for the semi-insulating and p-type samples on one hand and the autodoped n-type on the other. The increase in the S parameter of about 4 % for the n-type in comparison to the semi-insulating and p-type samples is typical of vacancy-type defects in compound semiconductors such as GaAs and strongly implies the presence of such defects in the autodoped n-type sample. This is further confirmed by the decrease in the W value for the same sample. The Doppler broadening data was analysed using the VEPFIT program and the fits are shown as solid lines in figures 6.31 and 6.32. Figure 6.32 shows the trajectory traversed in the S-W plane for the cases of the n-type and semi-insulating samples using the positron energy as a running parameter. The large open circles show the fitted values for each layer. The plot illustrates how the positrons first probe the surface, then the GaN layer and finally just begin to probe the Al_2O_3. Note also that for the case of the n-type there is an interface layer between the GaN and sapphire layers with a high S value and a low W. The effect of the interface in the S-E curve is an increase in the S value between 10 and 17 keV before the curve begins to go down to the S value of sapphire (estimated at 0.92 S_{SI-GaN}). The interface layer is quite thin, but it acts as a very efficient trap for positrons. Positrons implanted with an energy of 15 keV have a broad implantation profile and a large fraction of the implanted positrons annihilates in the interface layer. The high S value indicates the presence of vacancy-clusters or microvoids in this interface layer. The trajectory for the p-type sample is not shown in figure 6.32 since it would essentially run on top of the SI trajectory, as can be seen from figure 6.31.

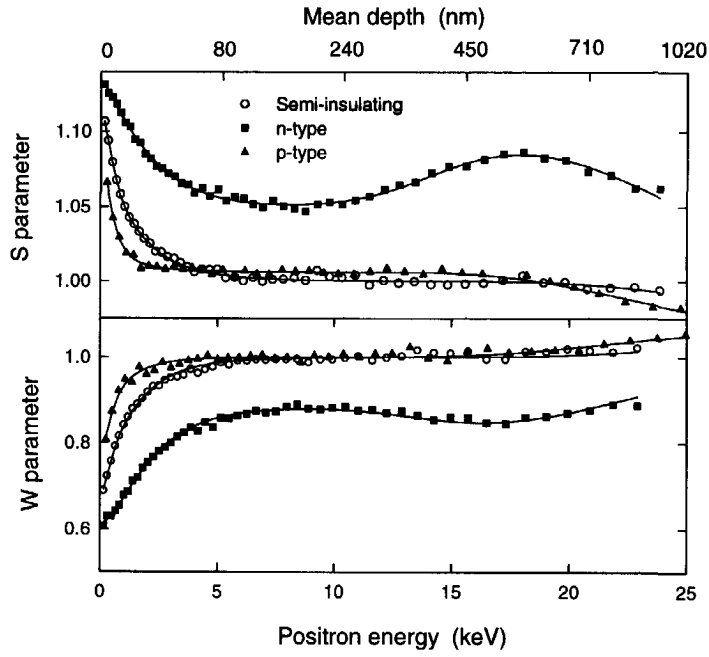

Figure 6.31: *S and W parameters as a function of incident positron energy for the three GaN samples studied. The curves are fitted values obtained from the VEPFIT fitting program.*

Two detector measurements

Figure 6.33a shows the result of the two-detector measurements at an incident positron energy of 7 keV for the semi-insulating sample and the autodoped n-type sample. This energy was chosen because it yields a maximum fraction of the incident positrons annihilating in the GaN layer (see figure 6.31.) For low-energy positron implantations (below 5 keV) a large fraction of the positron annihilates at the surface; for energies above 10 keV a part of the positrons annihilate at the interface layer. Figure 6.33b shows the calculated momentum distribution for defect-free GaN as well as for GaN with N vacancies, GaN-V_N, and Ga vacancies, GaN-V_{Ga}. For comparison the calculated curve for defect-free GaN is also shown in figure 6.33a.

The atomic superposition method described in chapter 2 was used to calculate the high momentum part of the Doppler broadening distribution. The generalised gradient approximation was applied in the calculations. The use of electron wavefunctions of free atoms in the atomic

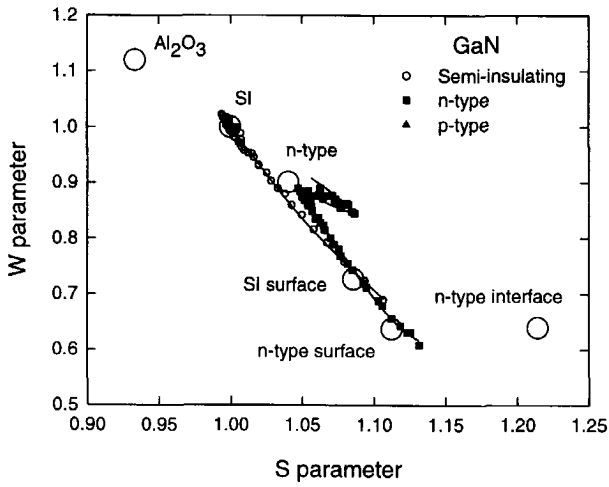

Figure 6.32: *S-W plot for the autodoped n-type and semi-insulating GaN samples showing the probing of different layers. The curves are fitted values obtained from the VEPFIT fitting program.*

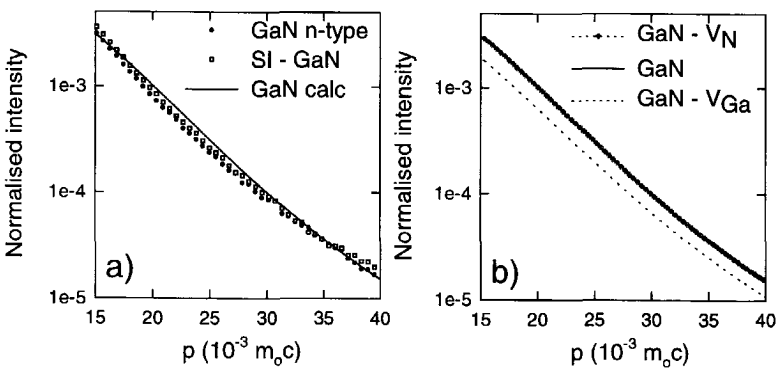

Figure 6.33: *a) Result of the two-detector coincidence measurements. At* 40×10^{-3} m_0c *there were 100-200 counts per point, making the difference between the two measurements statistically significant. b) Results of calculations of positron annihilation with core electrons for defect-free GaN as well as at N-vacancies and Ga-vacancies in GaN. Note that the calculated profiles for defect-free GaN and GaN-*V_N *are virtually identical. All experimental curves are normalised to unit area. The calculated curves are scaled to* $\sum_{j=core} \lambda_j / \sum_{j=all} \lambda_j$.

superposition program is not valid for valence electrons, so only core electrons are included in the calculation of the momentum distribution. The restriction to core electrons makes it impossible to calculate accurately the momentum distribution between 0 and $20 \times 10^{-3}\ m_0c$ since in that interval the contribution of valence electrons to the momentum distribution dominates the contribution of core electrons.

The calculation was done for $90 \times 90 \times 90$ node points using a supercell of 64 atoms for perfect GaN and 63 atoms for GaN with a vacancy defect. Atomic relaxation is not taken into account. The calculated distribution is convoluted with a gaussian with a FWHM of 0.93 keV to account for the experimental resolution. All Ga electrons up to and including *3d* are included in the calculation. Alatalo *et al.* [36] showed that, although the *3d* electrons of Ga cannot be considered as core electrons, the calculated Doppler broadened spectra show the same trends as the experimental spectra when the *d* electrons are included.

6.3.4 Discussion

The observed increase in the S parameter value of 4 % and the accompanied decrease in the W parameter are clear evidence of the presence of vacancy-type defects. In GaAs increases in the S parameter of 2-3 % have been associated with the presence of mono-vacancies and increases of 4-5% with di-vacancies [4]. The two-detector measurement on SI-GaN showed good agreement with the calculated momentum distribution for defect-free GaN. The calculated momentum distributions showed very little difference between defect-free GaN and GaN with N vacancies (GaN-V_N). This is an indication that it is difficult to observe such vacancies with positron annihilation techniques. A further indication of this can be obtained by calculating the positron lifetimes involved. The calculated lifetime for defect-free wurtzite GaN is 168 ps which is in good agreement with the experimental result of 170±10 ps [52]. The presence of a N vacancy only slightly increases the lifetime to 170 ps. Ga vacancies on the other hand show an increase of over 30 ps in the lifetime and a clear difference in the momentum distribution. It is not possible to perform conventional lifetime measurements to compare with the calculated lifetimes since this is a bulk method and the GaN layer was only $\sim 1\ \mu$m thick. It is unlikely that positrons trap at N vacancies as can be seen by the virtually identical high momentum distributions and the small increase in the lifetime. Also, recent ab initio calculations predict a positively charged state of the N vacancy [47, 48], thus making it not a trapping site for positrons. Therefore it is unlikely that the observed change in the momentum distribution is caused by N vacancies. Ga vacancies are more likely, although the calculated Doppler curve predicts a bigger difference between the defect-free material and the Ga vacancy. The discrepancy between the calculated Doppler spectrum of a Ga vacancy and the experimental spectrum of n-type GaN can be caused by relaxation of atoms around the defect site or the formation of defect complexes. Another

explanation for the discrepancy between the calculated and experimental curve is that at 7 keV not all the positrons annihilate in the n-type GaN layer. In figure 6.32 we can see that the S-W curve does not reach the S-W point for n-type GaN. The measured Doppler broadening curve at 7 keV contains also contributions of annihilations in the interface layer and at the surface.

6.3.5 Conclusions

Positron beam experiments have been performed on autodoped n-type, semi-insulating and Mg doped p-type GaN. The results from Doppler broadening yield clear evidence of the presence of vacancy-type defects in the autodoped n-type sample compared to the other two samples. Calculations and charge state considerations exclude that the observed vacancies are of the N vacancy type. Core-electron-sensitive two-detector measurements show that the most likely candidate for these vacancies is the Ga vacancy, although vacancy complexes or di-vacancies can not be ruled out.

References

[1] S. Dannefaer, *Phys. Status Solidi A* **102** (1987) 481.

[2] P. Ashoka-Kumar, K.G. Lynn and D.O. Welch, *J. Appl. Phys.* **76** (1994) 4935.

[3] R. Ambigapathy, A.A. Manuel, P. Hautojärvi, K. Saarinen and C. Corbel, *Phys. Rev. B* **50** (1994) 2188.

[4] P. Hautojärvi, *J. de Physique IV* (1995) C1-3.

[5] J. Mäkinen, C. Corbel, P. Hautojärvi, P. Moser and F. Pierre, *Phys. Rev. B* **39** (1989) 10162.

[6] A. Kawasuso, M. Hasegawa, M. Suezawa, S. Yamaguchi and K. Sumino, *Appl. Surf. Sci.* **85** 280.

[7] V. Avalos and S. Dannefaer, *Phys. Rev. B* **54** 1724.

[8] M. J. Puska, C. Corbel and R.M. Nieminen, *Phys. Rev. B* **41** (1990) 9980.

[9] J.W. Corbett, Point Defects in Solids, vol. 2, Semiconductors and Molecular Crystals, (Plenum Press, New York 1975).

[10] R. Harthoorn and P.E. Mijnarends, *J. Phys.* F **8** (1978) 1147.

[11] T. Chiba and T. Akahane, in *Positron Annihilation*, eds: L. Dorikens-Vanpraet, M. Dorikens and D. Segers (World Scientific, Singapore 1989) 674.

[12] M. Saito, A. Oshiyama and S. Tanigawa, *Phys. Rev. B* **44** (1991) 10601.

[13] P. Mascher, S. Dannefear and D. Kerr, *Phys. Rev. B* **40** (1989) 11764.

[14] M. Hasegawa, T. Chiba, A. Kawasuso, T. Akahane, M. Suezawa, S. Yamaguchi and K. Sumino, *Mater. Sci. Forum* **196-201** (1995) 1481.

[15] A. van Veen, H. Schut, J. de Vries, R.A. Hakvoort and M.R. IJpma, *AIP Conf. Proc. No. 218* (AIP, New York, 1990) p. 171.

[16] A. Kawasuso, M. Hasegawa, M. Suezawa, S. Yamaguchi and K. Sumino, *Mater. Sci. Forum* **175-178** (1995) 423.

[17] M.J. Puska and R.M. Nieminen, *Rev. Mod. Phys.* **66** (1994) 841.

[18] E. Soininen, H. Huomo, P.A. Huttunen, J. Mäkinen, A. Vehanen and P. Hautojärvi, *Phys. Rev. B* **41** (1989) 6627.

[19] J. Mäkinen, C. Corbel, P. Hautojärvi and D. Mathiot, *Phys. Rev. B* **42** (1990) 1750.

[20] J. Mäkinen, C. Corbel, P. Hautojärvi and D. Mathiot, *Phys. Rev. B* **43** (1991) 12114.

[21] E. Soininen, J. Mäkinen, D. Beyer and P. Hautojärvi, *Phys. Rev. B* **46** (1992) 13104.

[22] H. Schut, *A Variable Energy Positron Beam Facility with Applications in Material Science*, PhD dissertation, Delft University of Technology, Delft (1990).

[23] W. Bauer-Kugelmann, J.A. Duffy, J. Störmer, G. Kögel and W. Triftshäuser, *Appl. Surf. Sci.* **116** (1997) 231.

[24] B. Nielsen, O.W. Holland, T.C. Leung and K.G. Lynn, *J. Appl. Phys.* **74** (1993) 1636.

[25] T.E. Jackman, G.C. Aers, M.W. Denhoff and P.J. Schultz, *Appl. Phys. A* **49** (1989) 335.

[26] J. Mäkinen, P. Hautojärvi and C. Corbel, *J. Phys.: Cond. Mat.* **4** (1992) 5137.

[27] A.G. Revesz and H.L. Hughes, *Microelec. Eng.* **36** (1997) 343.

[28] A. Ikari, H. Haga, A. Uedono, Y. Ujihira and O. Yoda, *Jpn. J. Appl. Phys.* **33** (1994) 1723.

[29] A. Uedono, Y.K. Cho, S. Tanigawa and A. Ikari, *Jpn. J. Appl. Phys.* **33** (1994) 1.

[30] S. Dannefaer and D. Kerr, *J. Appl. Phys.* **60** (1986) 1313.

[31] M. Fujinami, *Phys. Rev. B* **53** (1996) 13047.

[32] M. Fujinami, *Mater. Sci. Forum* **255-257** (1997) 218.

[33] J.P. Biersack and L.G. Haggmark, *Nuc. Inst. Meth.* **174** (1980) 257.

[34] B. Nielsen, O.W. Holland, T.C. Leung and K.G. Lynn, *J. Appl. Phys.* **74** (1993) 1636.

[35] P.G. Coleman, N.B. Chilton and J.A. Baker, *J. Phys. Condens. Matter* **2** (1990) 9355.

[36] M. Alatalo, B. Barbiellini, M. Hakala, H. Kauppinen, T. Korhone, M.J. Puska, K. Saarinen, P. Hautojärvi and R.M. Nieminen, *Phys. Rev. B* **54** (1996) 2397.

[37] P. Asoka-Kumar, M. Alatalo, V.J. Ghosh, A.C. Kruseman, B. Nielsen and K.G. Lynn, *Phys. Rev. Let.* **77** (1996) 2097.

[38] M. Clement, J.M.M. de Nijs, H.Schut, A. van Veen and P. Balk, *J. Appl. Phys* **79** (1996) 9029.

[39] J.P. Peng, K.G. Lynn, P. Asoka-Kumar, D.P. Becker and D.R. Harshman, *Phys. Rev. Lett.* **76** (1996) 2157.

[40] A.C. Kruseman, H. Schut, M. Fujinami and A. van Veen, *Mater. Sci. Forum* **255-257** (1997) 793.

[41] R.W.N. Nilen, S.H. Connell, W.G. Schmidt, D.T. Britton, W.S. Verwoerd, J.P.F. Sellschop and S. Shrivastava, *Appl. Surf. Sci.* **116** (1997) 330.

[42] S. Nakamura, M. Senoh, N. Iwasa and S. Nagahama, *Appl. Phys. Lett.* **67** (1995) 1868.

[43] S. Nakamura, M. Senoh, S. Nagahama, N. Iwasa, T. Yamada, T. Matsushita, H. Kiyoku, and Y. Sugimoto, *Jpn. J. Appl. Phys.* **35** (1996) L74.

[44] H. P. Maruska and J. J. Tietjen, *Appl. Phys. Lett.* **15** (1969) 327.

[45] D. W. Jenkins and J. D. Dow, *Phys. Rev. B* **39** (1989) 3317.

[46] P. Bogusławski, E.L. Briggs and J. Bernholc, *Phys. Rev. B* **51** (1995) 17255.

[47] J. Neugebauer and C.G. van de Walle, *Phys. Rev. B* **50** (1994) 8067.

[48] T. Mattila and R.M. Nieminen, *Phys. Rev. B* **55** (1997) 9571.

[49] P. Perlin, T. Suski, H. Teisseyre, M. Leszczynski, I. Grzegory, J. Jun, S. Porowski. P. Bogusławski, J. Bernholc, J. C. Chervin, A. Polian and T. D. Moustakas, *Phys. Rev. Lett.* **75** (1995) 296.

[50] T. L. Tansley and R. J. Egan, *Phys. Rev.* **B 45** (1992) 10942.

[51] T.D. Moustakas and R.J. Molnar, *Mat. Res. Soc. Proc. Vol.* **281** (1993) 753.

[52] S. Dannefaer, W. Puff and D. Kerr, *Phys. Rev. B* **55** (1997) 2182.

Chapter 7

Calcium sulphate

7.1 Introduction

Calcium sulphate occurs in nature in different forms of hydration ($CaSO_4 \cdot n\ H_2O$, with $n \leq 2$). The material is best known however in its hemihydrate form ($n = 0.5$) which is a very important material in the building industry where it is used in the manufacture of plaster and plasterboard. Table 7.1 gives an overview of the most common forms. The literature is not clear about the precise number of forms of subhydrate ($n < 2$) and their structure. A schematic representation of the structures is shown in figure 7.1. The main characteristics of the structures are as follows: gypsum has a layered structure of calcium sulphate and water, hemihydrate and soluble anhydrite have a tunnel structure and insoluble anhydrite has a rather densely packed structure. In the hemihydrate one-half of all tunnel positions are occupied by water molecules while in the soluble anhydrite all positions are empty.

Table 7.1: *The most common forms of calcium sulphate.*

	Formula	Structure	Density (g/cm^3)
gypsum	$CaSO_4 \cdot 2.0\ H_2O$	monoclinic [1]	2.31
hemihydrate or bassanite	$CaSO_4 \cdot 0.5\ H_2O$	monoclinic [2]	2.74
soluble anhydrite	γ-$CaSO_4$	hexagonal [2]	
insoluble anhydrite	β-$CaSO_4$	orthorhombic	2.95

A considerable amount of literature has been devoted to the hemihydrate forms of calcium sulphate. Different techniques have been used to investigate the phase changes due to the dehydration but the literature is not conclusive about the number of subhydrate phases, their structure and the temperatures at which the phase transitions take place. It is known that the dehydration of gypsum proceeds through formation and growth of nuclei [3] and that the conversion rate is strongly temperature dependent [4, 5]. The conversion of gypsum to hemihydrate starts above

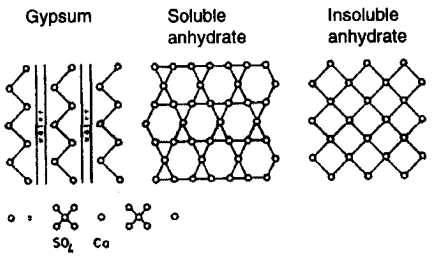

Figure 7.1: *The schematic structure of gypsum, soluble anhydrite and insoluble anhydrite. The open circles represent a chain of Ca^{2+} and SO_4^{2-} ions perpendicular to the plane of the paper (from Abriel et al. [6]).*

60°C [4, 6]. Between 100°-110°C [6] further loss of water results in the metastable γ-$CaSO_4$ (soluble anhydrite). This dehydration step is not accompanied by a basic change of the structure. Water molecules can leave and reoccupy their sites relatively easily (see figure 7.2). When the temperature is lowered, γ-$CaSO_4$ will rapidly rehydrate to hemihydrate under atmospheric conditions (10^5 Pa, RT, 50 % humidity). Gay [5] noticed that the dehydration temperatures depend on the particular sample, the sample history and the humidity. Both the dehydration and the rehydration temperature decrease considerably, up to 10°C, after a dehydration-rehydration cycle. Although the existence of the $CaSO_4 \cdot 0.5\ H_2O$ form is generally accepted the views about its structure still differ. Other subhydrate forms of $CaSO_4 \cdot n\ H_2O$ have been proposed with $n = 0.67$ [7], $n = 0.74$ [6] and $n = 0.80$ [8]; on the other hand Langer *et al.* [2] exclude the existence of $n > 0.5$.

Further heating of γ-$CaSO_4$ results in the formation of β-$CaSO_4$. Also the temperature for the conversion of γ-$CaSO_4$ to β-$CaSO_4$ is not well established. According to Gay [9] the conversion starts already at 150°C, although prolonged exposures to high temperatures (8 hours at 900°C) are necessary to convert all γ-$CaSO_4$ to β-$CaSO_4$. According to Abriel *et al.* [6] the formation of β-$CaSO_4$ starts at 250°C. In the densely packed structure of β-$CaSO_4$ there is no room for water molecules and β-$CaSO_4$ does not rehydrate, in contrast to γ-$CaSO_4$.

Very little positron annihilation work has been done on calcium sulphate, and the work that has been done is limited to lifetime and Doppler-broadening measurements [10–12]. In our present study the two-dimensional angular correlation of annihilation radiation (2D-ACAR) technique is used. We hope to see effects in our positron annihilation measurements caused by phase transitions or by the water loss due to dehydration. Positron annihilation techniques are very sensitive to open volumes. If the open volume is large enough, positronium formation is possi-

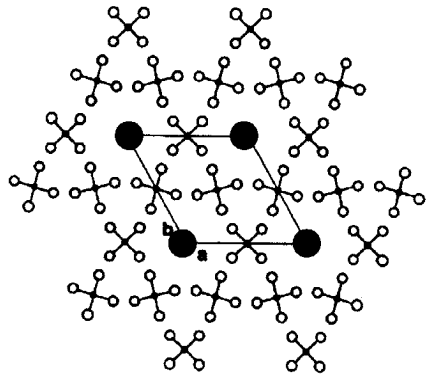

Figure 7.2: *Structure of hemihydrate and soluble anhydrite. The black dots connected to the four open circles represent the SO_4 groups. Together with the Ca groups they form chains perpendicular to the plane of the paper. The big gray dots represent possible positions for water molecules or for the formation of positronium (from Lager et. al. [2]).*

ble (positronium has a diameter of 1.06 Å). In 2D-ACAR measurements the presence of p-Ps, the singlet state of positronium, is clearly visible in the form of a very sharp peak at 0 mrad. The removal of the crystal water will open up channels with a diameter of 5.3 Å, which is large enough to allow the formation of positronium.

7.2 Experimental

Two single crystals of gypsum ($CaSO_4 \cdot 2\ H_2O$) were available, one of initial mass 86.00 $\pm$ 0.03 mg ($7 \times 5 \times 1$ mm) and one thinner piece of 19.05 $\pm$ 0.03 mg ($8 \times 6 \times 0.2$ mm). Both pieces were transparent. The loss of crystal water can be determined from the loss of mass. Gypsum ($CaSO_4 \cdot 2\ H_2O$) has a molecular weight of 172.173 while anhydrite ($CaSO_4$) has a molecular weight of 136.142, a difference of over 20%.

The sample with a thickness of 1 mm was used for the 2D-ACAR measurements. In 0.5 mm of $CaSO_4 \cdot 2.0\ H_2O$ over 99 % of the positrons are stopped. The measurements were performed at room temperature. One of the edges of the sample was aligned to be in line with both detectors. This alignment was repeated for all measurements to ensure an identical mounting for all measurements. Figure 7.3 shows a cross-section of the measured distribution compared to quartz and high-density polyethylene (HDPE). In the quartz distribution a very sharp positronium peak is present. The peak in the polyethylene distribution is broader than that of quartz.

The distribution of gypsum does not show a clear indication of a peak.

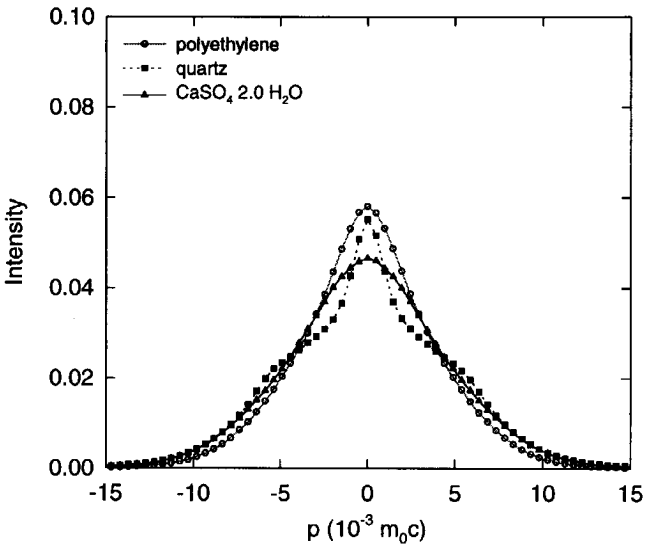

Figure 7.3: *Cross-sections of 2D-ACAR distributions for quartz, polyethylene (HDPE) and* $CaSO_4 \cdot 2.0\, H_2O$. *All curves are normalised to equal area.*

Both samples were placed in a tube which itself was placed in boiling water for the first heat treatment. The inside of the tube reached a temperature of 100°C. The tube was sealed with paper to avoid that water droplets reach the sample. Three separate heatings of 5, 7 and 20 minutes were performed. After each heating the sample was weighed. No water loss was detected. It is possible however that a part of the water was removed and that the sample rehydrated in the time between the end of the heating and the start of the weighing. The sample handling was done in less than one minute.

In the second heating session a furnace was used. This made it possible to change the temperature. No water loss was detected, neither after heating at 90°C for 20 minutes nor after heating at 100°C for 10 minutes. After heating for 5 minutes at 115°C the edges of the sample became white but the central part of the sample was still transparent. After heating for 10 minutes at 110-120°C a loss of mass of 3.5 mg was measured. The entire outside of the sample was white. After one night under atmospheric conditions the loss of mass was reduced to 3.2 mg, indicating that the sample was partially hydrated again. The outside of the sample remained white during

Table 7.2: Overview of the cumulative heat treatments of the calcium sulphate sample. The percentage of the net loss of mass is based on the mass before the specified heat treatment and at least 12 hours afterwards. The molecular weight is the estimated molecular weight after heating.

Session	Treatment	Initial mass (mg)	Net loss of mass (%)	Molecular weight
1	5 minutes at 100°C	86.00	0.0	172.17
	7 minutes at 100°C	86.00	0.0	172.17
	20 minutes at 100°C	86.00	0.0	172.17
2	20 minutes at 90°C	86.00	0.0	172.17
	10 minutes at 100°C	86.00	0.0	172.17
	10 minutes at 115°C	86.00	3.7	165.77
3	10 minutes at 115°C	80.10	2.5	161.62
4	10 minutes at 115°C	78.04	2.4	157.76
5	10 minutes at 115°C	73.12	3.4	152.39
6	120 minutes at 190°C	41.65	2.6	

this hydration. After a second day the loss of mass was still 3.2 mg. This is equivalent to 3.7% of the initial mass, i.e. to 0.35 H_2O. Figure 7.4 shows the cross-section of the ACAR distribution of $CaSO_4 \cdot 1.6\ H_2O$. The distribution is clearly peaked, indicating the formation of positronium.

The third heating session was performed under the same conditions as the last heat treatment of session # 2. After removing the mounting for the 2D-ACAR measurement (which resulted in the loss of a small part of the back of the sample), the mass of the sample was 80.10 mg. Directly after the heat treatment a loss of mass of 3.6 mg was measured. After one night under atmospheric conditions this was reduced to 2.0 mg. A fourth heating session was performed and the weight was measured several times during the day. Immediately after the heat treatment a rapid rehydration occurred as can be seen in table 7.3. Within 5 minutes the initial loss of mass of 3.9 mg was reduced to 2.9 mg. In an hour the loss of mass was reduced to only 1.9 mg. After 100 minutes the mass became stable and no further gain in mass was measured.

During the third and fourth heating session the sample lost 3.9 mg or 4.9 % in mass. The molecular weight was estimated at 157.76 which corresponds to $CaSO_4 \cdot 1.2\ H_2O$. A 2D-ACAR measurement was performed to investigate the effects of the water loss. The distribution of the $CaSO_4 \cdot 1.2\ H_2O$ sample is even more peaked than the $CaSO_4 \cdot 1.6\ H_2O$ measurement (see figure 7.4), which indicates a larger fraction of p-Ps.

Table 7.3: Gain in mass after the fourth heating session. The mass before the heat treatment was 78.0 mg.

Time (min)	mass (mg)
0	74.18
	74.65
	74.77
	75.00
	75.06
5	75.14
10	75.42
30	76.00
60	76.18
100	76.25
150	76.23
200	76.20
250	76.23

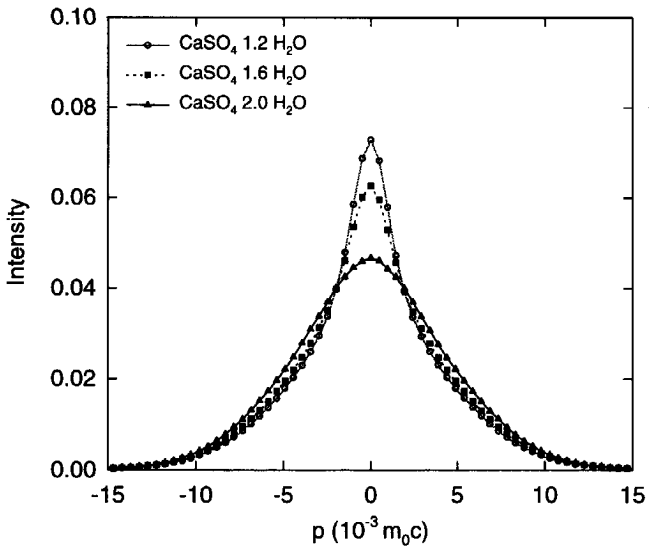

Figure 7.4: *Cross-sections of 2D-ACAR distributions for $CaSO_4 \cdot 2\,H_2O$, $CaSO_4 \cdot 1.6\,H_2O$ and $CaSO_4 \cdot 1.2\,H_2O$. All curves are normalised to equal areas.*

During the measurement of $CaSO_4 \cdot 1.2\ H_2O$ a difference was noticed between the first measurement (0-30,000 s) and the later measurements (30,000-300,000 s). The height of the peak in the distribution of the first measurement was considerably lower than in the other measurements. Although no permanent loss of water was measured in vacuum during a test with the thin gypsum sample, a temporary loss of water is still possible. To examine this the vacuum chamber was pressurised again. After one day under atmospheric conditions a new measurement was started in vacuum. A shorter measuring time of 10,000 s was used instead of 30,000 s to observe changes with time. Figure 7.5 shows the cross-section of these measurements. During the first 30,000 s the p-Ps peak became more pronounced. After 50,000 s no differences between the measurements were noticed. The water loss was confirmed by weighing the sample just after removal from the vacuum chamber and again 30 minutes later. The mass increased by 1.3 mg. The water content in vacuum is lower than one would expect based on the molecular weight under atmospheric conditions. The dehydration-rehydration effect is reversible. A new measurement showed the same behaviour after pressurising and evacuating the vacuum chamber.

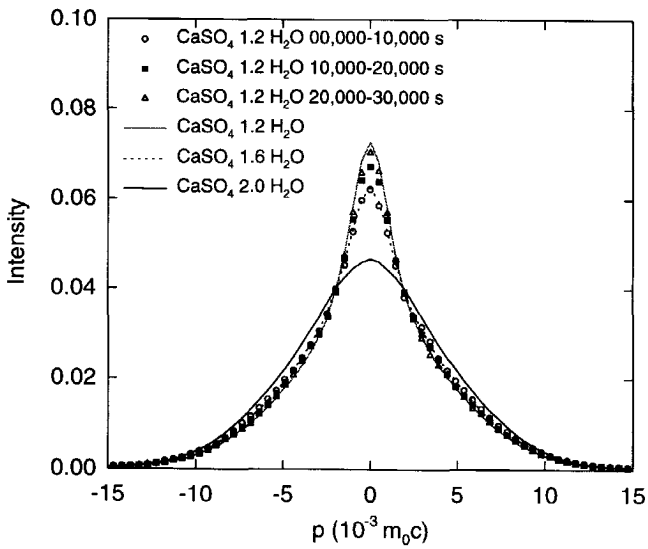

Figure 7.5: *Cross-sections of 2D-ACAR distributions for $CaSO_4 \cdot 1.2\ H_2O$ as a function of measuring time. For comparison the cross-sections of $CaSO_4 \cdot 2\ H_2O$, $CaSO_4 \cdot 1.6\ H_2O$ and $CaSO_4 \cdot 1.2\ H_2O$ are also shown. These last curves represent the combined measurements between 0 and 300,000 s.*

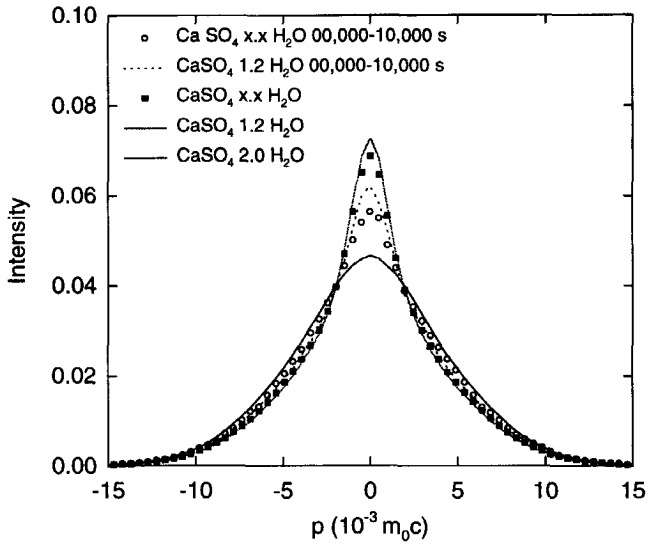

Figure 7.6: *Cross-sections of 2D-ACAR distributions for one piece of the $CaSO_4$ sample after the fifth heating session (curves marked with $CaSO_4 \cdot x.x\ H_2O$).*

A fifth heating session was performed under conditions identical to those of the third and fourth heating. After removing the mounting the mass of the samples was 73.12 mg. Initially 4.9 mg water was lost. After 30 minutes the sample gained 2.1 mg and after 14 hours the total gain was 2.4 mg; thus the net water loss was 2.5 mg. The molecular weight was 152.39, corresponding to $CaSO_4 \cdot 0.9\ H_2O$. During the handling of the sample after this heating the sample split parallel to the surface in two pieces. Troev *et al.* [12] mention separation of the crystal layers if the temperature is not increased slowly enough. In our measurements their criterion of 1 K min^{-1} was not met. No further splitting of the layers was observed in the two pieces.

The inner surfaces of both pieces were completely white with the exception of one spot, 0.5 × 1.5 mm in size, which was still transparent. Since the density of the gypsum spot is lower than that of the surrounding hemihydrate the splitting of the sample was probably caused by stress in the sample. The two pieces had a mass of 28.95 and 41.65 mg, respectively. The sample of 41.65 mg is 0.5 mm thick. This is still sufficiently thick to perform an ACAR measurement. The fact that the inner part of the sample is still partially transparent indicates that the water loss is not homogeneous. The outside of the sample has lost more water than the inside.

The inhomogeneity of the water content was confirmed by the ACAR measurement. The side

which previously was the inner part of the sample was directly exposed to the positrons. The height of the p-Ps peak is an indication of the water content of the sample. The ACAR distribution shows a p-Ps peak which is smaller than that observed in the previous measurement of $CaSO_4 \cdot 1.2\ H_2O$ (see figure 7.6). This indicates a higher water content, although the combination of the two parts of the sample should have a lower relative water content. The reason for this difference is the implantation profile of the positrons in the sample. The side of the sample directly exposed to the positrons contributes a large fraction of the overall momentum distribution. This side, which previously was the inner part of the sample, still has a high water content. Hence, it is not surprising that a higher 'effective' water content was measured and thus a lower p-Ps peak. An increase in the p-Ps peak was observed again during the first 30,000 s of the measurement.

Since the water content of the sample was not exactly known, the sample was heated at a temperature of 190°C during 2 hours. The hope was that during this heating all water would be removed. An initial loss of mass of 3.8 mg was measured (9% of the mass), which indicates a structure with at least 0.7 water molecules for each $CaSO_4$ before the heat treatment. Also this sample hydrated under atmospheric conditions. Before mounting, the net loss of mass was 1.1 mg. To monitor the changes in the distribution due to the loss of water in vacuum, ACAR measurements were performed with a measuring time of 10,000 s. The cross-section of the distribution obtained between 0-10,000 s is not significantly different from the distribution obtained for $CaSO_4 \cdot 1.2\ H_2O$ after the same time. The peak height after a prolonged time in vacuum was higher than the final peak of $CaSO_4 \cdot 1.2\ H_2O$, as can be seen in figure 7.7. A larger fraction of the sample was therefore hemihydrate. The hemihydrate dehydrates in vacuum and open volumes are created in which positronium formation is possible.

7.3 Discussion

The original sample contains only gypsum ($CaSO_4 \cdot 2\ H_2O$). During heating the sample begins to lose water, first from the outside layer and later also from the inside. The sample becomes a mixture of gypsum, hemihydrate and soluble anhydrite. Soluble anhydrite will rapidly rehydrate with atmospheric water to form hemihydrate. This rehydration can be observed as a gain in mass after the heat treatment.

During the first two sessions gypsum is partially converted to hemihydrate. Only a small gain in mass due to rehydration was measured after the heat treatment. During the third session a part of hemihydrate is converted to soluble anhydrite and all samples after this session contained at least 30 % γ-$CaSO_4$. After each heat treatment the increase in mass due to rehydration becomes larger, indicating a larger fraction of soluble anhydrite (see table 7.4). Although a gain in mass

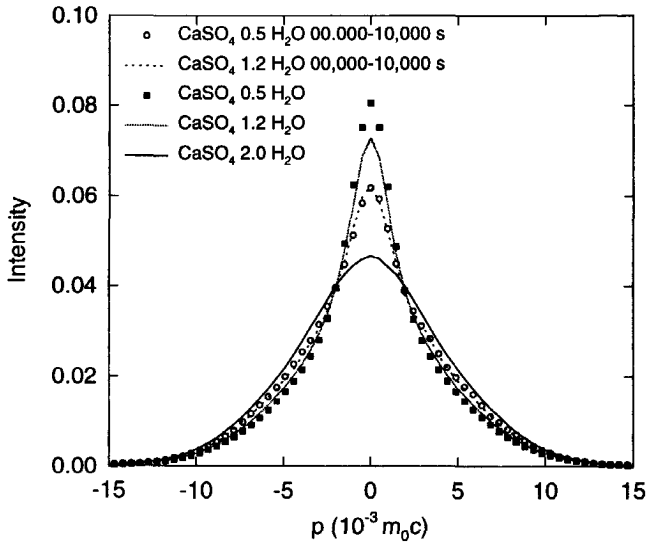

Figure 7.7: *Cross-sections of 2D-ACAR distributions for $CaSO_4$ after 2 hours heating at 190°C (marked $CaSO_4 \cdot 0.5\ H_2O$). For comparison the cross-sections of $CaSO_4 \cdot 2\ H_2O$ and $CaSO_4 \cdot 1.2\ H_2O$ are also shown.*

is measured after the heat treatment, all treatments resulted in a net loss of mass. This indicates that during all sessions gypsum was converted to hemihydrate. The presence of gypsum was confirmed during the fifth session in which the sample split in two parts. One part still contained a small spot of gypsum. In vacuum a large fraction of the rehydrated water is again removed. The concentration of open volumes then increases, which results in a higher fraction of positronium. Probably the mass just after the heat treatment is a good indication of the water content in vacuum. The problem is that the rehydration occurs very rapidly as can be seen in table 7.3. A slight delay in the weighing will result in an incorrectly measured loss of mass. To obtain well-defined numbers the water content is based on the mass determined under atmospheric conditions at least 12 hours after the heat treatment. This water content is an overestimate of the real water content in vacuum.

In the literature there is some discussion about the water content in the subhydrate form ($CaSO_4 \cdot n\ H_2O$). The annealing at 190°C for 2 hours should convert the entire sample to γ-$CaSO_4$. The temperature was not high enough to convert to β-$CaSO_4$ [6]. Under atmospheric conditions the γ-$CaSO_4$ rehydrates to hemihydrate. After the heat treatment the sample gained 7.0 % in mass. This corresponds to 0.53 water molecules which is in good agreement with values of 0.5 to 0.8

Table 7.4: Weight gain after heating. The percentage of γ-$CaSO_4$ is based on the assumption that the gain in mass is completely caused by the rehydration of γ-$CaSO_4$ to $CaSO_4 \cdot 0.5\ H_2O$. The gain in mass during sample handling is unknown. Thus, both the gain in mass and the γ-$CaSO_4$ percentage are underestimates.

Treatment	Weight gain (%)	Weight gain (H_2O)	Fraction of γ-$CaSO_4$ (%)
No treatment	0.0	0.00	0
115°C for 10 minutes	0.3	0.03	5
115°C for 20 minutes	2.0	0.18	$4 \cdot 10^1$
115°C for 30 minutes	2.6	0.23	$5 \cdot 10^1$
115°C for 40 minutes	3.3	0.28	$6 \cdot 10^1$
190°C for 120 minutes	7.0	0.53	$1.1 \cdot 10^2$

H_2O in subhydrates mentioned in the literature. The water content in our subhydrate may be higher since the gain in mass during sample handling is unknown. On the other hand a part of the water may be bound to the surface instead of in the γ-$CaSO_4$ channels. The p-Ps fraction for the γ-$CaSO_4$ sample was estimated at 25 % which indicates that a very large fraction of the positrons forms positronium.

A complication in the analysis is the inhomogeneous dehydration and the non-uniform probing of the sample by the positrons. The part of the sample probed by the positrons has a water content below average since the outside of the sample dehydrates first and a large fraction of the positrons annihilate in the toplayers of the sample. A rough indication of the water content of the sample is obtained by comparing the different cross-sections and the estimated percentage of γ-$CaSO_4$. No loss of mass is measured for $CaSO_4 \cdot 2.0\ H_2O$ after 1 day in vacuum. The angular correlation distribution of $CaSO_4 \cdot 1.6\ H_2O$ when placed in vacuum is identical to the angular correlation distribution of the first measurement of $CaSO_4 \cdot 1.2\ H_2O$. This last distribution is an average of the initial water content of ~ 1.2 molecule at 0 s and the unknown, but lower, water content after 10,000 s. The water content of the $CaSO_4 \cdot 1.6\ H_2O$ in vacuum is estimated at 1 molecule. Based on previous work [6] we can assume that after the heating at 190°C all $CaSO_4$ is hemihydrate or anhydrite. In vacuum all water is removed from the sample. The probed water content of the $CaSO_4 \cdot 1.2\ H_2O$ sample will be between 0 and 1. Table 7.5 shows the estimates of the water content in vacuum.

Our results are very different from the previous positron work on the dehydration of calcium sulphate [11, 12]. Troev *et al.* [11, 12] observed an increase in the o-Ps fraction in their lifetime measurements from 10 % to 20 % after heating at 50°C. At higher temperatures the o-Ps

Table 7.5: Water content under atmospheric conditions and estimates of the water content in vacuum.

Treatment	Atmospheric conditions	In vacuum
No treatment	$CaSO_4 \cdot 2.0\ H_2O$	$CaSO_4\ 2\ H_2O$
115°C for 10 minutes	$CaSO_4 \cdot 1.6\ H_2O$	$CaSO_4 \cdot 1\ H_2O$
115°C for 30 minutes	$CaSO_4 \cdot 1.2\ H_2O$	$CaSO_4 \cdot 1/2\ H_2O$
190°C for 120 minutes	$CaSO_4 \cdot 0.6\ H_2O$	$CaSO_4 \cdot 0\ H_2O$

remains at $\sim$ 20 %. In the present experiments we observe effects of dehydration only above 110°C and we notice a relation between the duration of the heat treatment, the water loss and the height of the p-Ps peak in the 2D-ACAR distribution. We do not see a saturation of the positronium formation which could explain the almost constant fraction of 20 % o-Ps observed by Troev *et al.* [11, 12]. Their measurements were performed under atmospheric conditions and at room temperature. This can partially explain the differences since the soluble anhydrite will hydrate to hemihydrate and obscure the effects of heating. The big difference in the temperature is harder to explain. Our temperature of 115°C is higher than the usually mentioned temperature of 100°C for the conversion of hemihydrate to soluble anhydrite; this can be ascribed to differences in the sample or the experimental conditions [5]. On the other hand, the literature seems to rule out loss of water at 50°C as mentioned by Troev *et al.* [11, 12].

7.4 Conclusions

A clear relation is shown between open volumes in calcium sulphate and the formation of p-Ps is established. The present measurements do not really allow a quantitative analysis due to the uncertainty in the water content in the layer probed by the positrons. Dehydration and rehydration of γ-$CaSO_4$ strongly affect the positron annihilation measurements due to the respective decrease (increase) of the concentrations of open volumes. A good understanding of these effects is important for a proper interpretation of the data.

References

[1] B.F. Pedersen and D. Semmingsen, *Acta Cryst. B* **38** (1982) 1074.

[2] G.A. Lager, Th. Armbruster, F.J. Rotella, J.D. Jorgensen and D.G. Hinks, *Am. Mineral.* **69** (1984) 910.

[3] J.E. Bright and M.J. Ridge, *Philos. Mag.* **6** (1961) 441.

[4] A. Puinis, B. Winkler and L. Fernandez-Diaz, *Mineral. Mag.* **54** (1990) 123.

[5] P. Gay, *Mineral. Mag.* **35** (1965) 354.

[6] W. Abriel, K. Reisdorf and J. Pannetier, *J. Solid State Chem.* **85** (1990) 23.

[7] N.N. Bushuev and V.M. Borisov, *Russ. J. Inor. Chem.* **27** (1982) 604.

[8] W. Abriel, *Z. Kristallogr.* **162** (1983) 1.

[9] P. Gay, *Mineral. Mag.* **35** (1965) 347.

[10] S.J. Tao, in *Positron Annihilation*, Proceedings of the 5th International Conference on Positron Annihilation, eds. R.R. Hasiguti and K. Fujiwara (Japan Institute of Metals, Aoba Arammaki, Sendai, 1979) p. 429.

[11] M. Dimanchev, A. Shofan, T. Troev and J. Serna, *Mater. Sci. Forum.* **105-110** (1992) 1545.

[12] T. Troev, M. Petkov, C. Alemany, J. Serna, *J. Mater. Sci.* **29** (1994) 865.

Chapter 8

Concluding remarks

The two new positron annihilation setups provide additional information compared to lifetime and single detector Doppler broadening measurements. This is shown by the experimental results described in this thesis. The 2D-ACAR system yields a two-dimensional distribution which contains information about annihilations predominantly with band electrons while the two-detector DBAR system yields spectra with a very low background which enables us to investigate the contribution of the core electrons. Thus the two setups provide complementary information.

The two-detector Doppler broadening technique in combination with calculations provides us with a tool to improve the identification of the atoms around the annihilation site. The high-momentum part of a Doppler broadening curve is determined by annihilations with core electrons. The shape of this contribution of the core electrons is almost unaffected by the surrounding atoms and can be used to identify the atom. The measurements of several metals show the potential use of the technique. The high-momentum parts of the Doppler broadening curves for Be, Ni, Mo and W are very different. As a result a unique fingerprint is obtained which can be used to identify different elements. In GaN the two-detector DBAR technique showed that n-type GaN contains vacancies on Ga positions. Although theoretical calculation predicted the V_{Ga}, its presence had not yet been experimentally determined. In SIMOX the technique was used to show that the top-layer of silicon contains defects which have a signature comparable with those of multivacancy-multioxygen defects. Although a DBAR curve often consists of contributions from different types of annihilation sites it is possible to obtain a fingerprint of one type by decomposing the low-background DBAR curve into separate contributions. An example of this decomposition was shown for silicon implanted with oxygen.

To obtain good statistics in the high-momentum part of a two-detector DBAR curve one has to measure for about ten hours. These long acquisition times make it interesting to construct a setup in which the high-intensity POSH beam is simultaneously used for ACAR measurements

and DBAR measurements. ACAR measurements also require long acquisition times and since they yield complementary information one would often like to perform both measurements. The ACAR detector spans only a small solid angle owing to the large sample-detector distance, so a large fraction of the annihilation photons is stopped in the shielding. Instead of stopping those photons one could also make two additional windows in the lead and use the photons for two-detector DBAR measurements.

The 2D-ACAR setup has proved its usefulness in the measurements of the highly-doped, electron irradiated silicon samples. While the two-detector Doppler broadening technique was not able to determine a unique fingerprint to distinguish between As-vacancy and Sb-vacancy complexes, the ACAR spectra showed a small but statistically significant difference between the Sb and the As doped samples.

The ACAR technique is also well suited to observe para-positronium. The annihilation of p-Ps yields a sharp peak at **p**=0. The open structure of soluble anhydrite ($CaSO_4 \cdot 0.5\ H_2O$) allows the formation of positronium. The effects of de- and rehydration are reflected in the fraction of positronium that is formed. Since the water loss is not uniform throughout the sample, a quantitative analysis was not yet possible. The combination of the ACAR setup and the high-intensity positron beam makes it possible to observe these effects as a function of depth and determine the diffusion behaviour of water in soluble anhydrite.

One of the advantages of the 2D-ACAR technique in comparison to the DBAR technique is its better resolution. Although our resolution at the present location is better than that of a DBAR setup ($1.7 \times 10^{-3}\ m_0c$ compared to $4.3 \times 10^{-3}\ m_0c$), it is not very good compared to other setups in the world owing to the maximum detector-detector distance of 10 m. Detector-detector distances up to 25 m are possible in the recently completed hall. This will improve the resolution component stemming from the detectors by a factor of 2.5. Furthermore, a smaller beam spot can be obtained by focusing of the POSH beam which also improves the resolution perpendicular to the beam direction. The resolution at the new location should be better than $1 \times 10^{-3}\ m_0c$ in both directions. A better resolution makes it easier to observe differences between measurements and thus improves the defect identification capabilities. It also makes it easier to distinguish the p-Ps component in the ACAR distribution from other annihilation modes, allowing a better determination of the p-Ps fraction and a better quantitative analysis than with the present resolution. Such an analysis yields for example the size of the void which is reflected in the width of the p-Ps peak. Thus, both setups provide a useful addition to the positron annihilation techniques available at the Interfaculty Reactor Institute and I expect a lot of interesting results.

Summary

For the characterisation of open-volume defects in solids a wide range of positron annihilation techniques can be applied. The positron lifetime and Doppler broadening of annihilation radiation techniques were already in use at the Interfaculty Reactor Institute at Delft University of Technology. This thesis describes the construction and the first results of two positron annihilation setups which are new to the institute. The first setup is a two-dimensional angular correlation of annihilation radiation system which yields a two-dimensional spectrum, whereas conventional techniques only yield a one-dimensional spectrum. The second setup is an extension of the Doppler broadening setup with a second detector in coincidence with the first one. As a result of the coincidence condition and the known relation between both energy shifts the background is three orders of magnitude lower than for a conventional single detector measurement. The measurement therefore allows us to investigate the high-momentum part of the Doppler broadening spectrum.

Chapter 1 gives a short introduction into the positron annihilation technique. Theoretical calculations of the spectra can be very helpful in the interpretation of the data. One of the methods for calculating spectra in the high-momentum region is the atomic superposition method. The theory behind this method is explained in chapter 2. The method uses some approximations which reduce the computational efforts but make the method less suited for calculating the contribution of the band electrons and thus the central part of the distribution. To validate the atomic superposition method the results were compared with more sophisticated calculations employing the Korringa-Kohn-Rostoker method of electronic structure calculation. The results were in good agreement between 20 and $45 \times 10^{-3}\ m_0c$, making the atomic superposition method a useful aid for the analysis of the high-momentum part of two-detector Doppler broadening curves.

Chapter 3 describes the experimental setup of the two newly built systems while chapter 4 explains the additional data handling necessary to correct the two-dimensional angular correlation spectra for the experimental conditions. In chapter 5 the results for six metals are reported. Especially aluminium was investigated thoroughly. Measurements on Al were performed at elevated temperatures. The S-W plot showed that above 450K mono-vacancies are created. The

curve in the S-W plot shows an almost linear relation between S and W for temperatures between 450K and 740K indicating that annihilations only occur at one type of defect sites, i.e. mono-vacancies. At 740K the curve strongly deviates which is probably related to the formation of divacancies. The atomic superposition method was used to calculate the high-momentum part of the Doppler broadening spectrum at room temperature and at 670K. The calculated curves were in good agreement with the experimental data. A second material investigated was Cu. The agreement between the experimental spectrum and the calculated distribution for Cu was not good. This discrepancy is ascribed to the limitations in the approximation used for the multi-particle interactions. Although the quantitative results are not satisfying for all cases, the qualitative results of the calculations are good as is shown by the comparison of the results for Be, Ni, Mo and W. They also confirm that the shape of the high-momentum part of the Doppler broadening spectrum is element-specific.

In chapter 6 three types of semiconducting materials were investigated: doped silicon, silicon irradiated with oxygen and GaN.

- Silicon is by far the most frequently applied semiconductor in electronic devices and point defects play an important role in its electrical properties. To create defects silicon doped with As and Sb was irradiated with electrons. Doppler broadening measurements performed at low temperatures showed that negatively charged defects were created with concentrations of $\sim$ 3 ppm in Si:Sb and $\sim$ 10 ppm in Si:As. The higher concentration in the As-doped Si is not surprising since this material had a ten times higher doping concentration than the Sb-doped Si. The doping atom near the annihilation site has a small effect on the annihilation characteristics which was observed in the two-dimensional angular correlation distributions.

- The use of a thin silicon layer on top of an insulator has advantages in the production of semiconductor devices. A way to create this is the implantation of silicon with oxygen (SIMOX). After annealing at 1350°C a top layer of silicon is created with the electrical qualities of bulk Si. The Doppler-broadening measurements showed that this layer still contains defects which can not be observed with TEM. Additional measurements with the low-background Doppler-broadening setup showed that this layer contains small defects (possibly in the form of SiO_2 precipitates) which have the same characteristics as multivacancy-multioxygen defects. Although these defects are electrically inactive they can become a problem when the size of device structures shrink.

- GaN is a semiconductor with a wide bandgap. It has therefore attracted interest as a candidate material for the production of blue LED's. The cause of the intrinsic autodoping of GaN to n-type has puzzled the field. This intrinsic autodoping has long been associated with N-vacancy defects. However, recent calculations for the n-type material seem to rule out the N-vacancy and predict a much lower formation energy for the Ga-vacancy.

Atomic superposition calculations have been performed for GaN with one N atom missing and with one Ga atom missing. The results for the N-vacancy are almost identical to defect-free GaN while the Ga-vacancy shows a clear effect in both the lifetime and the high-momentum part of the Doppler broadening curve. The low-background Doppler-broadening curves for semi-insulating GaN (defect-free) and n-type GaN are different and it is therefore concluded that n-type GaN contains Ga-vacancies.

In chapter 7 the formation of positronium in calcium sulphate is discussed. Soluble anhydrite contains open volumes in which positronium can be formed. The same open volumes can be occupied by water, thus prohibiting the formation of positronium. By heating gypsum soluble anhydrite is formed. Under atmospheric conditions the open volumes are filled with water while in vacuum the material dehydrates. The dehydration in vacuum was followed in time and a clear relation was observed between the water content and the positronium fraction in the angular correlation distribution. Chapter 8 concludes this thesis with some general remarks and prospects for the future.

Nomenclature

Symbol	Description
c	velocity of light
c_t	concentration of defects
$c(p_x, p_y)$	momentum sampling function
D_+	positron diffusion coefficient
E	measured photon energy
E_b	binding energy of the electron and the positron in the solid
E_d	difference between the two measured energies in a two detector DBAR experiment
E_s	sum of the two measured energies in a two detector DBAR experiment
e	elementary charge
$\mathbf{G}_i$	reciprocal lattice vector
G_j	orbital motion part of two-particle wavefunction with the electron in state j
$\hbar$	Planck's constant / 2 π
j_l	l^{th} spherical Bessel function
$\mathbf{k}$	wavevector
k_b	Boltzmann constant
k_x	wavevector in direction x
k_y	wavevector in direction y
k_z	wavevector in direction z
L	sample-detector distance
l_d	detector diameter
L_+	positron diffusion length
m^*	effective mass
m_o	rest mass of the electron
N_+	number of positrons emitted by the source
N_c	count rate in a in coincident measurement

N_{single}	single detector count rate
n_-	electron density
$n_m(p_x, p_y)$	measured ACAR distribution
$n_t(p_x, p_y)$	true ACAR distribution
$\mathbf{p}$	momentum
p_F	radius of the Fermi sphere
p_x	momentum in x direction
p_y	momentum in y direction
p_z	momentum in z direction
q_{TF}	Thomas Fermi screening length
R	backscatter coefficient for positrons
$R^-_{l,nl}$	radial part of electron (quantum numbers n and l) wavefunction
R^+	radial part of positron wavefunction
$\mathbf{r}$	position
r_0	classical electron radius
T	Absolute temperature
t	temperature in degrees Celsius
t_+	positrons transmission coefficient
t_γ	gamma ray transmission coefficient
u_j	correlated motion of two-particle wavefunction with the electron in state j
α	adjustable parameter in the GGA enhancement
Γ_c	FWHM of resolution contribution of c
γ_j	enhancement for electron state j
ΔE	Doppler broadening
ε	detector efficiency
ε	parameter in the GGA enhancement
Θ	angle
$\theta_{0.5}$	FWHM of the momentum distribution
κ_t	positron trapping rate
Λ_j	local annihilation rate for electron state j
λ	annihilation rate
λ_b	bulk annihilation rate
ν_t	specific positron trapping rate
$\rho^{2\gamma}$	momentum distribution as observed for two gamma annihilation
$\rho_j^{2\gamma}$	momentum distribution as observed for two gamma annihilation with an electron in state j

$\rho_{l,nl}^{2\gamma}$	momentum distribution as observed for two gamma annihilation for an electron with quantum numbers n and l
σ_1	resolution of detector 1
σ_2	resolution of detector 2
τ	positron lifetime
τ	width of the coincidence window
Φ	angle
χ	geometric detector efficiency
χ^2	chi squared
ψ_j^{ep}	positron-electron two-particle wavefunction for electron state j
ψ_+	positron wavefunction
ψ_j	wavefunction for electron state j
Ω	solid angle of the detector
∇n	gradient of the charge density

Abbreviation

1D-ACAR	one-dimensional Angular Correlation of Annihilation Radiation
2D-ACAR	two-dimensional Angular Correlation of Annihilation Radiation
ACAR	Angular Correlation of Annihilation Radiation
ADC	Analog to Digital Converter
BOX	Buried Oxide
CZ	Czochralski
DBAR	Doppler broadening of Annihilation Radiation
DIMES	Delft Institute for Microelectronics and Submicrontechnology
ECR	Electron Cyclotron Resonance
FWHM	Full Width at Half Maximum
FZ	float zone
GGA	Generalised Gradient Approximation
HDPE	High Density Polyethylene
HMC	Higher Momentum Component
HOR	Hoger Onderwijs Reactor
IRI	Interfaculty Reactor Institute
IPM	Independent Particle Model
KKR	Korringa-Kohn-Rostoker
LDA	Local Density Approximation
LED	Light Emitting Diode
LLD	Lower Level Discriminator
LMTO	linear-muffin-tin-orbital

MBE	Molecular Beam Epitaxy
o-PS	ortho-positronium
POSH	POSitrons at the Hor-reactor
p-PS	para-positronium
PS	Positronium
RT	Room Temperature
SOI	Silicon On Insulator
SI	Semi-Insulating
SIMOX	Separation by IMplantation of OXygen
TEM	Transmission Electron Microscope
TRIM	TRansport of Ions in Matter
UV	Ultra Violet
VEP	Variable Energy Positron beamline at Delft
VEPFIT	Variable Energy Positron FITting and modeling program

List of publications

Low-Energy Ion Scattering

H.H. Brongersma, R.H. Bergmans, L.G.C. Buijs, J-P. Jacobs, A.C. Kruseman, C.A. Severijns and R.G. van Welzenis, "Developments in Low-Energy Ion Scattering from surfaces", *Nuc. Ins. Meth.* B **68** (1992) 207.

R.G. van Welzenis, R.H. Bergmans, J.H. Meulman, A.C. Kruseman and H.H. Brongersma, "Low-Energy Ion Scattering at extremely low ion doses", NATO ASI, Porto Carras, Greece 1991 (Plenum, New-York 1992).

R.H. Bergmans, A.C. Kruseman, C.A. Severijns and H.H. Brongersma, "Simultaneous Energy and Angle Resolved Ion Scattering Spectrometer; First results", *Appl. Surf. Sci.* **70/71** (1993) 283.

Infrared cloud clutter

P.B.W. Schwering and A.C. Kruseman, "All-sky infrared cloud clutter analysis", SPIE Vol. **1967** Orlando 1993.

P.B.W. Schwering and A.C. Kruseman, "All-sky infrared cloud clutter", SPIE Vol. **2020** San Diego 1993.

Positron annihilation

A. van Veen, H. Schut, M. Clement, J.M.M. de Nijs, A. Kruseman and M.R. IJpma, "VEPFIT applied to depth profiling problems", *Appl. Surf. Sci.* **85** (1995) 216.

P. Asoka-Kumar, M. Alatalo, V.J. Ghosh, A.C. Kruseman, B. Nielsen and K.G. Lynn, "Increased Elemental Specificity of Positron Annihilation Spectra", *Phys. Rev. Lett.* **77** (1996) 2097.

A.C. Kruseman, H.Schut, A. van Veen, M. Clement and J.M.M. de Nijs, "Positron beam analysis of semiconductor materials using a two-detector Doppler broadening coincidence system", *Appl. Surf. Sci.* **116** (1997) 192.

V.J. Ghosh, M. Alatalo, P. Asoka-Kumar, K.G. Lynn and A.C. Kruseman, "The momentum distribution of annihilating positron-electron pairs in aluminum", *Appl. Surf. Sci.* **116** (1997) 278.

L.V. Jørgensen, A.C. Kruseman, H. Schut, A. van Veen, M. Fanciulli and T.D. Moustakas, "Investigation of vacancies in GaN by positron annihilation", MRS Fall Meeting 1996, *Mat. Res. Soc. Proc.* **449** (1997) 853.

A. van Veen, A.C. Kruseman, H. Schut, P.E. Mijnarends, B.J. Kooi and J.Th.M. de Hosson, "Positron Analysis of Defects in Metals", *Mater. Sci. Forum* **255-257** (1997) 76.

P.E. Mijnarends, A.C. Kruseman, A. van Veen, V.J. Ghosh, P. Ashoka-Kumar, A. Bansil, S. Kaprzyk and K.G. Lynn, "Two-Detector Doppler Broadening Profiles in Al", *Mater. Sci. Forum* **255-257** (1997) 784.

A.C. Kruseman, H. Schut, M. Fujinami and A. van Veen, "Decomposition of Doppler Broadened Annihilation Spectra", *Mater. Sci. Forum* **255-257** (1997) 790.

M. Alatalo, P. Asoka-Kumar, V.J. Ghosh, B. Nielsen, K.G. Lynn, A.C. Kruseman, A. van Veen, T. Korhonen and M.J. Puska, "Effect of lattice structure on the positron annihilation with inner shell electrons", *J. Phys. Cham. Solids* **59** (1998) 55.

P.E. Mijnarends, A.C. Kruseman, A. van Veen, H. Schut and A. Bansil, "Two-detector Doppler broadening study of enhancement in Al", *J. Phys.: Cond. Mat.* **10** (1998) 10383.

A.C. Kruseman, H. Schut, A. van Veen and M. Fujinami, "Oxygen implanted silicon investigated by positron annihilation spectroscopy", *Nuc. Ins. Meth.* B **148** (1999) 294.

V.J. Ghosh, B. Nielsen, A.C. Kruseman, P.E. Mijnarends, A. van Veen and K.G. Lynn, "The effect of the detector resolution on the Doppler Broadening measurements of both valence and core electron-positron annihilation", *Appl. Surf. Sci.* (to be published).

Samenvatting

Twee-dimensionale ACAR en lage achtergrond DBAR onderzoek aan materialen met defecten.

Om open-volume defecten in materialen te karakteriseren kan men gebruik maken van verschillende positronannihilatietechnieken. Twee van deze technieken werden al gebruikt op het Interfacultair Reactor Instituut van de Technische Universiteit Delft. In dit proefschrift worden de constructie en de eerste resultaten van twee, voor het IRI nieuwe, positronannihilatieapparaten beschreven. Het eerste apparaat bepaalt de hoekcorrelatie van de annihilatie straling in twee richtingen (2D-ACAR). Dit systeem meet een twee-dimensionale verdeling terwijl de meer gebruikelijke positron annihilatie technieken alleen maar een één-dimensionale verdeling geven. Het tweede systeem is een uitbreiding op een opstelling om de Dopplerverbreding van annihilatiestraling te meten. Hierbij wordt een tweede detector gebruikt om in coïncidentie met de eerste detector, metingen te verrichten. Ten gevolge van de coïncidentieconditie en de bekende relatie tussen de energieverschuivingen kunnen metingen worden verricht met achtergronden die drie ordes van grootte lager zijn, dan die van een opstelling met een enkele detector. Door deze achtergrondreductie is het mogelijk om het hoge impuls gedeelte van het Dopplerverbredingspectrum te onderzoeken.

Hoofdstuk 1 geeft een korte introductie van de verschillende positronenannihilatietechnieken. Theoretische berekeningen kunnen erg nuttig zijn voor de interpretatie van de metingen. Een methode om het hoge impuls gedeelte van de spectra te berekenen is de atomaire superpositie methode. De theoretische basis van deze methode wordt uitgelegd in hoofdstuk 2. Door het gebruik van een aantal benaderingen is het mogelijk om de computerrekentijd te reduceren. Deze benaderingen maken de methode echter minder geschikt voor de berekening van de bandelektronen en daarmee het centrale gedeelte van de impuls verdeling. De resultaten van de atomaire superpositie methode zijn vergeleken met de complexere berekeningen die gebruik maken van de Korringa-Kohn-Rostoker methode om de elektronische structuur te bepalen. De resultaten van de beide methodes zijn in goede overeenkomst met elkaar tussen 20 en $45 \times 10^{-3}\ m_0c$. Hiermee is aangetoond dat de atomaire superpositie methode een bruikbaar hulpmiddel is voor

de analyse van het hoge impuls gedeelte van Dopplerverbredingmetingen met twee detectoren.

Hoofdstuk 3 geeft een technische beschrijving van de twee nieuwe systemen. De gemeten twee-dimensionale hoekcorrelatieverdeling moet gecorrigeerd worden voor de meetcondities. De hiervoor noodzakelijke databewerking wordt beschreven in hoofdstuk 4. De resultaten voor zes metalen worden beschreven in hoofdstuk 5. Van deze zes metalen is aluminium meest uitvoerig onderzocht. Hierbij zijn onder meer metingen op temperatuur verricht. Uit de S-W plot blijkt dat boven 450°C , mono-vacatures gecreëerd worden. Tussen 450°C en 740°C vertoont de S-W plot een bijna lineaire relatie tussen S en W. Dit duidt op annihilaties in de omgeving van één type defect. In dit geval mono-vacatures. Bij 740°C wordt de lineaire relatie verstoord, wat waarschijnlijk wordt veroorzaakt door de creatie van di-vacatures. De atomaire superpositie methode is gebruikt om het hoge impuls gedeelte van het Dopplerverbredingspectrum te berekenen voor kamertemperatuur en voor 670°C . De aldus berekende verdelingen komen goed overeen met de experimentele resultaten. Als tweede materiaal is koper onderzocht. De overeenkomst tussen de berekende en de experimentele verdelingen was minder goed dan voor aluminium. De afwijkingen bij koper worden toegeschreven aan beperkingen in de gebruikte benaderingen voor het veel deeltjes gedrag. Hoewel de kwantitatieve overeenkomst tussen de berekeningen en de experimenten nog niet altijd bevredigend is, is de kwalitatieve overeenkomst wel goed. Dit blijkt uit metingen aan berylium, nikkel, molybedeen en wolfraam. Deze metingen bevestigen tevens dat de vorm van het hoge impuls gebied elementspecifiek is.

In hoofdstuk 6 zijn de volgende halfgeleider materialen onderzocht: gedoteerd silicium, silicium geïmplanteerd met zuurstof en GaN.

- Silicium is de meest gebruikte halfgeleider voor elektronische circuits. Punt-defecten spelen een grote rol voor de elektrische eigenschappen van silicium. Om defecten te creëren is met As en Sb gedoteerd silicium bestraald met elektronen. Dopplerverbredingsmetingen bij lage temperaturen tonen aan dat negatief geladen defecten gecreëerd zijn met concentraties van $\sim$ 3 ppm voor Si:Sb en $\sim$ 10 ppm in Si:As. De hogere concentratie in het As gedoteerde Si is gerelateerd aan de tien keer hogere doteringsconcentratie dan voor Sb gedoteerd Si. De aanwezigheid van een doteringsatoom in de directe omgeving van de annihilatielocatie heeft een klein effect op de annihilatiekarakteristieken. Dit effect wordt waargenomen in de twee-dimensionale ACAR verdelingen.

- Het gebruik van een dunne laag silicium boven op een isolator heeft grote voordelen bij het produceren van halfgeleider IC's. Dit soort materialen kan gemaakt worden door silicium te implanteren met zuurstof (SIMOX). Na uitstoken op 1350°C ontstaat een oxide laag met daarboven op een dunne laag van silicium. De dunne laag silicium heeft elektrische eigenschappen die vergelijkbaar zijn met bulk silicium. De Dopplerverbredingmetingen tonen echter aan dat deze laag nog steeds kleine defecten bevat (moge-

lijk in de vorm van SiO_2 precipitaten) met dezelfde karakteristieken als multivacature-multizuurstof defecten. Hoewel deze defecten kennelijk elektrisch inactief zijn kunnen ze een probleem gaan vormen wanneer de afmetingen van de structuren op een IC kleiner worden.

- GaN is een halfgeleider met een brede bandkloof. Daarom wordt het gezien als een kandidaat om blauwe LED's mee te maken. Een nog onbeantwoord vraagstuk voor GaN was de oorzaak van de intrinsieke autodotering naar n-type materiaal. Deze intrinsieke autodotering is lang geassocieerd met vacatures op het stikstofrooster. Recente berekeningen voor n-type GaN voorspellen echter een veel lagere formatieenergie voor een Ga-vacature dan voor een N-vacature waardoor de aanwezigheid van de laatste erg onwaarschijnlijk wordt. Atomaire superpositie berekeningen zijn verricht voor GaN, GaN met een N-vacature en GaN met een Ga-vacature. De resultaten voor een N-vacature zijn praktisch identiek aan die van defectvrij GaN terwijl de berekening voor de Ga-vacature een duidelijke effect geeft, zowel in de levensduur als in het hoge impuls gedeelte van het Dopplerverbredingspectrum. De Dopplerverbredingspectra met een gereduceerde achtergrond van semi-isolerend GaN (defect-vrij) en n-type GaN zijn verschillend. Hieruit wordt geconcludeerd worden dat n-type GaN, vacatures op het Ga rooster bevat.

Hoofdstuk 7 beschrijft positroniumformatie in calciumsulfaat. Oplosbaar anhydrite bevat open-volumes waarin de formatie van positronium mogelijk is. Dezelfde open-volumes kunnen ook bezet worden door watermoleculen waardoor de formatie van positronium belet wordt. Door gips ($CaSO_4 \cdot 2\ H_2O$) te verhitten wordt oplosbaar anhydrite (γ -$CaSO_4$) gevormd. In lucht zullen de open-volumes gevuld worden met water terwijl in vacuüm dit water weer verwijderd wordt. De dehydratie in vacuüm is in de tijd gevolgd. Hieruit bleek dat er een duidelijke relatie bestaat tussen de hoeveelheid water in het calciumsulfaat en de fractie positronium in de hoekverdelingsmetingen. Hoofdstuk 8 besluit dit proefschrift met een aantal algemene opmerkingen en mogelijkheden voor de toekomst.

A.C. Kruseman

Dankwoord

Het verrichten van promotieonderzoek en het schrijven van een proefschrift is niet mogelijk zonder de hulp van anderen. Daarom aan het eind van mijn proefschrift een dankwoord aan iedereen die mij de afgelopen jaren heeft geholpen.

In de eerste plaats wil ik mijn promotoren Tom van Veen en Hugo van Dam bedanken die het mogelijk maakten mijn promotieonderzoek te verrichten. Mede richting bepalend voor het onderzoek waren de nuttige suggesties die Tom van Veen maakte tijdens de vele discussies. Verder gaat mijn speciale dank uit naar Peter Mijnarends voor zijn jarenlange begeleiding. Tijdens deze periode heeft hij geprobeerd zijn kennis van ACAR aan mij over te brengen. Ook moet ik hem bedanken voor het zorgvuldig en kritisch lezen van mijn proefschrift. De leesbaarheid hiervan is aanzienlijk verbeterd dankzij zijn opmerkingen. Henk Schut wil ik bedanken voor alle hulp tijdens de Dopplerverbredingsmetingen waarbij hij mij de fijne kneepjes van het DBAR meten heeft bijgebracht. In de eerste jaren van mijn AIO-schap deelde ik samen met twee (en later drie) anderen de bunker. Op deze plek, tussen de fazanten, katten en bramen, heb ik samen met Karl Roos en mijn mede AIO's Maarten Clement en Lars Jørgensen een plezierige tijd doorgemaakt. Karl Roos moet ik tevens bedanken voor al zijn hulp bij de constructie van de ACAR opstelling en al het tekenwerk dat hij hiervoor verricht heeft. Zonder zijn hulp zouden wij nooit zo snel een werkende opstelling hebben gekregen. Op deze plaats wil ik ook Jan de Roode bedanken voor zijn hulp met de elektronica van het ACAR-systeem en Rene de Goede voor zijn hulp tijdens het plaatsen van de bron.

Behalve onderzoek in Nederland is er ook nog onderzoek in Amerika verricht. Na een boel problemen om de juiste reispapieren te verkrijgen stond ik hartje winter, in een meter sneeuw bij Brookhaven National Laboratory. Hier heb ik gedurende drie maanden met veel plezier onderzoek verricht. Deze tijd was nooit zo productief geweest zonder de volgende personen: Vinita Ghoosh voor de opvang gedurende de eerste dagen en de plezierige samenwerking, Kelvin Lynn voor zijn altijd kritische vragen, Matti Alatalo voor de hulp bij het ontrafelen van de computerprogrammatuur en de "site-seeing" activiteiten, Mihail Petkov als collega ACARer en natuurlijk Bent Nielsen en Ashoka-Kumar voor de positron annihilatie metingen. Gedurende mijn afwezigheid heeft Bob Heijenga als een goede huisbaas voor mijn woning in Delft gezorgd

waarvoor ik hem opnieuw wil bedanken.

Ondertussen werd de bunker langzaam ontvolkt. Nadat eerst Karl verhuisd was kwam ook voor mij het moment om naar het "hoofdgebouw" te verhuizen. In het hoofdgebouw kwam ik bij Peter Mijnarends en Kees Westerduin op de kamer. Kees wil ik bedanken voor zijn hulp bij de preparatie van verschillende preparaten en de talloze discussies die wij hebben gehad over een keur van onderwerpen. Voor de preparatie van de preparaten was ook de hulp van Danny Seegers van de universiteit van Gent onmisbaar en bij deze wil ik hem nogmaals bedanken voor het met elektronen bestralen van verschillende preparaten.

Verder moet ik natuurlijk mijn mede AIO's bedanken: Olof Dankert die altijd bereid is iets te organiseren en die tot 's avonds laat aanwezig is, Alexander Federov die vanwege een goed Russisch gebruik Sacha heet en voor wie ik hoop dat zijn MODEX programma ook in staat is zijn proefschrift te schrijven, Antonio Riviera die nadat hij een stage bij ons had verricht het zo leuk in Nederland vond dat hij ook hier zijn promotieonderzoek is gaan doen en verder de nieuwste AIO's Elena Abadjieva en Claudiu Falub die ik veel succes bij hun onderzoek wens.

Voor de hulp bij allerlei administratieve zaken ben ik het RF-secretariaat in de vorm van Riny Purmer en Sonja Jobse dankbaar.

Als laatste rest mij om mijn familie en vrienden te bedanken voor de steun die zij mij de afgelopen jaren hebben gegeven.

Bram

Curriculum Vitae

De auteur van dit proefschrift werd geboren op 11 maart 1968 te Amsterdam. In 1986 behaalde hij aan de Rijksscholengemeenschap te Amersfoort het VWO diploma. In datzelfde jaar is hij begonnen met zijn studie Technische Natuurkunde aan de Technische Universiteit Eindhoven. Het afstudeeronderzoek werd verricht in groep fysica van oppervlakken en grenslagen en succesvol afgesloten in 1992. Tussen 1992 en 1993 vervulde hij zijn militaire dienstplicht op het Fysisch en Elektronisch Laboratorium van TNO te Den Haag in de groep fysica en akoestiek. Na zijn afzwaaien als luitenant heeft hij hier nog zes maanden gewerkt om het onderzoek af te ronden. In 1994 is hij begonnen met zijn promotieonderzoek bij de afdeling Reactorfysica van aan de Technische Universiteit Delft. Hier is bij de afdeling Reactorfysica van het Interfacultair Reactor Instituut materiaalonderzoek verricht met behulp van positron annihilatie technieken. Tijdens zijn promotieonderzoek heeft hij gedurende drie maanden gewerkt op het "Brookhaven National Laboratory" in de Verenigde Staten van Amerika. Sinds 1998 werkt de auteur bij het Natuurkundig Laboratorium van Philips te Eindhoven.